HDL-TR-2087
September 1986

Prompt Charge Collection in Gallium Arsenide Diodes Struck by Energetic Heavy Ions

by Raine M. Gilbert
Gregory K. Ovrebo
Joe Schifano

U.S. Army Laboratory Command
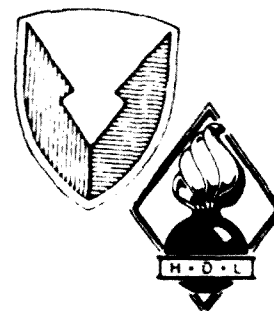**Harry Diamond Laboratories**
Adelphi, MD 20783-1197

REPORT DOCUMENTATION PAGE

1a. REPORT SECURITY CLASSIFICATION UNCLASSIFIED		1b. RESTRICTIVE MARKINGS AD-A173 515			
2a. SECURITY CLASSIFICATION AUTHORITY		3. DISTRIBUTION / AVAILABILITY OF REPORT Approved for public release; distribution unlimited.			
2b. DECLASSIFICATION / DOWNGRADING SCHEDULE					
4. PERFORMING ORGANIZATION REPORT NUMBER(S) HDL-TR-2087		5. MONITORING ORGANIZATION REPORT NUMBER(S)			
6a. NAME OF PERFORMING ORGANIZATION Harry Diamond Laboratories	6b. OFFICE SYMBOL *(If applicable)* SLCHD-NW-RH	7a. NAME OF MONITORING ORGANIZATION			
6c. ADDRESS *(City, State, and ZIP Code)* 2800 Powder Mill Road Adelphi, MD 20783-1197		7b. ADDRESS *(City, State, and ZIP Code)*			
8a. NAME OF FUNDING / SPONSORING ORGANIZATION Strategic Defense Command	8b. OFFICE SYMBOL *(If applicable)* DASD-H	9. PROCUREMENT INSTRUMENT IDENTIFICATION NUMBER			
8c. ADDRESS *(City, State, and ZIP Code)* Attn: R. C. Webb Huntsville, AL 35800		10. SOURCE OF FUNDING NUMBERS			
		PROGRAM ELEMENT NO. 6.32.22	PROJECT NO.	TASK NO.	WORK UNIT ACCESSION NO.

11. TITLE *(Include Security Classification)*

Prompt Charge Collection in Gallium Arsenide Diodes Struck by Energetic Heavy Ions

12. PERSONAL AUTHOR(S) Raine M. Gilbert, Gregory K. Ovrebo, and Joe Schifano

13a. TYPE OF REPORT Final	13b. TIME COVERED FROM 5/83 TO 12/85	14. DATE OF REPORT *(Year, Month, Day)* September 1986	15. PAGE COUNT 109

16. SUPPLEMENTARY NOTATION
HDL Project: 280628
AMS Code: 5-623222.K06D000

17.	COSATI CODES		18. SUBJECT TERMS *(Continue on reverse if necessary and identify by block number)*
FIELD	GROUP	SUB-GROUP	Single-event upset; SEU; gallium arsenide; funnel effect; plasma screening
20	12		
09	01		

19. ABSTRACT *(Continue on reverse if necessary and identify by block number)*

Charge collection was measured as a function of reverse-bias voltage on GaAs Schottky-barrier diodes bombarded with heavy, energetic ions. Ion species included in the study were copper (57 MeV), chlorine (62 MeV), oxygen (18 MeV), and, to establish a baseline for comparisons, ^{241}Am decay alpha particles (5.4 MeV). Measurements of the drift component of collected charge are compared to funneling predictions based on the Hu and McLean-Oldham models. Results show that significant funneling occurs in these gallium arsenide diodes, in reasonable agreement with predictions for the lighter ions, but to a lesser extent than predicted by both models for the heavier ions. By comparing these results with data on silicon diodes published in the literature, we show that gallium arsenide is less responsive to heavy-ion strikes than silicon. This enhances the value of the gallium arsenide technology for systems required to operate in environments containing high-energy heavy ions, such as cosmic rays in the exoatmosphere.

20. DISTRIBUTION / AVAILABILITY OF ABSTRACT ☒ UNCLASSIFIED/UNLIMITED ☐ SAME AS RPT. ☐ DTIC USERS	21. ABSTRACT SECURITY CLASSIFICATION UNCLASSIFIED	
22a. NAME OF RESPONSIBLE INDIVIDUAL Raine M. Gilbert	22b. TELEPHONE *(Include Area Code)* (202)394-3180	22c. OFFICE SYMBOL SLCHD-NW-RH

DD FORM 1473, 84 MAR   83 APR edition may be used until exhausted.   SECURITY CLASSIFICATION OF THIS PAGE

All other editions are obsolete.

UNCLASSIFIED

CONTENTS

APPENDICES

3

APPENDICES (Cont'd)

FIGURES

FIGURES (Cont'd)

FIGURES (Cont'd)

TABLES

DTIC
ELECTE
S   D
NOV 4 1986

B

Accession For

NTIS
DTIC
Un
Ju

By
Dis
A

Dist

A-1

7

1. INTRODUCTION

After a brief historical background on the discovery of semiconductor device upset by single ion impact, we describe analytical models that have been offered in the literature to quantify the phenomenon. This section concludes with a statement of the objective of this research and a discussion of its relevance to the device-physics community.

1.1 Background

The first published recognition of the threat of upset in electronics from energetic ions came from Binder, Smith, and Holman in 1975 [1]. They reported that anomalous upsets in the operation of orbiting communications satellites were attributable to the triggering of digital circuits by cosmic ray particles. They further showed that the upset rate correlated well with the flux of iron cosmic rays measured at orbit altitudes. May and Woods in 1979 reported that α-particles released during radioactive decay of impurities in packaging materials also produce soft errors in some semiconductor devices [2]. Following this observation, Hsieh, Murley, and O'Brien studied the mechanisms of charge collection in silicon junctions struck by α-particles [3-5]. Their approach was to generate self-consistent spatial and temporal records of the electric field and charge carrier motion using a computerized, finite-difference, simultaneous solution of Poisson's equation and the electron and hole continuity equations. To derive the initial conditions, they superimposed the electron and hole distributions of the α track onto the pre-strike charge and field distributions of a representative silicon n^+p junction. They were particularly interested in the relative importance of ambipolar diffusion and electric-field drift transport in the charge-collection process. Their modeling effort predicted that more charge should be collected by electric-field drift than was generated by the ion in the depletion layer of the device. This result was unexpected because the electric field was thought to be confined to the depletion layer even through the ion strike. Their solution showed that the initial movement of the ionization charge into the high-field region near the junction produced a strong distortion of the electric field, causing the field to extend farther down the track into the formerly neutral region (see fig. 1). Although it is not shown in the figure, the ion track in figure 1(a) is believed to extend approximately to the 5-V contour. The closer spacing of contours beyond this marks the high field region at the tip of the track. This field distortion--they called it field funneling--significantly increased the amount of track charge exposed to the collection field. Since drift transport is a very fast process compared to field-free carrier diffusion (which until that time was widely viewed as the dominant transport mechanism [6]), they concluded that the single-event upset (SEU) threat from α-particles was much greater than was commonly believed, especially for current-sensitive devices.

To verify the results of their computer calculations, Hsieh and his coworkers made a variety of high-speed charge-collection measurements on silicon devices bombarded by α-particles. Their measurements indeed showed that significantly more track charge is collected in the first nanosecond (i.e., by drift transport) than is generated in the depletion layer, a verification of

8 / 9

Figure 1. Equipotential contours in an n^+p silicon diode (substrate re-
sistivity = 14 ohm-cm) reverse-biased to +7.5 V at times t after a
4.3-MeV α-particle strike: (a) t = 0.1 ns, and (b) t = 1 ns (from
Hsieh et al [3]).

their funneling prediction. For many bias and doping conditions, additional
charge was collected during the ensuing nanoseconds, and was readily identi-
fied as the diffusion contribution. In the course of hundreds of measurements
at various junction biases and on devices having different resistivities, they
further demonstrated that drift collection was more dominant at higher biases
and in devices having higher resistivities, i.e., lower doping concentrations.
The latter effect they attributed to the persistence of funneling action until
the track ionization density near the junction approached the substrate doping
density, a process that takes longer for the lower doping densities. Hsieh et
al also concluded that the soft error rate (SER) would not be scaled down with
the device dimensions as would be expected if diffusion were the principal
collection mechanism. They pointed out that the amount of drift charge
collected in a given strike is essentially independent of collection area,
since carriers are funneled back along the track to the struck node. Their
strongest recommendation for reducing the SER was for circuit designers to
select more highly doped substrates for their devices.

1.2 Review of Funnel Models

After Hsieh, Murley, and O'Brien reported their findings, several re-
searchers independently sought a means of quantifying the funnel effect in
terms of simple analytical treatments, treatments not dependent on the costly
and time-consuming computer modeling techniques used by Hsieh et al. These
were C. Hu, G. C. Messenger, and the team of F. B. McLean and T. R. Oldham.

10

Hu has given what appears to be the simplest formulation for the funnel length L [7]. For a track density much greater than the doping density, Hu assumed that the original depletion layer field drives the majority carriers down the track into the neutral region. In the p-type semiconductor of his example, these carriers were holes.

He calculated the Ohm's law field produced by this hole current and then assumed that the minority carriers in the track are pulled from the neutral region into the depletion layer by this same field. He gave this field as

$$E = \frac{J}{\sigma} = \frac{I_p/A}{nq\mu_p} = \frac{I_p}{n'q\mu_p} \quad , \tag{1}$$

where J is current density, σ is the ion-track conductivity, I_p is the hole current, A is the track's cross-sectional area, n is the hole density in the track, n' is the hole line density (hole density per unit length of track), q is the electronic charge, and μ_p is the hole mobility.

Hu let this field drive track electrons in the neutral substrate to the neutral/depletion-layer interface (the "edge" of the depletion layer) with a velocity

$$v(r,t) = -\frac{dr}{dt} = \mu_n E(r,t) = \frac{\mu_n I_p(t)}{n'q\mu_p} \quad , \tag{2}$$

where μ_n is the electron mobility. With distance r measured from the edge of the depletion layer, r = R was defined as that furthest position down the track from which a minority carrier could be brought by drift to the edge of the depletion layer:

$$r(t) = R - \frac{\mu_n}{n'q\mu_p} \int_0^\tau I_p \, dt \quad , \tag{3}$$

where τ is the duration of drift collection. Hu stated that when electrons starting at r = R reached the edge of the depletion layer, i.e., when their $r(t) \to 0$, the integral in (3) had to equal the original number of holes in the depletion region, n'qW/cos Θ, where W is the depletion depth at the end of the drift collection process, and Θ is the angle of the track relative to the junction normal. Then

$$R = W\mu_n/(\mu_p \cos \Theta) \quad . \tag{4}$$

The total drift collection length L was therefore

$$L = \frac{W}{\cos \Theta} + R = \left(1 + \frac{\mu_n}{\mu_p}\right) \frac{W}{\cos \Theta} \quad . \tag{5}$$

11

In n-type semiconductors, the subscripts would be reversed. Note that this expression calls for greater funneling in p-type materials than in n-type because $\mu_n > \mu_p$. Hu derived a different expression for the case where the doping density is higher than the track density, and assumed in this case that holes are driven isotropically into the neutral half-space. He found that this result gave essentially the same result as that given by equation (5), and concluded that his treatments were not sensitive to the choice of current flow patterns. Hu also derived an expression for the time-dependence of the collection current, and, with judicious choice of values for electron and hole mobilities, drew favorable comparisons between his model and certain experimental data of Hsieh et al. He concluded finally that his model required all charge in the track to be set in motion by the Ohm's law field. As a result, many of the charge carriers not quite reaching the depletion layer edge at the end of the drift collection interval would diffuse the rest of the way in a short time interval, and further exacerbate the SEU problem.

In a later treatment based on the same notion of majority carrier flow into the neutral region, G. C. Messenger called for a funnel to be established by the hemispherically isotropic diffusion of majority carriers into the neutral substrate, following the substrate's spreading resistance [8]. The value given to this resistance was

$$R_s(t) = \rho/4L_p = \rho/4\sqrt{D_p t} \quad , \tag{6}$$

where L_p is the majority carrier diffusion length, ρ is the resistivity of the substrate, D_p is the majority carrier diffusion constant, and t is the time after the ion strike.

For purposes of evaluating funnel length, Messenger chose to evaluate R_s at that time when the radially averaged ionization density of the track was reduced by diffusion to the substrate doping level N_D:

$$\tau = \frac{n'}{4\pi D_p N_D} \quad , \tag{7}$$

where n' is the ionization line density. The current in the spreading resistance R_s was set equal to the ambipolar longitudinal current in the depletion layer segment of the track,

$$I \sim 2q\bar{\mu}n'E_o \quad , \tag{8}$$

where q is the electronic charge, $\bar{\mu}$ is an algebraic mean of electron and hole mobilities adjusted for high-field nonlinearities, and E_o is the initial depletion layer field.

The applied voltage V_o was thus divided between the depletion layer segment of the track and the diffusion distance into the neutral region,

$$V_o = V_j + IR_s \quad , \tag{9}$$

12

where V_j is now the reduced drop across the depletion layer. Messenger then defined his funneling enhancement factor as

$$F = \frac{V_o}{V_j} = \frac{V_o}{V_o - IR_s} \; . \tag{10}$$

With this funneling factor, Messenger's expression for the drift collection current was given by

$$I(t) = -2q\bar{\mu}n'E_o \; \sec \Theta \left(\frac{V_o}{V_o - IR_s}\right)\left[\exp\left(-\bar{\mu}\frac{dE}{dX}t\right) - \exp(-bt)\right] \; , \tag{11}$$

where Θ is the track angle relative to the junction normal, and the square bracket reflects the influence of two time constants, the first being the junction's collection time constant, and the second, the time required for the ion to establish the ion track (typically $\sim 10^{-11}$ s).

In a final step to facilitate the fitting of these results to experimental data, Messenger called for the insertion of two free parameters, α and β. The first was to be used as a multiplier of τ, the time required for diffusion to reduce the average track density to the value of the semiconductor doping density, as in equation (7); this τ was identified as the critical time constant for drift charge collection. The second was to be used as a multiplier of R_s, the spreading resistance. Messenger called for these two parameters to be assigned values that produce the best agreement between his model's predictions and measured data. No assessment of prospects for assigning universal values to these constants was given, nor were actual comparisons to data included in his paper.

A third model of funneling was reported by the team of McLean and Oldham [9]. Their treatment was a phenomenological model based on the concept of an effective funnel length. It described an essentially radial ambipolar diffusion of ionization charge within the track plasma column and a coincident drift collection of carriers only from the exterior sheath of the column. The sheath was defined as that part of the track where the ionization density has fallen approximately to the value of the doping density, and where a radial charge separation occurs. The funnel was said to extend down the ion track as the initial junction is neutralized during early drift collection. For simplicity, the longitudinal electric field E_L was assumed to be essentially linear over the effective funnel length L_c. This length was given as the average distance down the track that the field reaches, and from which drift currents are collected. Accordingly, charge collected by drift was given as

$$Q_c = q\bar{N}_o(L_c)L_c \; , \tag{12}$$

where q is the electronic charge and $\bar{N}_o(L_c)$ is the ionization line density averaged over L_c. Note that this use of a line density averaged over L_c insures that Q_c will never exceed the total ionization charge produced in the

13

track, even if the predicted funnel length L_c should exceed the actual length of the track. The collection length L_c was formally defined as the depletion layer depth x_d plus that portion of the track extending into the initially neutral region from which minority carriers are funneled during the collection time interval τ_c:

$$L_c = \bar{v}_d \tau_c + x_d \ .$$ (13)

Here, $\bar{v}_d$, the average drift velocity, was to be evaluated self-consistently with the expression

$$\bar{v}_d = \bar{\mu}_n(E_L)\bar{E}_L = \bar{\mu}_n(E_L) \frac{V_o}{L_c} \ ,$$ (14)

where V_o is the applied bias voltage and $\bar{\mu}_n(E_L)$ is the field-dependent mobility of minority carriers (electrons in this example) averaged over L_c. The charge collection time τ was derived using several additional assumptions. The radial field responsible for ionization charge separation was assumed to be excluded from the core of the plasma column. Its effect was therefore limited to pulling the holes out of the sheath. Once outside the plasma column, these majority carriers were assumed to be turned into the substrate by the field outside the track sheath. Near the surface of the device, the radial separation field was assumed to have a value comparable in magnitude to the initial depletion layer field at the surface, $E_d = V_o/x_d$. The escaping hole current density was then given as

$$J_p = N_A v_p \ ,$$ (15)

where v_p is evaluated for a field magnitude $|V_o/x_d|$, and N_A is the acceptor doping density for the p-type bulk silicon represented in the model. As the majority carriers are pulled out of the track into the surrounding space, they leave an equal number of uncompensated electrons behind. An assumption of plasma neutrality required that the collection rate for minority electrons at the surface node equal the escape rate for majority holes out of the sheath. Then, using (15),

$$\frac{dN}{dt} = -2\pi r(t)J_p = -2\pi L_D J_p = 4\pi N_A v_p (Dt)^{1/2} \ .$$ (16)

In this expression, N is the plasma line density, v_p is the hole escape velocity in the separation field, and the radius of the charge-separation sheath $r(t)$ has been set equal to the diffusion length $L_D = (4Dt)^{1/2}$, where D is the ambipolar diffusion constant and t is the time after the ion strike. The integration of this expression yields

$$N(t) = N_o \left[1 - \left(\frac{t}{\tau_c} \right)^{3/2} \right]$$ (17)

14

with

$$\tau_c \equiv \left(\frac{3N_o}{8\pi N_A v_p D^{1/2}} \right)^{2/3} \quad . \tag{18}$$

τ_c is the value of t for which $N(t) \to N_A \approx 0$, i.e., the time to complete drift collection. Note that the assumptions above call for funneling to continue at a rate governed by the product of the majority carrier current density at the sheath radius, $J_p = N_A v_p$, and the sheath surface area, which is continually expanding because of ambipolar diffusion. Thus, in effect, ambipolar diffusion is an important regulator of the drift collection rate in the McLean-Oldham model.

In their paper, the authors compared their effective funnel length predictions with experimental data that they obtained bombarding variously doped silicon n^+p and p^+n diodes with ^{241}Am α-particles. Their instrumentation was similar to that used by Hsieh and his coworkers. The agreements were quite good throughout the range of test parameters covered. In particular, their measurements showed the predicted dependence of prompt collected charge on doping level and bias. Moreover, they invariably observed larger collections in p-type silicon than in n-type silicon. This again is predicted by their model because L_c depends directly on the minority carrier mobility (eq (13) and (14)). In p-type silicon, the minority carrier is the electron, which is more mobile than the hole.

A year after they first introduced their effective funnel length model and experimentally verified its accuracy for α-particles, Oldham and McLean sought to apply their treatment to the case of silicon junctions struck by heavier ions (beryllium, oxygen, silicon, and copper) [10]. In this paper, they took the opportunity to introduce a slight modification to the model that provided a more realistic representation of the radial ionization distribution in the ion track. Instead of modeling a uniformly ionized track with sheath radius $r(t) = L_D$ as in reference 9, they derived a modified sheath radius:

$$r(t) = \beta L_D = 2\beta(Dt)^{1/2} \quad , \tag{19}$$

where

$$\beta = \langle \{ \ln(N_o/4\pi N_A Dt) \}^{1/2} \rangle \tag{20}$$

is the direct result of replacing the uniform track plasma density with a radial Gaussian distribution centered on the track axis and normalized to the diffusion length L_D. The brackets in equation (20) denote "an appropriate time average over the drift collection time." Because β has only a weak functional dependence on the argument of the logarithm, the authors elected to accomplish the averaging by setting $t = \tau_c/2$, where τ_c was calculated with $\beta = 1$ in equation (21).* The modified charge collection time was then

---

*F. B. McLean (Harry Diamond Laboratories), private communication.

15

$$\tau_c = \left[\frac{3N_o}{8\pi\beta N_A v_p D^{1/2}} \right]^{2/3} . \tag{21}$$

For $L_c \gg x_d$, the collected charge was approximately

$$Q_o \approx \left[\frac{3N_o}{8\pi\beta N_A v D^{1/2}} \right]^{2/3} . \tag{22}$$

For α-particle tracks, the effect of β was to reduce Q_c by 6 to 12 percent. This result slightly improved the already good agreements found in their treatment of α-particles. The effect of β for much heavier particles such as the copper ion was to reduce the Q_c prediction by as much as 30 percent. Even with this correction, the model still overpredicted prompt charge collection from tracks formed by ions heavier than beryllium. The relative differences were greatest in the midrange of bias (5 to 15 V), where the model predicted prompt collection of all charge in the track. These 100-percent collection predictions were usually two to three times larger than the corresponding measurements. The authors attributed this result to the model's representation of the longitudinal electric field as a field linearly decreasing from V_o/L_c at the surface to zero at the end of the effective funnel length. For lightly ionized α and beryllium tracks, they felt that this was a reasonable representation. They suggested that tracks formed by heavier ions may have such large ionization densities and high conductivities that screening effects on the initial junction field reduce the potential variation along the track to values much smaller than V_o/L_c, leaving most of the applied bias potential to fall across the nonionized region beyond the end of the track. In this case, the smaller longitudinal field along the track would collect the much smaller amounts of prompt charge seen in their heavy-ion experiments.

The research described above was all directed at SEU in silicon, the semiconductor material from which state-of-the-art electronic switching devices are almost exclusively made. Citing the increasing importance of GaAs in radiation hardening applications, Hopkins and Srour reported studies of SEU charge collection and funneling in GaAs devices [11]. The ions they used in their experiments were 5-MeV α-particles emitted from a ^{244}Cm thin-foil source. Their targets, n-type Schottky-barrier GaAs diodes, were formed from gold metallizations on doped epitaxial layers, with ohmic contacts on the semiconducting substrates. The epitaxial layers, 7 to 20 μm in thickness, were doped with sulfur (a donor) to densities in the range of 10^{14} to 10^{16} cm^{-3}, while the semiconducting substrates were all doped with tellurium at a density of $\sim 3 \times 10^{18}$ cm^{-3}. Instrumentation was essentially comparable to that used by Hsieh et al and McLean and Oldham.

In their report, Hopkins and Srour discussed the effect of recombination on the charge collection process in their diodes. They considered Auger (inverse impact-ionization), radiative (direct band-to-band), and Shockley-Read-Hall (trap-assisted) recombination processes. Using the limited and widely scattered data on cross sections and recombination rates seen in the literature, they assigned approximate regimes of predominance based on track

ionization densities as follows: Auger recombination above 10^{21} cm^{-3}, radiative recombination between 10^{17} and 10^{21} cm^{-3}, and Shockley-Read-Hall recombination below 10^{17} cm^{-3}. Assuming initial ionization densities in the core of the α track of $\sim 3 \times 10^{21}$ cm^{-3}, they estimated an associated Auger lifetime of tens of picoseconds. Estimating initial average noncore densities of $\sim 5 \times 10^{19}$ cm^{-3}, they gave a minimum radiative lifetime of ~ 0.4 ns, and noted that radiative recombination would dominate beyond this time until ionization densities approached 10^{17} cm^{-3}. By this time, the charge collection process is essentially complete. If track densities were reduced only by recombination, this last regime would be reached through radiative recombination over tens of nanoseconds. In reality, ambipolar diffusion and plasma erosion by bias fields add to the effects of recombination in reducing the ionization density. However, the authors stopped short of an attempt to treat these multiple concurrent mechanisms analytically. Instead, they noted that in those measurements where α tracks were entirely enclosed in the high-field depletion layer (where one expects 100-percent collection by drift), only 85 percent of the charge initially produced was collected. They attributed this shortfall to the effects of prompt recombination in the track core during the collection interval. They also noted that the collection percentage increased slightly with small increases in the bias. They saw this as an indication that recombination might be larger than 15 percent at lower biases, but concluded that avalanche ionization at these higher biases could also be responsible for the effect. As a result of these considerations, Hopkins and Srour included a 15-percent recombination term in the comparisons of their data with the Hu and McLean-Oldham models.

These comparisons were made only for a single data point in the measurements on a single sample doped to 1.4×10^{15} cm^{-3}. This data point corresponded to a 5.0-MeV α strike and a reverse-bias voltage of 20 V. Under these conditions, prompt charge was collected commensurate with an 8.0-μm collection length. The authors applied the McLean-Oldham model and predicted an effective funnel length of 8.0 μm, a perfect agreement. A corresponding solution of Hu's model, using an iterative solution of equation (5) with $E = 20^V/L_c$, gave a value of 7.4 μm, also a good agreement for that data point.

Hopkins and Srour concluded that funneling after an α strike is a "factor-of-two" enhancement effect in their GaAs devices, that the Hu and McLean-Oldham models treated it accurately, and that their GaAs data gave evidence of a modest (15-percent) recombination effect.

In summary, several independent research groups have demonstrated that (1) an α-particle penetrating a reverse-biased semiconductor junction causes a rapid drift collection of ionization charge at the junction node, (2) that the amount of charge so collected is typically greater than that produced by the α-particle within the initial electric field region of the device, and (3) that the excess prompt collection is adequately explained by a field funneling mechanism, for which at least two well-defined analytical models exist. It has also been experimentally demonstrated that heavy ions produce funnel effects in silicon, but the one model that has been compared to data in this case, the McLean-Oldham model, tends to overpredict prompt charge collection by a considerable margin.

17

There have been no investigations of heavy-ion charge collection in GaAs, either analytically or experimentally. In particular, the reduced funneling observed for heavy ions in silicon and the possibility of the same effect in GaAs have not been explored.

1.3 Objective and Relevance of Research

The primary objective of this research is the experimental characterization of prompt charge collection in GaAs junctions struck by high-energy heavy ions. Secondary objectives are the evaluation of the adequacy of the Hu and McLean-Oldham models in treating this phenomenon in GaAs, and, in the process, an accounting for the apparent influence of high track densities on the funneling action reported by Oldham and McLean. The reliance of the Messenger model on free parameters makes it unsuitable for predicting results in advance of measurements. For this reason, his treatment will not be considered further in this study.

The relevance of this research stems from the potential importance of the GaAs technology to the microelectronics industry, especially that part of the industry dedicated to satellite electronics. There, data processing requirements have traditionally pushed the state of the art, both in processing speed and storage capacity. Improvements in the silicon technology to meet these needs are now largely directed at the reduction of device dimensions to the submicron level. There are clear signs, however, that progress toward this goal is increasing the vulnerability of semiconductor junctions to upset and damage from nuclear and space radiations, especially the radiation components responsible for single-event effects. The increased SEU vulnerability derives primarily from the extremely small charge transfers required for switching submicron devices, as compared with the free charge introduced into a junction region by an ionizing particle [12]. The increased vulnerability of submicron devices to permanent damage derives in part from the fact that stable defect clusters produced by energetic ions may approach the dimensions of the device junction itself, permanently altering its conduction characteristic [13] and increasing dark current leakage [14]. Moreover, single ions have been shown to produce latchup and subsequent burnout in various complementary metal-oxide semiconductor microcircuits, an effect judged to be more likely in devices with junction dimensions <2 μm [15]. Thus, the concern exists in parts of the radiation effects community that submicron miniaturization of silicon devices to meet the speed and capacity requirements of the electronics industry may be self-defeating, at least in terms of resistance to SEU.

An alternative to further miniaturization is the development and use of GaAs microelectronic devices, which are inherently less sensitive to ionizing radiation [16] and are intrinsically faster than corresponding silicon devices. Electron mobility in GaAs is almost 6 times higher than in silicon [17], so that much faster data-processing rates can be attained in the n-type GaAs device than in silicon devices having the same dimensions. The maturity of the silicon technology and the comparative immaturity of the GaAs technology have delayed the widescale introduction of GaAs devices into satellite

18

electronics. Nevertheless, the current dominant role of doped GaAs in short-wave infrared optoelectronics and monolithic microwave integrated circuits, and the importance attached to the GaAs microelectronics technology by the U.S. Government (through the Defense Advanced Research Projects Agency*) suggest that at least a partial shift to GaAs will occur in the next decade. The undetermined vulnerability of GaAs devices to heavy-ion SEU is therefore a latent obstacle to the insertion of the GaAs technology into satellite design and manufacture.

Additional relevance for this research project follows from the failure of SEU models to accurately predict prompt charge collection when heavy ions strike semiconductor junctions (recall that the McLean-Oldham model strongly overpredicted results in silicon [10], and a similar tendency exhibited by the Hu model in comparisons with gallium arsenide data will be demonstrated later in this report). It follows that a use of these models to predict heavy-ion results in GaAs devices will be at least equally suspect, especially in view of the marked difference in silicon and gallium arsenide electron mobilities (electron mobility is a critical parameter in both models). Thus, an experimental approach is seen to be the most reliable and direct means of characterizing heavy-ion charge funneling in GaAs.

2. THEORY

In the first part of this section, the basic steps taken to convert ion-impact conditions and parameters to predictions of simple charge collection will be described. Then a brief description will be given of the formation of the diode depletion layer.

2.1 Ion Energy Considerations

The first critical parameter is the ion energy at the point of entry into the charged epitaxial layer. This value determines not only the amount of ionization charge produced in the diode, but the ionization distribution relative to the high-field and quasi-neutral regions. The heavy ion is produced by the tandem accelerator with a well-defined, highly resolved energy. Subsequently, it undergoes several sequential energy-loss interactions before reaching the device junction. First, the ion is scattered out of the main beam into a 20° side drift leading to the diode under test. The energy lost to the recoil of the scattering atom (gold in this case) is calculated using the Rutherford scattering theory. In this classical scattering theory, the kinetic energy and momentum are conserved. Eliminating target-atom recoil parameters in the simultaneous solution of the conservation equations gives

$$v^2 - \frac{2m \cos \theta}{m + M} v - \frac{M - m}{M + m} = 0 \quad , \tag{23}$$

---

*Sven Russo (DARPA), private communication.

where v is the scalar value of the incident ion's reduced recoil velocity (normalized to that ion's nonrelativistic incident velocity), m and M are the masses of the incident ion and target (scattering) atom, respectively, and Θ is the deflection angle of the scattered ion, required to be 20° in this experiment [18]. The positive root is the only physical solution to this quadratic equation; it is

$$v = \frac{m \cos \Theta}{M + m} \left\{ 1 + \left[1 + (M^2 - m^2)/(m \cos \Theta)^2 \right]^{1/2} \right\} \quad . \tag{24}$$

The energy E_s of the ion after scattering is then

$$E_s = v^2 E_o \quad , \tag{25}$$

where E_o is ion's initial energy.

The low-probability, high-angle scatter of the ion into the side drift can occur at any time during the ion's transit of the scattering foil. During this transit, the ion is losing energy through a continuous series of small-angle inelastic collisions with gold atoms. The ion's energy loss during these collisions is well represented by the continuous slowing down approximation (CSDA) for which energy loss rates have been provided graphically by Ziegler [19]. Figure 2 is a typical graph of the Ziegler energy loss rates (stopping powers) for various atomic particles in germanium. The loss rate data for germanium were used as approximations of the unreported loss rates for gallium arsenide (with adjustments for the differing densities) since the atomic numbers of gallium and arsenic bracket the atomic number of germanium. Similar data from Ziegler were used to treat slowing down and ionization in silicon. Loss rates for copper ions (atomic number 29) were not given in the Ziegler data. However, data given for nickel (atomic number 28) and zinc (atomic number 30) permit an accurate interpolation to arrive at loss rates for copper ions. The complete set of Ziegler graphs for germanium and silicon are contained in appendix A.

To insure that ion energy loss due to nuclear collisions is a small effect in the slowing of ions in target diodes, the nuclear stopping formulation reported by Ziegler was solved for the ions and energy range of interest [19]. Nuclear stopping is given as

$$S_n = s_n(8.462 \ Z_1 Z_2 M_1)/\left[(M_1 + M_2)(Z_1^{2/3} + Z_2^{2/3})^{1/2} \right] \quad , \tag{26}$$

where

$$s_n = 0.5 \ \ln(1 + \varepsilon)/\left(\varepsilon + 0.10718 \ \varepsilon^{0.37544} \right) \quad , \quad \text{and}$$

$$\varepsilon = 32.53 \ M_2 E/\left[Z_1 Z_2 (M_1 + M_2)(Z_1^{2/3} + Z_2^{1/2})^{1/2} \right] \quad .$$

Figure 2. CSDA energy loss rates for S → U ions with energies from 0.5 to 5 MeV/amu (from Ziegler [19, p 236]).

21

The nuclear stopping powers given by equation (26) for the four bombarding particles are plotted in figure 3. They may be compared to the much larger ionization stopping powers in figure 4 [19]. The net relative energy loss due to nuclear stopping of a 60-MeV Cu ion is shown in figure 5. As shown, the effect is only 2.5 percent for this worst case, and almost all the nuclear stopping occurs at the end of the particle's range. The effect is even more negligible for the three lighter ions. Nuclear stopping is therefore neglected in the charge collection calculations given later.
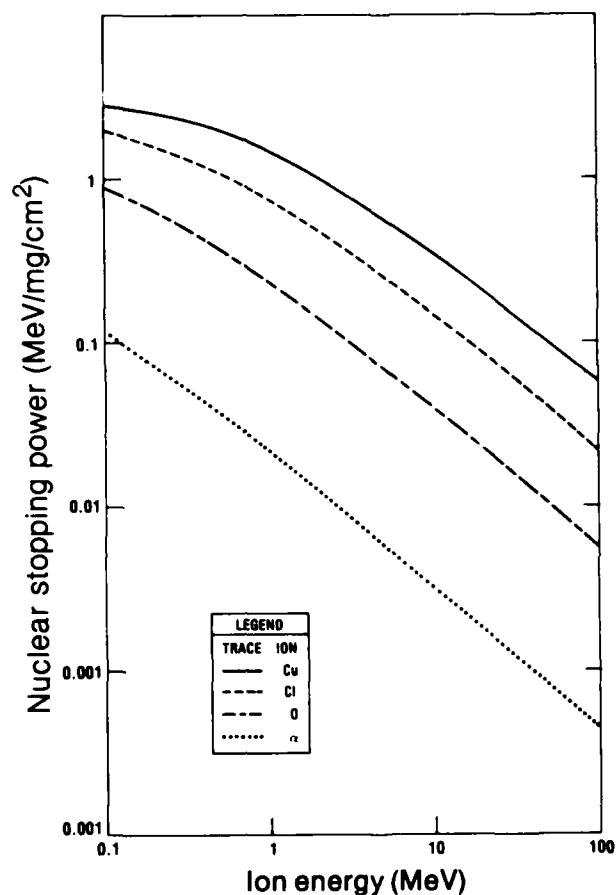

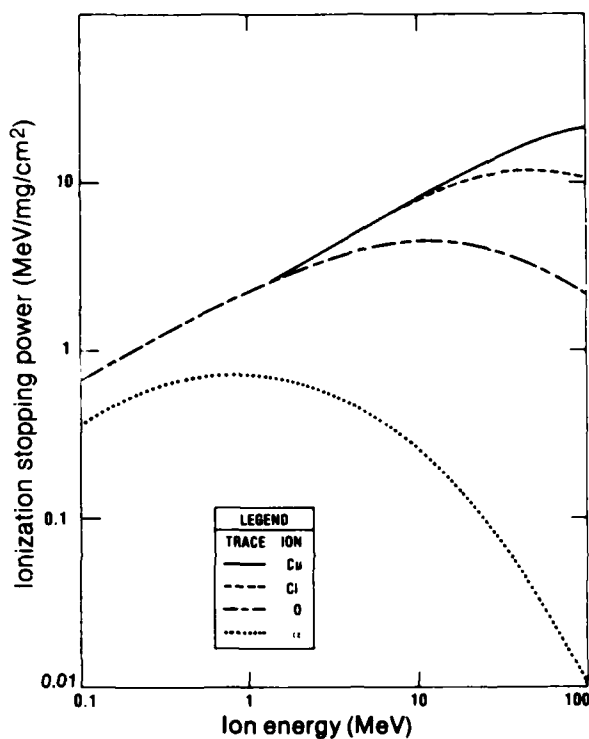Figure 3. Nuclear stopping powers for Cu, Cl, and O ions and α-particles in Ge.

Figure 4. Ionization stopping powers for Cu, Cl, and O ions and α-particles in Ge.

22

Figure 5. Relative nuclear stopping for copper ions in GaAs (Ge).

To determine a representative energy of the scattered beam, we consider two trajectory extremes. Figure 6 depicts these two extremes for the copper ion incident on the gold scattering foil. In one extreme, the ion is scattered into the side-drift direction upon first reaching the scattering foil. The scattered ion, with energy reduced according to equation (25), then undergoes continuous slowing down over the distance d/cos 20°. In the second extreme, the ion manages to traverse the entire thickness of the foil before undergoing the 20° scattering event at the rear surface. During this transit, its energy is reduced according to the CSDA applied over the distance d; its energy after the 20° scatter is further reduced according to equation (25). As figure 6 shows, these two extremes yield scattered energies differing by only a few percentage points; the representative energy in the scattered beam is therefore taken to be just the arithmetic average of the two energies shown.

23

Figure 6. Large-angle scattering of incident copper
ion from front and rear surfaces of scattering foil.

After the ion is scattered into the side drift, it still must trav-
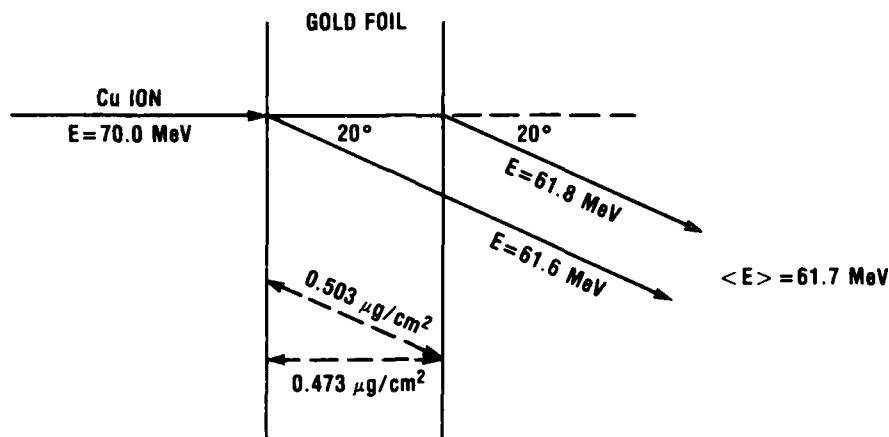erse the metallization layers of the diode before reaching the semiconductor
junction. The energy loss during this transit is again calculated using the
CSDA. Once the ion energy at the diode junction is known, the CSDA can then
be used to calculate the ion range and the ionization density along the ion's
track in the semiconductor. The ion range is found by incremental application
of the CSDA energy loss rate across short path increments to reduce the ion
energy to zero. The number of path increments required to accomplish this
stopping gives the ion range. The ionization line density is found by con-
verting CSDA energy loss per unit track length into an ion-pair line density
using the average energy required to produce a single ionization. This energy
is taken to be 4.80 eV/ion-pair in gallium arsenide, an average of those
values reported in the literature [20]. The corresponding value for silicon
is 3.65 eV/ion-pair [21].

2.2 Formation of Depletion Layer

In the large reverse-biased diodes used in this study, the steady-
state (prestrike) charge distribution is essentially that of a distributed
planar dipole layer. Figure 7(a) shows charge distributions in a cross-
sectional view of the diode junction. Figure 7(b) shows field and potential
as a function of depth. An n-type GaAs diode is shown charged to a nominal
reverse bias, $-V_o$. The donor-doped epitaxy is depleted out to a distance x_D
by the presence of negative charge on the metallization. The portion of the
ion trajectory lying in this high-field region determines how much of the
ionization produced by the ion is assured of drift collection, apart from
funneling enhancement. This makes the depletion depth x_D a critical parame-
ter. So that it can be expressed in terms of the observables of the problem,
Poisson's equation is doubly integrated in one dimension over x, the distance
from the junction, and the appropriate boundary conditions are applied:

24

$$\vec{\nabla} \cdot \vec{E} = \frac{\rho}{\varepsilon} = q \frac{N_D}{\varepsilon} \quad , \quad 0 \le x \le x_D \quad ,$$

$$= 0 \qquad , \quad x > x_D \quad , \qquad (27)$$

where $\vec{E}$ is the electric field, ε is the dielectric constant, given as a uniform scalar quantity equal to 13.0 [22], and ρ is the charge density. The charge density (initially just the density of charged donors) is equal to the uniform donor density N_D times the positive electronic charge q for $0 \le x \le x_D$ and is equal to zero for $x > x_D$. Integrating with respect to x' from x' = 0 to x' = x gives

$$E(x) = E(0) + \frac{\rho x}{\varepsilon} \quad . \qquad (28)$$

Applying the first boundary condition, $E(x_D) = 0$, yields

$$E(x) = \frac{\rho}{\varepsilon} \left(x - x_D \right) \quad . \qquad (29)$$
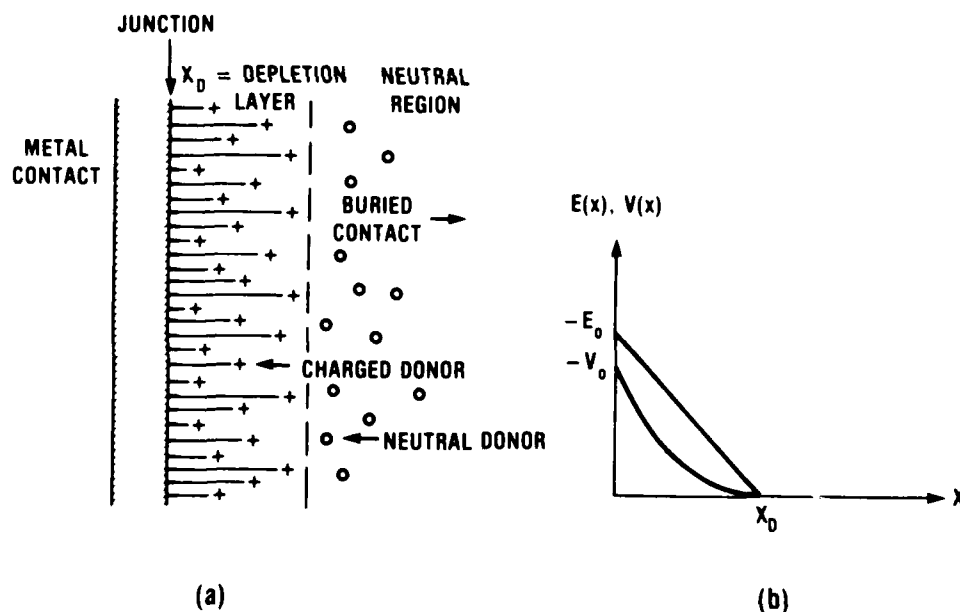

Figure 7. Reverse-biased junction before ion strike: (a) charge distribution, and (b) E and V as functions of depth.

This describes the field in figure 7(b) that, for this n-type diode, has a maximum negative value $-\rho x_D/\epsilon$ at the junction. The field magnitude falls linearly with x to a zero value at $x = x_D$. A second integration over the range $x < x_D$ to $x = x_D$, and the application of the second boundary condition, $V(x_D) = 0$, gives

$$V(x) = \frac{\rho}{\epsilon} \left[x_D x - \frac{1}{2} \left(x_D^2 + x^2 \right) \right] \quad , \tag{30}$$

which describes the parabolic potential variation shown in figure 7(b). The depletion depth x_D is expressed in terms of $V_o \equiv V(0)$, N_d, and ϵ by evaluating (30) at the junction, $x = 0$:

$$x_D = \left(\frac{2\epsilon |V_o'|}{q N_d} \right)^{1/2} \quad . \tag{31}$$

Implicit in the term for applied bias V_o is the constant additive contact potential, approximately equal to -1 V for the gallium arsenide diodes used in this experiment [23,24].

The product of x_D calculated with equation (31) and the ionization line density calculated using the CSDA then give the ionization charge one expects to be promptly collected from within the depletion layer for a given bias and doping level. The funneling enhancement over and above this "guaranteed prompt collection" is predicted by the Hu and McLean-Oldham funnel models described in the previous section.

3. EXPERIMENTAL APPROACH

This section describes the approach taken to achieve the primary research objective, the experimental characterization of prompt charge collection in GaAs diodes hit by heavy ions. The preparation of diode samples and the measurement of their voltage-capacitance characteristics are described first, followed by descriptions of the experimental configuration and the test procedure.

3.1 Sample Preparation and Characterization

Preparation of samples included first a fabrication of the Schottky-barrier diodes, and then a measurement of the diode leakage current and capacitance as functions of reverse bias voltage. Segments of n-type GaAs wafers were purchased from Northrop Research and Technology Center. They had semiconducting substrates doped with tellurium to a density of 1×10^{18} cm^{-3}. These segments were remnants of two of the same wafers Hopkins and Srour used in their SEU study [11]. One was epitaxially doped with sulfur to 8.0×10^{14} cm^{-3}, the other with sulfur to 1.3×10^{15} cm^{-3}. Final sample preparation was carried out at the Harry Diamond Laboratories Microelectronics Facility. There, each segment was cut into 12 to 15 squares, approximately 2×2 mm. Each square was then subjected to a two-layer metal vapor-phase deposition

process to produce a large 1-mm-diameter circular electrode on the epitaxial surface. The first layer was a 50-nm thickness of chromium to insure adhesion to the GaAs and the formation of a good metal/semiconductor interface, required for the Schottky barrier. The second layer was 80 nm of gold to facilitate wire bonding. The next steps were cementing the chip substrate to the header ground surface using conducting epoxy, and attachment of the wire to the diode. The wire was welded to the metallization by a combination of temperature ($\sim$400 K) and pressure ($\sim$$10^5$ psi). The other end of the wire was connected with conducting epoxy to a high-frequency (1-GHz) feedthrough contact in the base of the header. Removable header lids were provided to protect the diodes during handling and storage. Figure 8 shows features of a typical test diode.

(a)

(b)

80-nm Au
50-nm Cr

Epitaxy, 20 μm;
Sn at 8 × 10^{14} cm^{-3}
or $^.3 × 10^{15}$ cm^{-3}

Semiconducting
substrate, $\sim$0.5 mm;
Te at 10^{18} cm^{-3}

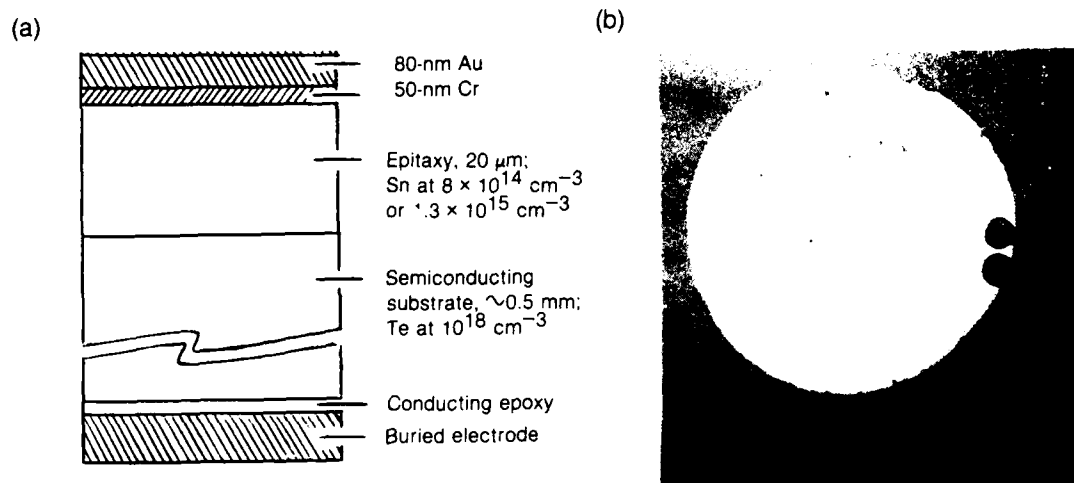Conducting epoxy
Buried electrode

Figure 8. GaAs diode test sample showing (a) cross section of junction region, and (b) a top view of diode metallization, with redundant wire bonds.

The circular metallizations on the diode surfaces were made large, 1.0 mm in diameter, to insure a large sample capacitance. In this way, the ~1-pF frequency dependence of the probe capacitance was made a negligible perturbation to the net capacitance charged by the ion strike. Access to the mounted diode for capacitance measurement required the fabrication and use of an adaptor plug having a front end resembling the TEK 6201 high-impedance probe tip (see fig. 9). Diode capacitance was measured as a function of reverse bias using a Boonton Electronics capacitance meter, model 72BD, and a Hewlett Packard multifrequency LCR meter, model 4275A. These meters probe device capacitance with a sinusoidal variable-voltage signal. The first meter uses a fixed 1-MHz probe frequency; the second provides optional probe frequencies that include 1 MHz. Figure 10 shows the configuration used for measuring the capacitance of the diode when it was mounted in its holder. Holder capacitance was found to be 8.6 ± 0.5 pF. Table 1 gives capacitance measured with the Boonton 72BD as a function of reverse-bias voltage for

representative low- and high-doped diodes. Results of capacitance measurements for the remaining test diodes are given in appendix B, including representative comparisons of capacitances measured with the two meters on a given diode. The latter showed that both meters gave similar results, typically agreeing to within a few percentage points.

Figure 9. Adaptor plug for capacitance measurements and TEK 6201 probe for charge-collection measurements.
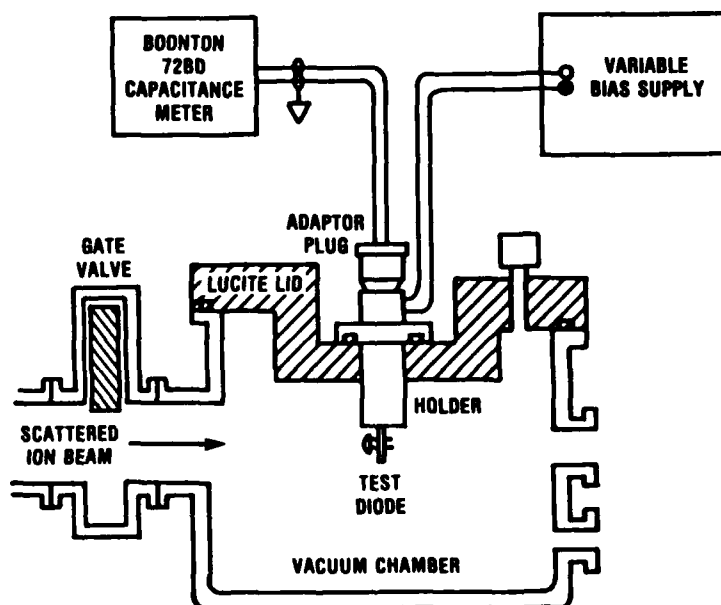

Figure 10. In-situ configuration for measuring diode capacitance.

TABLE 1. REPRESENTATIVE IN-SITU CAPACITANCE MEASUREMENTS

A. GaAs diode sample 2-1 ($N_D = 8.0 \times 10^{14}$ cm^{-3}), Cl beam

Reverse bias voltage (V)	Capacitance (pF)		Difference (%)
	Pre-exposure	Post-exposure	
0	90.64	89.84	-0.88
-1	59.64	---	---
-2	49.44	49.04	-0.81
-5	37.04	36.94	-0.27
-10	30.04	29.64	-1.33
-15	26.74	26.34	-1.49
-20	24.74	24.44	-1.21
-25	23.34	---	---
-30	22.24	21.94	-1.35
-40	20.64	20.34	-1.45
-50	19.54	19.24	-1.53

B. GaAs diode sample 1-8 ($N_D = 1.3 \times 10^{15}$ cm^{-3}), Cu beam

Reverse bias voltage (V)	Capacitance (pF)		Difference (%)
	Pre-exposure	Post-exposure	
0	124.34	122.93	-1.13
-1	78.84	---	---
-2	63.84	63.33	-0.80
-5	46.54	46.13	-0.88
-10	36.44	36.03	-1.29
-15	31.84	31.43	-1.23
-20	29.14	28.63	-1.75
-25	27.24	---	---
-30	25.84	25.43	-1.59
-40	23.94	23.53	-1.71
-50	22.64	22.23	-1.81

Reverse-bias (leakage) current was measured on each of the assembled diodes using a Tektronix 576 Curve Tracer. The purpose of this test was twofold: (1) The basic intent was to verify connectivity within the diode and the adequacy of the metal/semiconductor interface as a Schottky barrier. Surface defects on some rejected crystal samples were so large (visible to the eye) that diode leakage led to a failure of the barrier above a few volts of reverse bias. (2) The reverse-bias current-voltage characteristic is a measure of long-lived permanent radiation damage produced in semiconductor devices. Pre- and post-test comparisons of these I-V curves were recorded to provide an indication of diode sensitivity to cumulative ion exposures. Figures 11 and 12 show typical comparisons for a high- and low-doped diode bombarded with copper ions; similar results for the remaining test diodes are given in appendix C. These data showed that all diode junctions withstood their ion bombardments, showing either no change in reverse-bias leakage or a reduction.
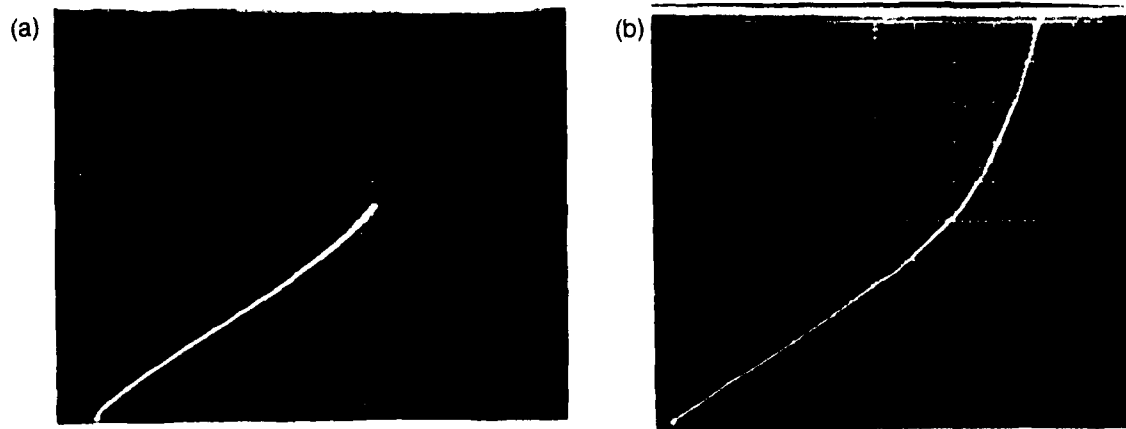
29

Figure 11. Reverse-bias I-V curves for GaAs diode 2-1 ($N_D = 8.0 \times 10^{14}$ cm^{-3}): (a) before, (b) after Cu-beam exposure.
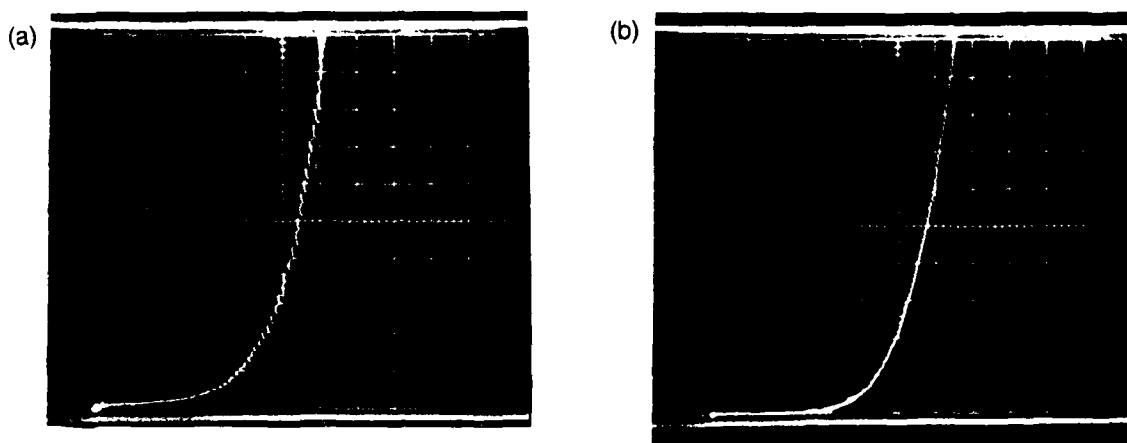

Figure 12. Reverse-bias I-V curves for GaAs diode 1-8 ($N_D = 1.3 \times 10^{15}$ cm^{-3}): (a) before, (b) after Cu-beam exposure.

3.2 Experimental Configuration

The tandem Van de Graaff accelerator at Rutgers State University, New Brunswick, NJ, was used as the source of heavy energetic ions. This accelerator is fed by a cesium-beam sputter ion source. In this source, positive cesium ions bombard a negatively biased sputter target composed (in whole or in part) of the element needed for the ion beam. Ions sputtered from the source target are passed through a thin foil to strip them of orbital electrons. Raised to a variety of relatively high positive charge states, these ions are then guided into the first Van de Graaff accelerator. Its cathode is

30

at ground potential and its anode is held at a large negative potential (typically -8 MV). After passing through this first accelerator, the partially energized ions enter a plasma region where they pick up free electrons and become negatively charged. They then enter the second Van de Graaff accelerator, which is aligned in tandem. Its electrodes are biased opposite to those of the first accelerator and bring the fully energized ion beam back to ground potential. Since electron stripping and attachment provide a range of charge states and therefore a variety of essentially discrete ion energies, a series of analyzing magnets and slits is used to isolate the desired ion-beam energy. Steering and focusing magnets then deliver the beam to any one of several vacuum beam lines for use. The heavy-ion experiments performed for this study were carried out on beam line No. 3 in the Rutgers accelerator facility.

Figure 13 shows a schematic of the heavy-ion test configuration. A thin gold scattering foil was placed in the center of beam line No. 3 a meter or so from its point of entry into the exposure laboratory. At that same location, a side drift was installed at a 20° angle. The purpose of the scatterer and side drift was to reduce the relatively high intensities of the entry beam (~10 µA particle current) to much lower levels (~10 counts/s), where isolated ion strikes on target could be resolved. The scattered beam passed through approximately 7 m of vacuum line equipped with user-controlled roughing and diffusion pumps and an assortment of vacuum valves. This vacuum system held air pressure in the beam line below ~10 mTorr to insure negligible ion energy loss during transit. A gate valve placed just in front of the test chamber was used both for isolating the chamber from the drift pipe during changes of target diodes, and to minimize damage in target diodes by blocking the scattered beam during preparation intervals.
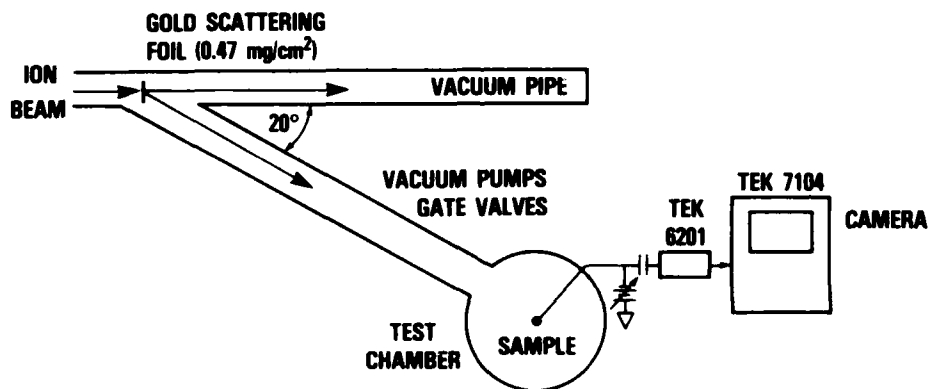

Figure 13. Experimental configuration at Rutgers State University tandem Van de Graaff accelerator facility.

Figure 14 is a photograph of the vacuum chamber used in this study. As shown, the chamber design provides for a diode holder, a pressure sensor, and a silicon surface-barrier detector for measuring beam energy. Vacuum integrity was sufficient to insure a maximum chamber air pressure of <50 mTorr

31

when the gate valve was open and the diffusion pump was operating. Figure
15(a) shows the diode holder cross-sectional design. Figure 15(b) is a photo-
graph of the assembled device. The holder was designed to provide simultan-
eously a steady-state bias on the target diode, a capacitor block to isolate
the high-frequency probe from this bias, and a short transmission line from
the diode through the direct-current block to the probe. The transmission
line feature was chosen as the best means of minimizing the bandwidth-limiting
effects of stray capacitance and inductance in the signal line. Figure 15(c)
shows the equivalent circuit for this arrangement. Figure 16 shows the layout
of the instrumentation and supporting equipment used in the experiment. The
voltage transients produced by ion strikes on the target diode were picked up
on a Tektronix P6201 probe, which has a 100-kΩ impedance and a 900-kHz band-
width. With this impedance and the 10^{-10} to 10^{-11} F capacitance of the target
diode, the probe provides an instantaneous output voltage proportional to the
cumulative charge collected on the diode. This signal was carried by a 2-m,
50-Ω, RG58U cable to a 1-GHz Tektronix 7104 oscilloscope. This instrument was
internally triggered, and its display was recorded on high-speed Polaroid film
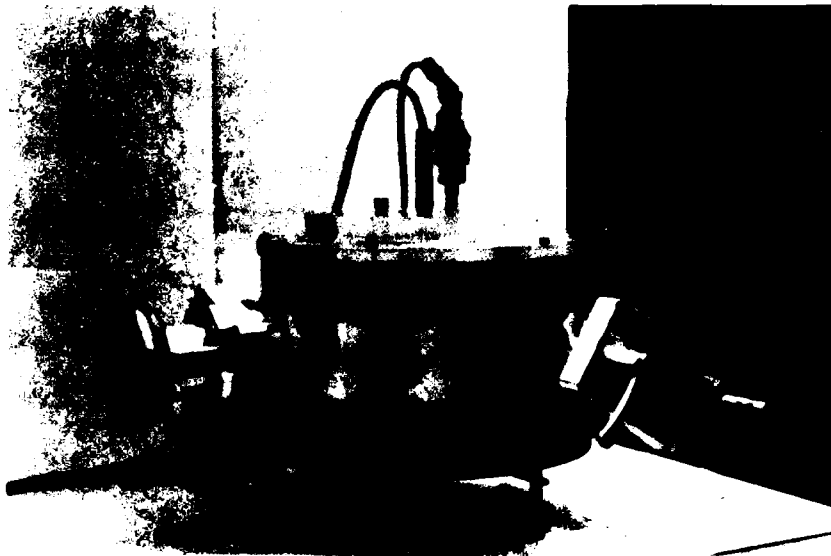with an attached F-1.2 Tektronix C-51 camera.

Figure 14. Vacuum chamber with diode holder, vacuum
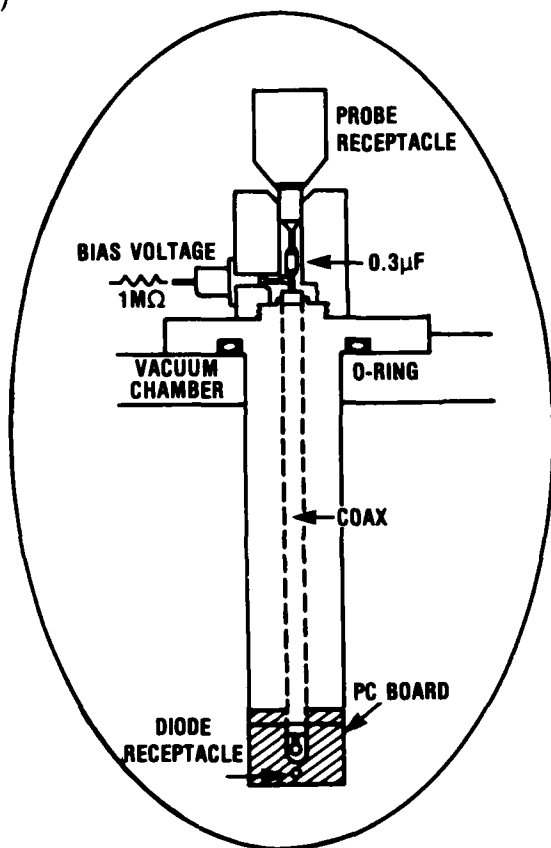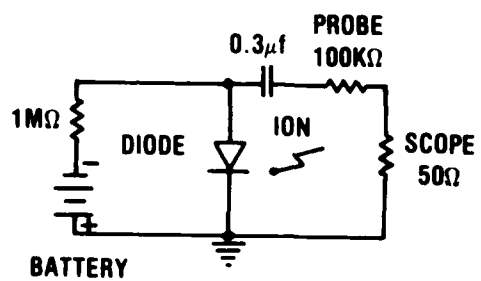gauge, and high-impedance probe.

(a)

PROBE RECEPTACLE

BIAS VOLTAGE

1MΩ

0.3μF

VACUUM CHAMBER

O-RING

COAX

PC BOARD

DIODE RECEPTACLE

Figure 15. Diode holder:
(a) cross-sectional design,
(b) completed holder, and
(c) equivalent circuit.

(b)

(c)

0.3μf

PROBE
100KΩ

1MΩ
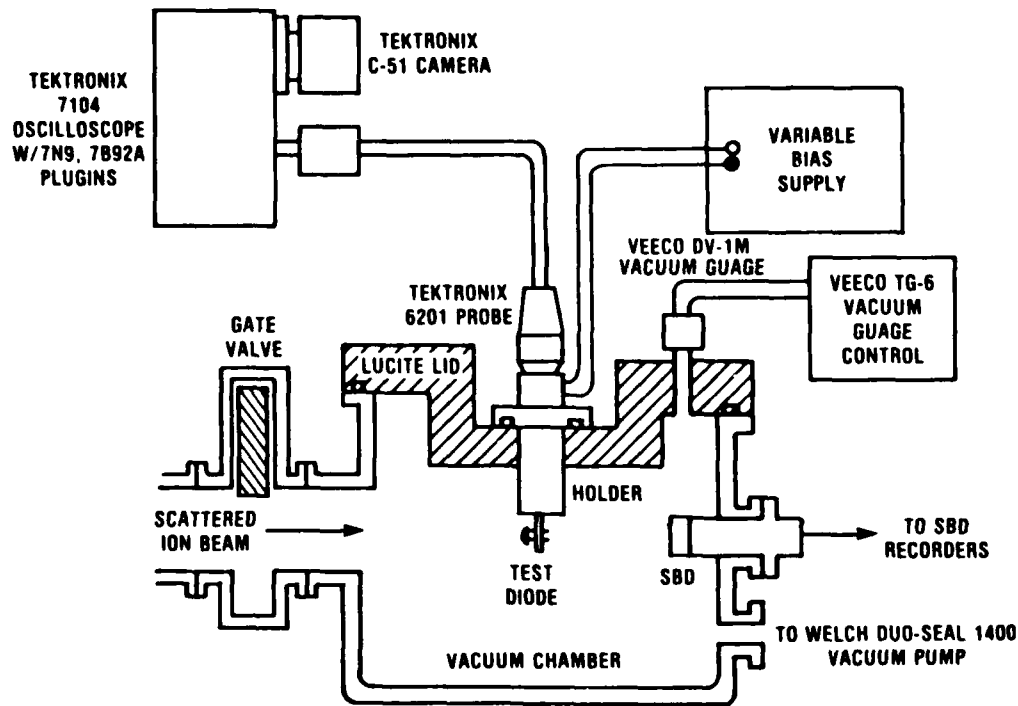
DIODE

ION

SCOPE
50Ω

BATTERY
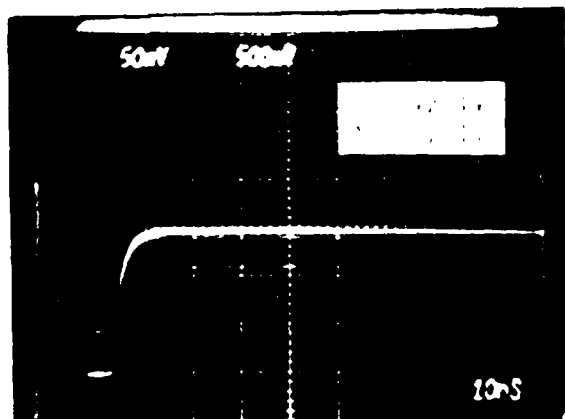
33

Figure 16.   Instrumentation layout.

3.3 Test Procedure

The procedure followed in recording a gallium arsenide diode response under given bias and beam conditions was to expose the diode to the beam with the camera shutter held open for several seconds, or until the oscilloscope trigger indicator registered 10 to 20 strikes. The resulting multiple exposure on the film invariably showed a very well-defined trace, usually having at most about 3 or 4 times the single-trace thickness, a measure of the direct-hit signal variation (see fig. 17). As with previous researchers [3, 9, and 11], the initial rise of each data trace in the first nanosecond was held to be a measure of the cumulative drift collection, including the funneled component. Figure 18 shows how the intersection of the initial rise with the interpolated mean of the ring oscillation was identified as the end of the prompt component. The subsequent slower rise of the trace was attributed to collection of charge transported into the depletion layer by diffusion. The film also typically showed a faint scattering of smaller amplitude, slower rising signals that were interpreted as near misses. The peak prompt and final diode responses were taken from the center of the trace and were converted to collected charges using the sum of measured diode and holder capacitances.
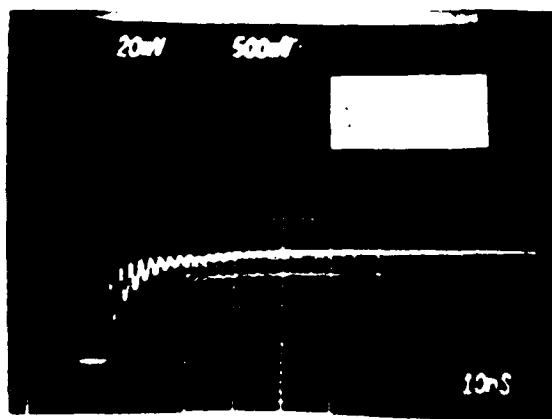
Ion energies were measured with an EG&G Ortec silicon surface-barrier detector (SBD) calibrated in vacuum using [241]Am α-particles. Figure 19 shows the instrumentation for processing and recording the pulses produced by this sensor. The output of this system was a pulse whose amplitude is proportional to the ion energy after the ion traverses the metallization of the SBD. The

34

processed pulse amplitude was recorded on Polaroid film and was also input to a multichannel spectroscopy system operated by the accelerator facility personnel.
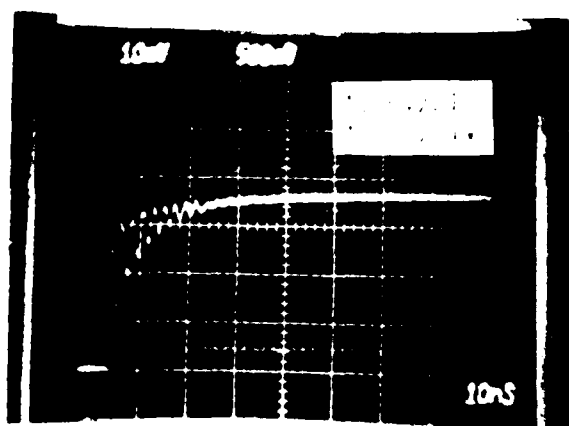
(a)

(b)

(c)

Figure 17. Typical recorded waveforms for Cl ion bombardment of (a) silicon (9×10^{13} cm^{-3}), (b) gallium arsenide (8×10^{14} cm^{-3}), and (c) gallium arsenide (1.3×10^{15} cm^{-3}).
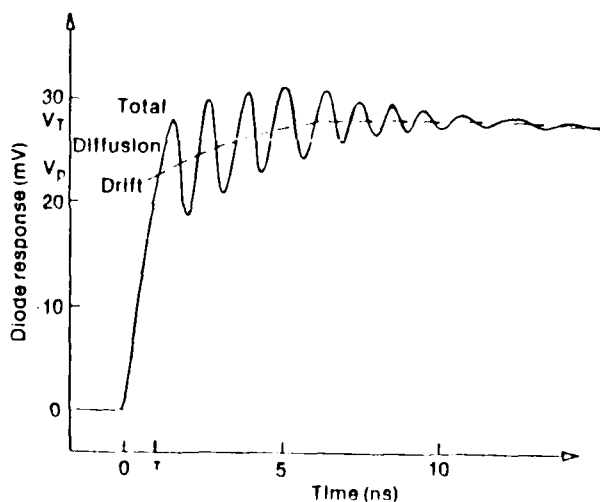

Figure 18. Separation of a nominal waveform into prompt drift (V_p) and slower diffusion ($V_T - V_p$) charge-collection components.
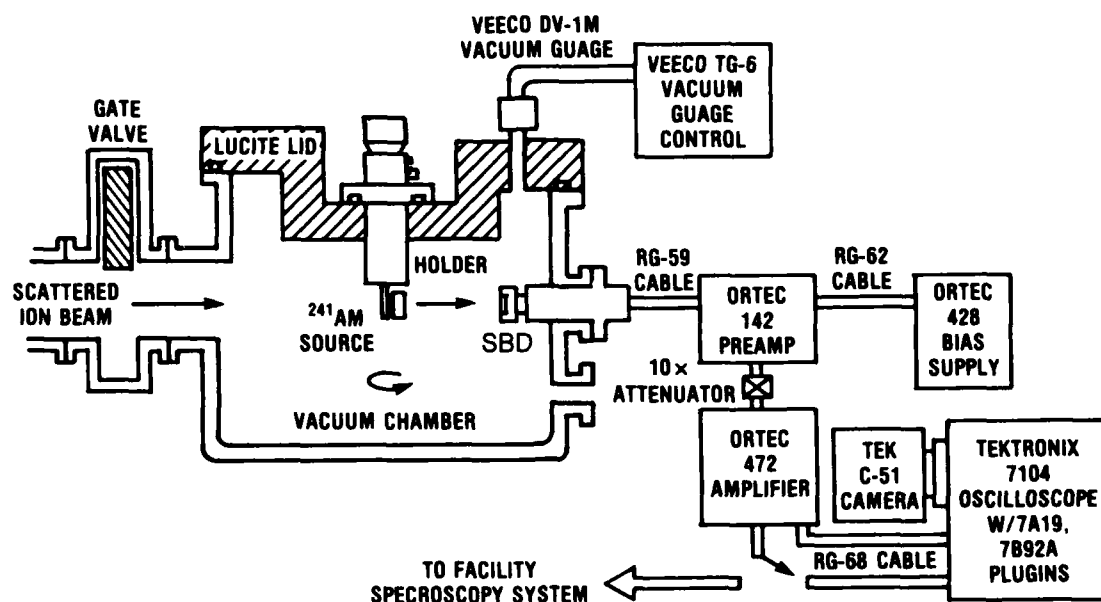
35

Figure 19. Instrumentation for processing and recording pulse generated by surface barrier detector.

The signal processing equipment was gain-calibrated using n-type silicon diodes with very low doping ($9 \times 10^{13}/cm^3$), biased high enough to insure complete enclosure of the ion track in the depletion layer. This insured prompt (drift) collection of all unrecombined charge in the track. To minimize calibration error due to ionization recombination, the gain-correction factor was taken from silicon diode responses to α-particle bombardment.

A note on ionization recombination is offered here. Recall that, in their investigation of charge collection in gallium arsenide diodes struck by α-particles, Hopkins and Srour attributed a measured 15-percent shortfall in total charge collection to Auger and radiative recombinations [11]. Based on this estimate, one would expect an even greater effect in the more strongly ionized tracks of heavy ions. Nevertheless, recombination has not been included in this analysis for several reasons. First, the 15-percent shortfall reported by Hopkins and Srour is not a decisive margin in light of normal experimental uncertainties. Second, the heavy-ion data generated by Oldham and McLean did not provide a clear indication of recombination.* Third, the Auger coefficients reported in the literature are scattered over nine orders of magnitude [11]; with that uncertainty, a meaningful evaluation of the importance of Auger recombination would be difficult. Fourth, radiative recombination produces photons, a good portion of which will be reabsorbed within a very short distance (~2 μm), producing new electron-hole pairs [11]. For these reabsorbed photons, the net effect of radiative recombination will

---

*T. R. Oldham (Harry Diamond Laboratories), private communication.

36

be only a moderate diffusing of the plasma column. Last, it is not known what influence funnel fields have on the various recombination processes. One might expect that the nonequal momenta imparted to electrons and holes by the field would reduce recombination coefficients from published values, which are typically derived for field-free plasmas. For these reasons, recombination is left an undetermined parameter in the results of this study.

4. RESULTS

The first part of this section presents the results of the preparatory calculations and measurements described above. The second part gives the results of the charge collection measurements on the silicon diodes used for system gain calibration and the gallium arsenide Schottky-barrier diodes. The last part offers a comparison between measurements and the McLean-Oldham and Hu funnel models.

4.1 Preparatory Calculations and Measurements

Table 2 summarizes the results of energy loss calculations for ion interactions in the scattering foil and in the target diode's dead layers (i.e., its surface metallization layers).

The ion energies were also measured using the test configuration given in figure 19. The more accurate alternative of the two shown was the facility spectroscopy system, which used signal processing to remove errors associated with near coincidental strikes on the SBD. The results from this system are shown in figures 20 and 21, and show O, Cl, and Cu ion energies of 18.1, 66.0, and 60.0 MeV, respectively, based on an alpha energy of 5.39 MeV. These differ from the calculated values in table 2 by 3, 2, and 2 percent, respectively.

TABLE 2.   ION ENERGIES AT KEY POINTS ALONG THEIR
TRAJECTORIES

Location	Calculated ion energies (MeV)			
	α	O	Cl	Cu
Incident on scatterer	--	20.0	70.0	70.0
After scattering foil	5.40	18.7	65.2	61.4
After diode metallization				
GaAs test diodes[a]	5.24	17.7	62.5	56.9
Si gain-calibration				
diodes[b]	5.20	16.5	61.0	52.8
Surface barrier detector[c]	5.39	18.6	64.9	60.95

[a]Dead layers: 0.370 mg/cm^2 Au, 0.035 mg/cm^2 Cr
[b]Dead layers: 0.194 mg/cm^2 Au, 0.135 mg/cm^2 Al
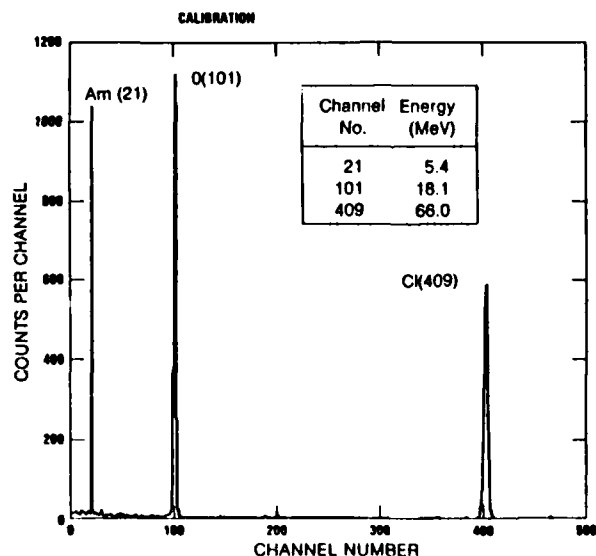[c]Dead layers: 0.040 mg/cm^2 Au, 0.040 mg/cm^2 Al

Figure 20. Energy spectra for ^{241}Am α-particles and oxygen and chlorine ions.
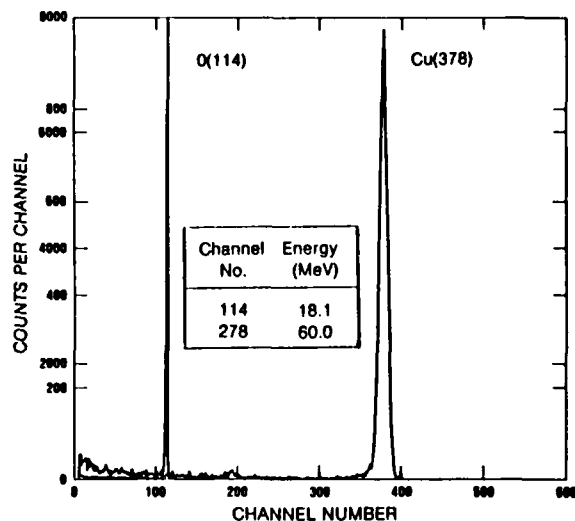
Figure 21. Energy spectra for oxygen and copper ions.

Tne second backup measurement approach called for recording the SBD amplifier outputs directl/ on the TEK 7104 oscilloscope, and scaling ion energies from estimated pulse amplitudes. Figures 22 to 25 show recorded signals for α-particles and O, Cl, and Cu ions. Their relative pulse heights are 1.0 : 3.0 : 10.8 : 10.4, which, for an α-particle energy of 5.39 MeV, suggest energies of 16.3, 58.0, and 56.0 MeV for the O, Cl, and Cu ions, respectively. These differ from predicted values by 12.4, 10.6, and 8.1 percent, again respectively.

The spectroscopy results are in quite good agreement with predicted values in table 2, while measurements based on Polaroid records of SBD pulse heights are in reasonable agreement, given the normal accuracy in reading film.

The calculated ion energies are chosen to be the baseline values because (1) calculational uncertainties are less than the experimental uncertainties in this well-defined geometry, and (2) even the measured values of ion energies at the SBD junction require two dead-layer CSDA adjustments to translate into ion energies at the GaAs and Si diode junctions.
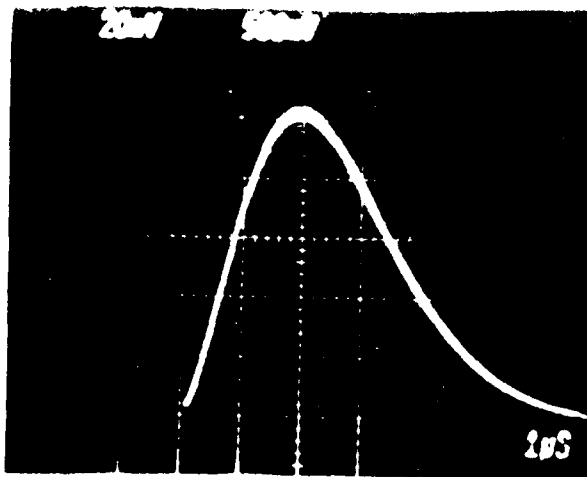
38

Figure 22. SBD output pulse after strike by ^{241}Am α-particles.
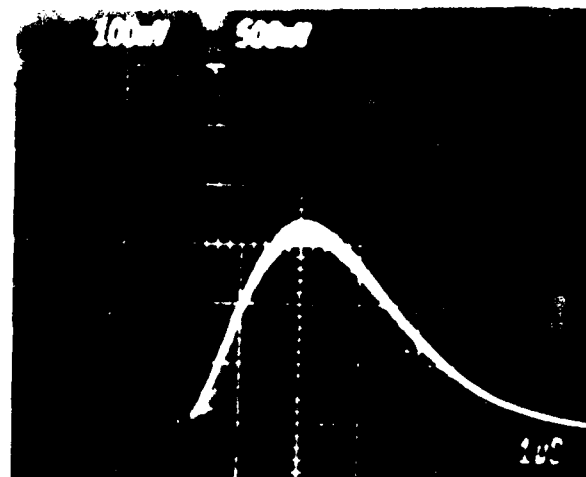

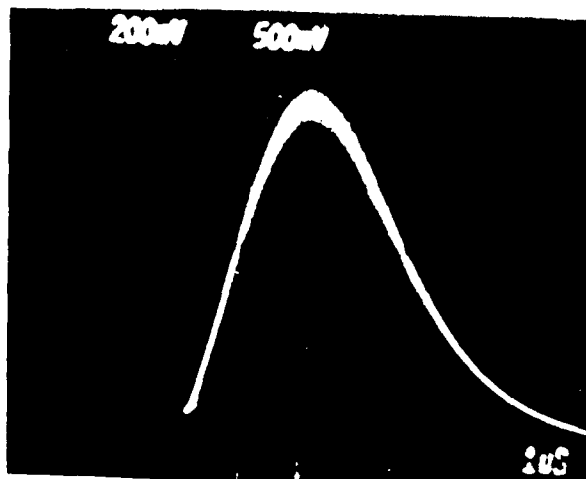Figure 23. SBD output pulse after strike by oxygen ion.

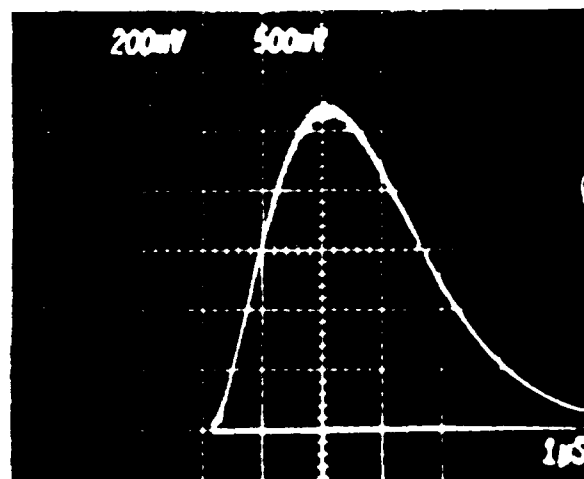Figure 24. SBD output pulse after strike by chlorine ion.

Figure 25. SBD output pulse after strike by copper ion.

The calculated energy of the ion as it crosses the diode junction serves as the starting point for the calculation of ionization line density. Figures 26 to 34 show the results of converting CSDA energy loss into plots of cumulative ionization charge as a function of ion depth into the semiconductor. The final data point in each plot represents the total ionization charge produced by the ion as it comes to rest at the end of its range. Depletion layer thicknesses and funnel lengths for given biases are readily converted to drift collection predictions by referring to the appropriate cumulative charge profile.

Figure 26. Cumulative ionization as a function of α-particle depth in silicon.

Figure 27. Cumulative ionization as a function of oxygen ion depth in silicon.

Figure 28. Cumulative ionization as a function of chlorine ion depth in silicon.

Figure 29. Cumulative ionization as a function of copper ion depth in silicon (59.6 MeV).

Figure 30. Cumulative ionization as a function of copper ion depth in silicon (52.8 MeV).
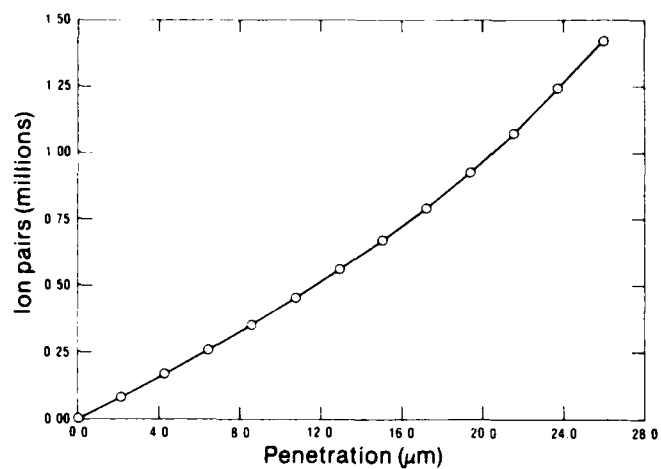

Figure 31. Cumulative ionization as a function of α-particle depth in gallium arsenide.
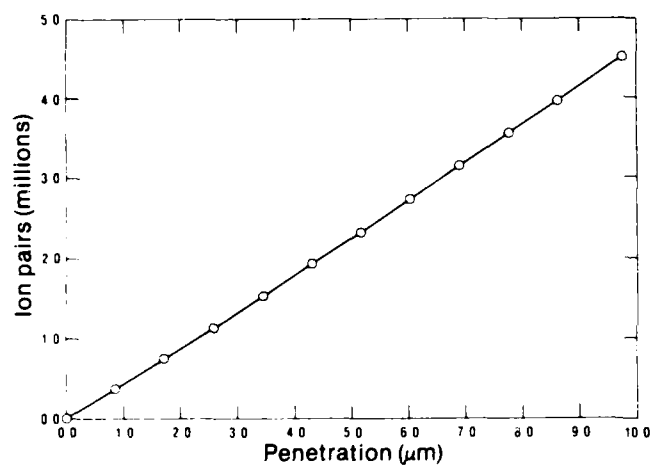
41

Figure 32. Cumulative ionization as a function of oxygen ion depth in gallium arsenide.
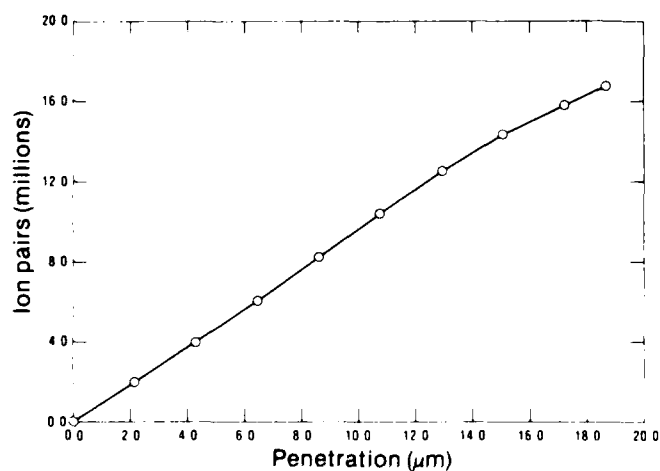

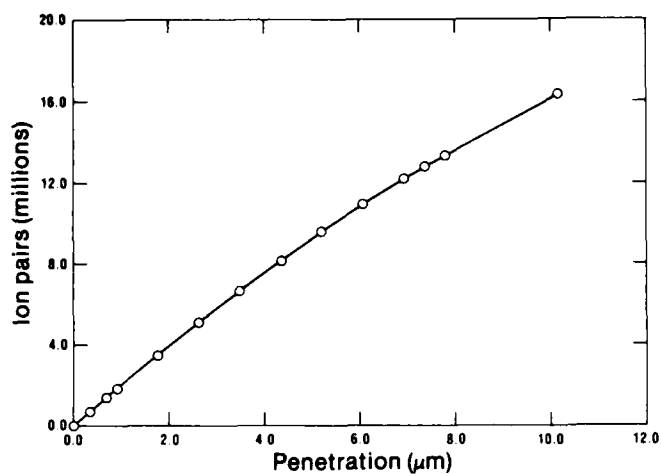Figure 33. Cumulative ionization as a function of chlorine ion depth in gallium arsenide.

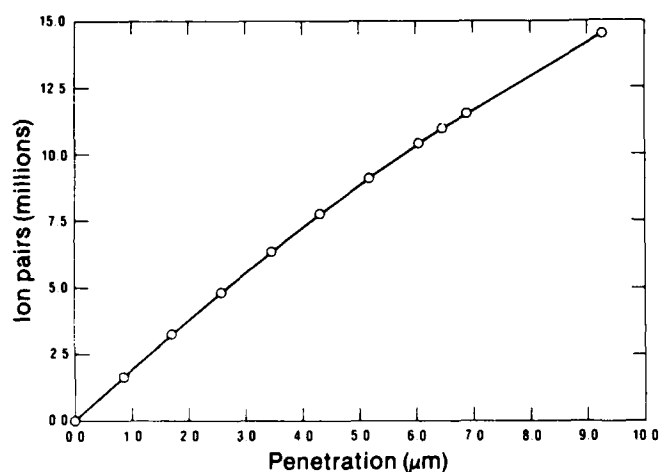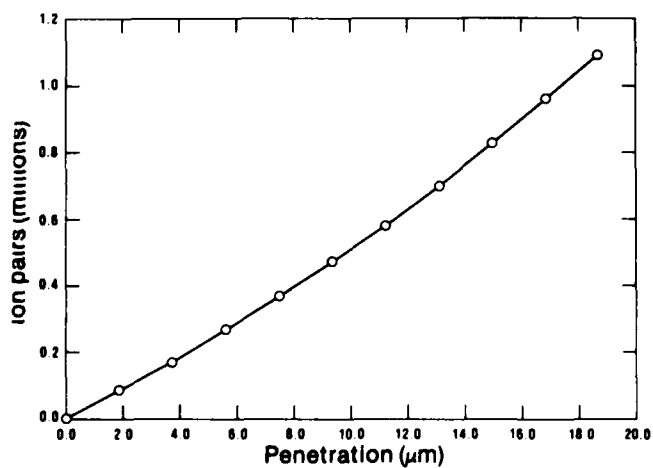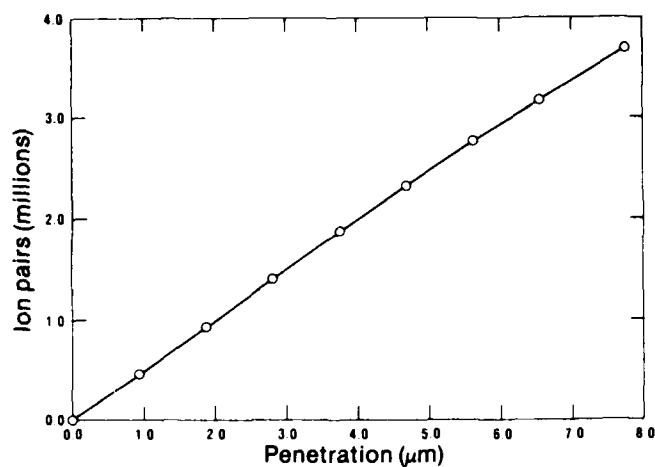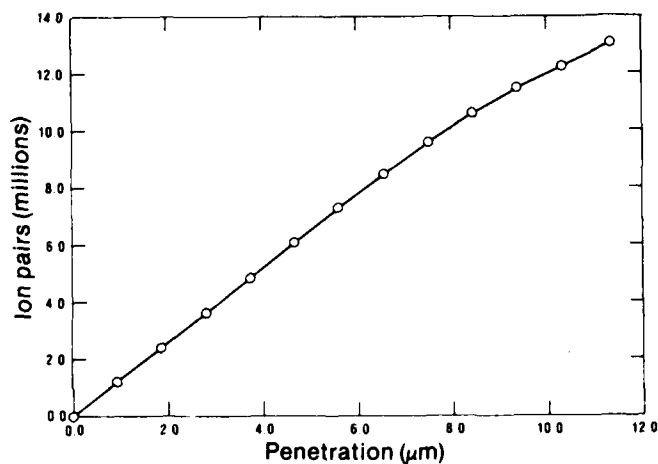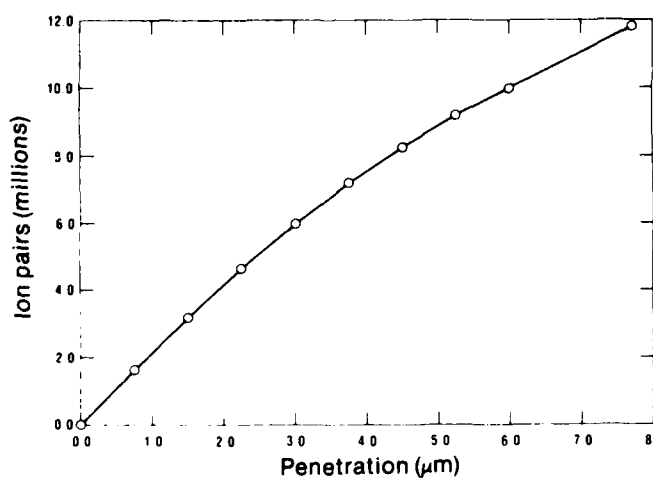Figure 34. Cumulative ionization as a function of copper ion depth in gallium arsenide.

42

4.2 Charge Collection Measurements

Figure 17 showed a typical set of oscilloscope waveforms recorded during chlorine ion bombardments of silicon GaAs diodes. The drift components of the GaAs records are limited by the risetime of the instrumentation. The damped oscillations shown in the figure invariably appeared on the GaAs waveforms; they are the result of a circuit resonance driven by the very fast risetimes of the drift collection signal in these GaAs samples. The slower silicon risetimes, which are commensurate with the silicon's lower majority carrier mobilities, did not excite this circuit resonance.

The open symbols in figure 35 represent the total charge measured as a function of bias voltage on the calibration silicon diodes. The dashed lines correspond to the calculated maximum charge produced in silicon by the ions. Measured charge collection exceeded the calculated maximum charge produced for each of the four ion species, indicating the need for a system gain-correction factor. The solid points on the graph are the open-symbol data reduced by a 0.88 correction factor, the factor required to bring the α-particle data to the assumed 100-percent collection at the highest bias.

Figures 36 through 39 give charge-collection data for the GaAs-diode bombardments. Open symbols denote actual measurements; solid points are data reduced by the 0.88 gain-correction factor. Each graph in these figures compares, for various bias voltages and a given ion species and diode dopant level, experimental prompt charge collection with calculated depletion layer charge. In every case, prompt charge collections (even the reduced values) exceed the depletion-layer curve, a clear manifestation of funneling action.

Figure 35. Total charge collection in calibration silicon diodes ($N_D = 9 \times 10^{13}$ cm^{-3}).

Figure 36. Prompt and total charge collections in GaAs diodes after 5.4-MeV α-particle strike: (a) $N_D = 8 \times 10^{14}$ cm^{-3} and (b) $N_D = 1.3 \times 10^{15}$ cm^{-3}.

Figure 37. Prompt and total charge collections in GaAs diodes after 17.7-MeV ^{16}O ion strike: (a) $N_D = 8 \times 10^{14}$ cm^{-3} and (b) $N_D = 1.3 \times 10^{15}$ cm^{-3}.

Figure 38. Prompt and total charge collections in GaAs diodes after 62.5-MeV
^{35}Cl ion strike: (a) $N_D = 8 \times 10^{14}$ cm^{-3} and (b) $N_D = 1.3 \times 10^{15}$ cm^{-3}.

Figure 39. Prompt and total charge collections in GaAs diodes after 56.9-MeV
^{63}Cu ion strike: (a) $N_D = 8 \times 10^{14}$ cm^{-3} and (b) $N_D = 1.3 \times 10^{15}$ cm^{-3}.

An unexpected feature in these GaAs data is that total charge collections at the higher biases appear to exceed the calculated values of total ionization charge in the track, even after the gain reduction factor is applied. Several observations suggest that charge multiplication is responsible. First, the slopes of the charge-collection curves do not appear to approach the saturation at high bias one expects for a fixed pool of charge available for collection. Instead, the charge collections at high bias appear to increase almost linearly, as if the charge pool is increasing with bias field. Second, the total charge values measured at the highest bias correspond closely to the total charge production given by a smaller generation rate constant: 4.2 or 4.3 eV/ion pair, instead of the 4.8 eV/ion pair used here. Eberhardt et al 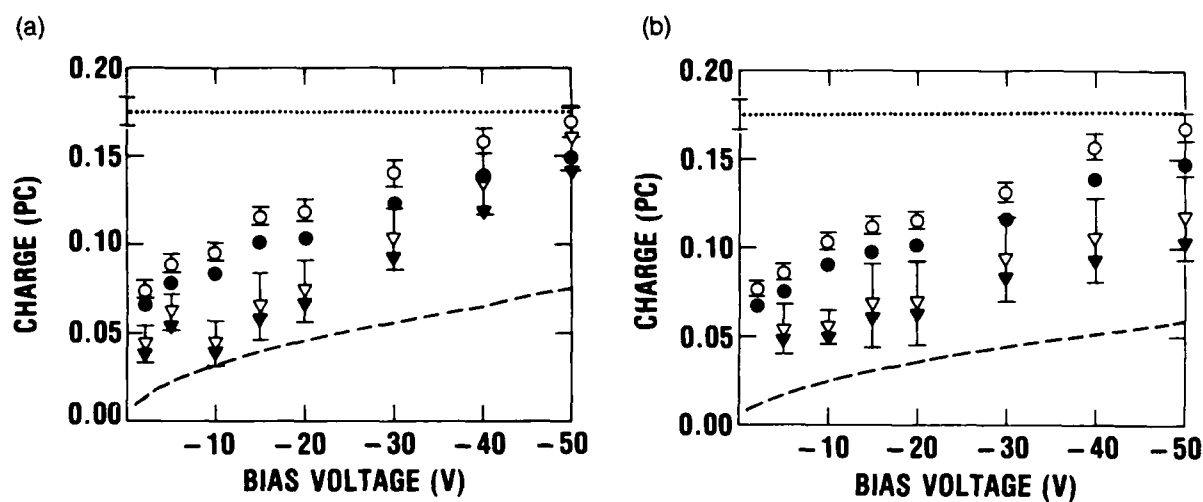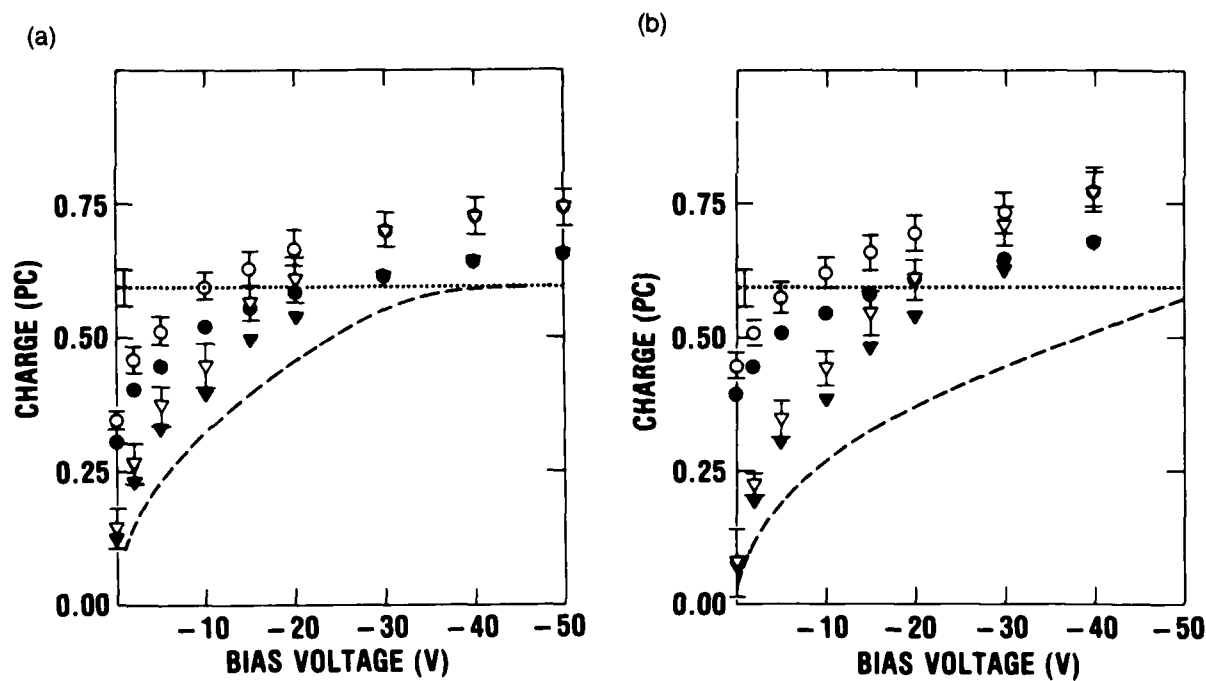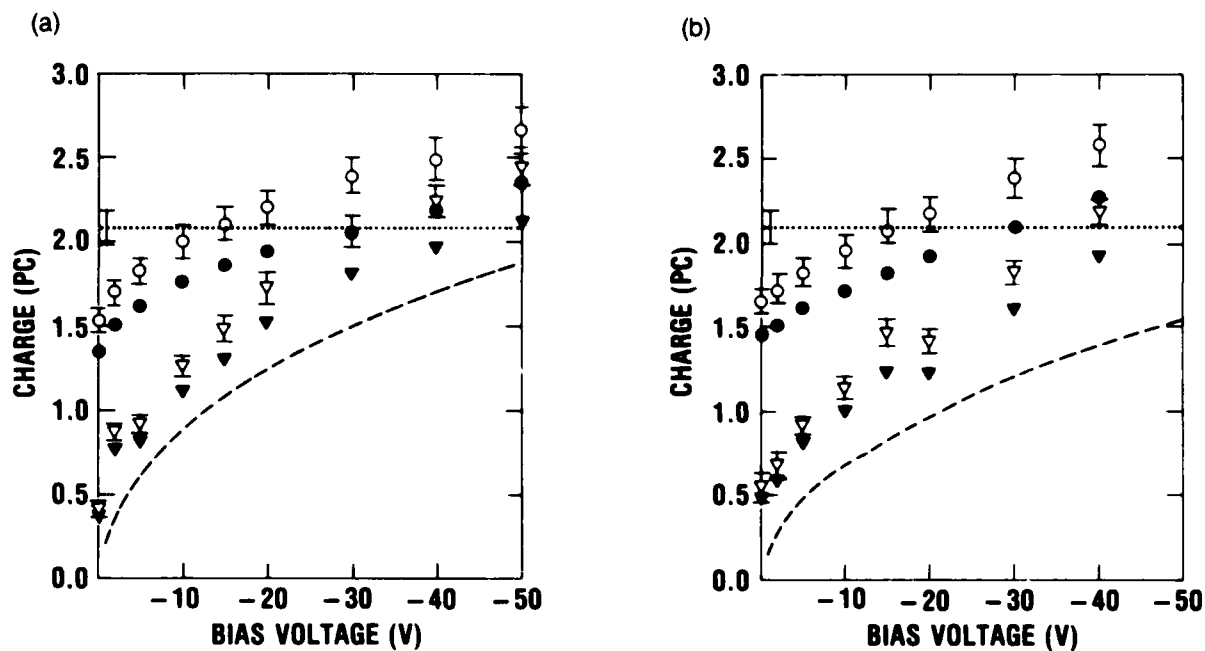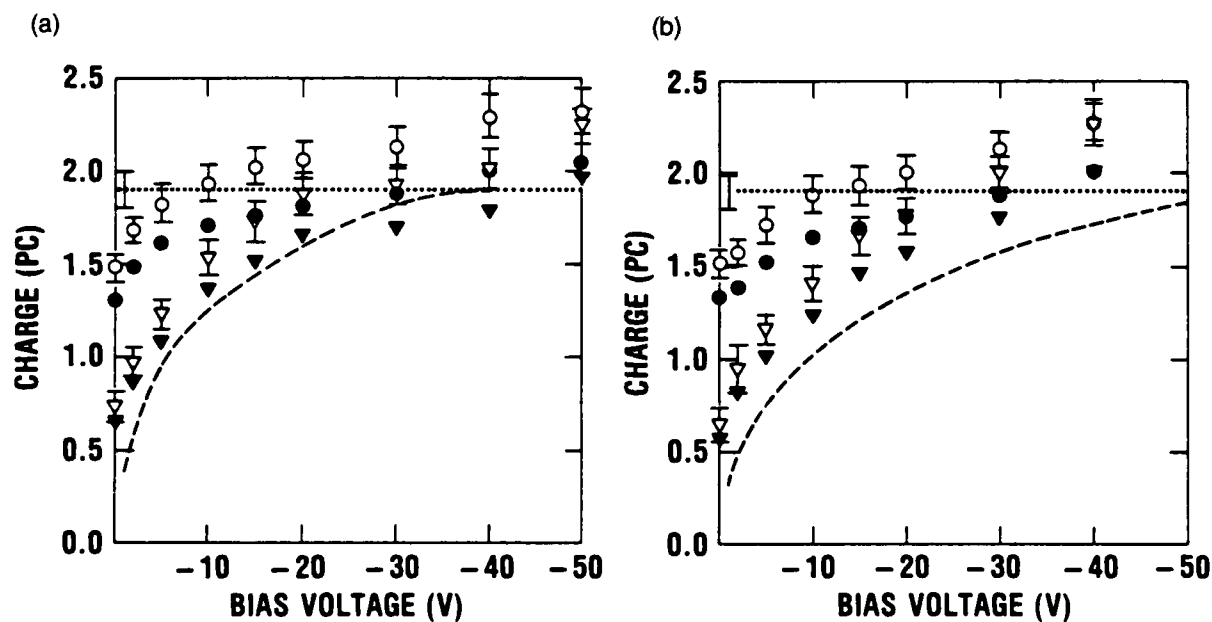measured a value of 4.27 eV/ion pair in GaAs, and did so using charge-sweeping biases just below breakdown value [25]. Third, McKay and McAfee reported a charge multiplication rate in germanium of ~10^3/cm at 10^5 V/cm [26], or a factor of ~1 to 2 for the ~10- to 20-μm track lengths obtained here. Germanium has a smaller energy band gap than gallium arsenide, 0.66 eV as compared with 1.42 eV [17], and one expects it to be more prone to charge multiplication than GaAs. Even so, a GaAs multiplication factor as low as 1.1 would raise calculated charge available for collection up to the values measured in this experiment. Finally, we observed clear signs of incipient breakdown in the GaAs diodes at -50 V bias (in fact, a few samples suffered avalanche breakdown at biases between -40 and -50 V).

These considerations support the argument that the excess charge measured in these GaAs samples was the result of charge multiplication. The charge multiplication is believed to be concentrated near crystal defects, which, when polarized by the applied field, become sites of local field intensification. This possibility is supported by the following observation. In the course of the study, a separate group of GaAs crystal samples from the same vendor was found to have a large number of surface flaws, most easily visible through a microscope at low magnification, a few visible to the naked eye. After large 1-mm-diameter metallizations were deposited on the crystals and were wire-bonded, the reverse-bias breakdown thresholds were measured. These diodes all broke down at only a few volts, while diodes from the same crystal wafer metallized with 1/4-mm contacts broke down only above 30-V reverse bias, suggesting that breakdown thresholds varied inversely with the number of defects covered by the contact.

The important observations to be drawn from the gallium arsenide data are that (1) funneling occurs in all instances, but to a lesser degree the heavier the ion, and (2) the same trend is not apparent in the silicon data presented in the literature by Oldham and McLean [10].

4.3 Comparisons of Funnel Models with Measured Data

Because the effect of avalanching in the high-bias GaAs data is not amenable to analysis using any of the models described earlier, and because the present bias range of interest in digital circuit design is limited to about 15 to 20 V, comparisons of data with funnel predictions are presented here only for the bias range from 0 to 20 V.

Comparisons between predicted and measured charge collection in gallium arsenide for this bias range are shown in figures 40 through 43 for α-particles and oxygen, chlorine, and copper ions, respectively. The point-to-point amplitude variation shown in the data, each point of which represents an average of 10 to 20 responses, is unexplained, but was shown to be reproducible when selected portions of the test sequence were repeated. The uncertainty bars reflect both the maximum variation in the direct-hit signals recorded during the multiple exposure of the film and the uncertainty in averaging out high-frequency signal oscillations.

Experimental measurements of prompt collection are matched with predictions taken from the McLean-Oldham effective funnel-length model and the Hu model. The prompt measurements show the qualitative dependence on dopant level and ion track density called for in the Hu and McLean-Oldham models, and the quantitative agreements between the α-particle data and predictions from the two models are quite good. The McLean-Oldham model gives an even greater overprediction of prompt charge for heavy-ion bombardment of gallium arsenide than the authors of the model observed for silicon. Thus, for copper and chlorine ions, their model predicts that almost all ionization charge produced in the track is promptly collected above a reverse bias of a few volts, while measured collection of prompt charge in these gallium arsenide diodes more closely follows the depletion layer contribution.
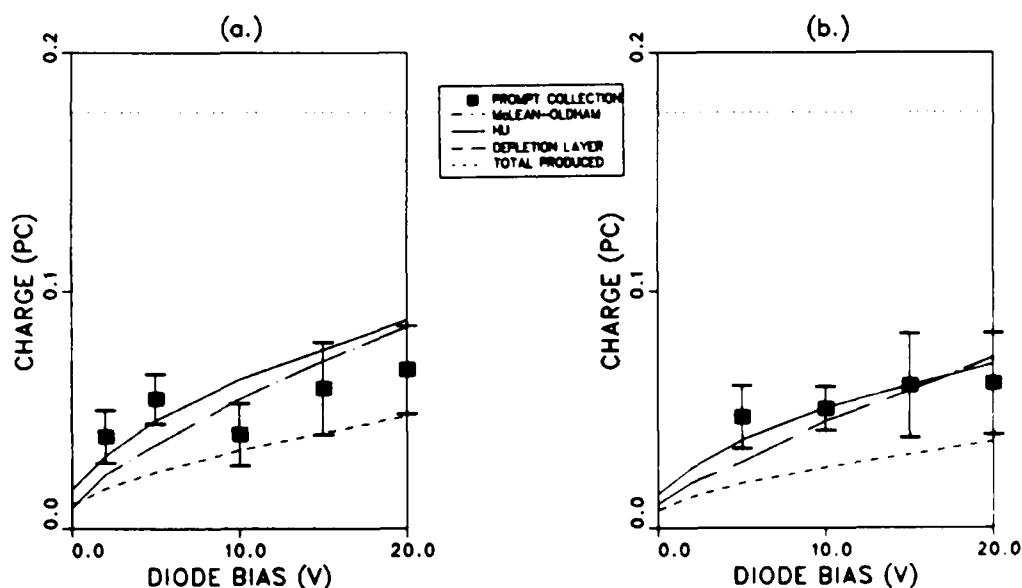

Figure 40. 5.2-MeV α-particles in GaAs: (a) $N_D = 8.0 \times 10^{14}$ cm^{-3} and (b) $N_D = 1.3 \times 10^{15}$ cm^{-3}.

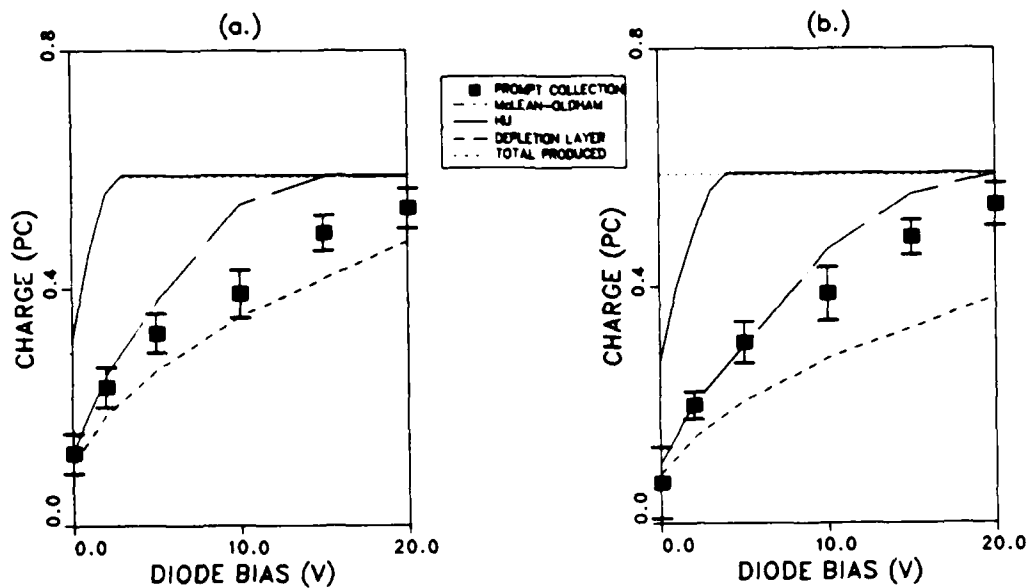Figure 41. 17.7-MeV ^{16}O ions in GaAs: (a) $N_D = 8.0 \times 10^{14}$ cm^{-3} and (b) $N_D = 1.3 \times 10^{15}$ cm^{-3}.

Figure 42. 62.5-MeV ^{35}Cl ions in GaAs: (a) $N_D = 8.0 \times 10^{14}$ cm^{-3} and (b) $N_D = 1.3 \times 10^{15}$ cm^{-3}.

Figure 43. 56.9-MeV ^{63}Cu ions in GaAs: (a) $N_D = 8.0 \times 10^{14}$ cm^{-3} and (b) $N_D = 1.3 \times 10^{15}$ cm^{-3}.

The Hu predictions were generated using equation (5), with carrier mobilities taken from figure 44 [11], depletion depths calculated using equation (31), and ionization profiles taken from figures 31 to 34. These predictions are plotted as dashed lines in figures 42 to 45. The comparisons show that the Hu model gives quite good results for both light and heavy ions between 0 and -5 V biases, giving funneling predictions consistently closer to measurements than the McLean-Oldham model. For reverse biases more negative than -5 V, the Hu model increasingly overstates prompt charge collection, although by significantly less than the McLean-Oldham model.

Figures 45 to 48 show charge collection measurements made by Oldham and McLean in n- and p-type silicon for α-particles [8] and copper ions [9,10]. Measurements in each figure are accompanied by the corresponding McLean-Oldham funnel-model predictions. As with gallium arsenide diodes, the α-particle predictions are fairly good, usually within 15 percent of measurement, while the heavy-ion predictions are again overstated, usually by factors of two or three. However, in the lightly doped p-type silicon diode (fig. 48(a)), the prompt measurement is only about 10 percent below the 100-percent collection prediction. This relatively large prompt collection in the lightly doped diode was called for in all three funnel models, because funneling action was held to persist until the track ionization density falls to the ambient doping level.

Notwithstanding these areas of agreement, it is clear that both the Hu and McLean-Oldham models consistently overpredict prompt charge collection for heavy ions in the mid-range of bias voltage.

49

Figure 44. Velocity-field relationship for carriers in GaAs (extracted from [11]).

Figure 45. 5.2-MeV α-particles in p-type Si: (a) $N_A = 8.0 \times 10^{14}$ cm^{-3} and (b) $N_A = 3.0 \times 10^{15}$ cm^{-3}.

Figure 46. 59.6-MeV ^{63}Cu ions in p-type Si: (a) $N_A = 3.6 \times 10^{14}$ cm^{-3} and (b) $N_A = 1.8 \times 10^{15}$ cm^{-3}.

Figure 47. 5.2-MeV α-particles in n-type Si: (a) $N_D = 1.0 \times 10^{15}$ cm^{-3} and (b) $N_D = 4.0 \times 10^{15}$ cm^{-3}.

Figure 48. 59.6-MeV ^{63}Cu ions in n-type Si: (a) $N_D = 4.7 \times 10^{14}$ cm^{-3} and (b) $N_D = 2.8 \times 10^{15}$ cm^{-3}.

5. DISCUSSION

In this section, an attempt is made to explain why the Hu and McLean-Oldham models overpredict funneling in heavy-ion tracks. First, an alternative description of funneling is given that is believed to be more relevant to the diodes and test circuitry used in these experiments. This funneling representation is shown to be compatible with a plasma screening mechanism, which is offered as an explanation for the reduced prompt charge collections observed in these experiments. Finally, the McLean-Oldham model modified with a plasma-screening factor is compared to measured data.

5.1 Funneling in Transiently Isolated Diode

The Hu and Messenger models described in the first section were built up from an important common assumption, that the electric field in the depletion layer drives majority carriers into the initially neutral region. While their model did not explicitly require it, McLean and Oldham also envisioned majority carriers being driven into the substrate toward the buried electrode [9]. It is not surprising that these independent investigators of the funnel phenomenon shared this common view, because it was developed explicitly in the two-dimensional computer solutions published earlier by Hsieh, Murley, and O'Brien [3-5]. These solutions were presented as spatial plots showing electric potentials and majority carrier distributions extending into the substrate at various times after an α-particle strike (recall fig. 1). The key point here is that this aspect of the collection process was the direct consequence of a particular and important boundary condition: the junction bias potential was assumed to be held at a constant value through the event.

52

This bias condition does not appear to be an assured option in typical circuit applications, for the following reasons. The bias circuit loop is usually external to the device package. In addition to intentional circuit elements, the bias loop unavoidably includes reactive and resistive components due to stray inductance, resistance, and capacitance. Consequently, the bias circuit impedance in one extreme is likely to slow the rise of a large replacement current to beyond the end of the prompt response; in the other extreme, it limits the fast-rising bias current amplitude to such a low level that negligible charge is restored to the junction node during the extremely short-lived prompt charge-collection process. Figure 15(c) shows a 1-MΩ resistor in the bias loop; it was placed there to decouple the bias circuitry from the signal channel. It gives the bias circuit a fast time constant of $~10^{-12}$ s ($~10^{-6}$ H stray inductance $\div$ 10^6 Ω), but limits bias current amplitudes to $~100$ μA or less (0.1-V diode response $\div$ 10^6 Ω). The finite electric-signal propagation speed (c) further increases the time required to restore charge to the node. Consequently, the latter extreme condition is held to apply to the experiments conducted in this study. Accordingly, an alternative description of drift collection is developed below to account for the transiently isolated junction.

Two conditions are assumed to apply: (1) The time required for the bias circuit to replace collected charge on the junction is assumed to be long compared to the duration of drift collection; i.e., during the event, the junction is transiently isolated from the rest of the circuit. (2) The lateral dimensions of the diode are sufficiently large that the bias charge on the junction is much greater than the free charge produced in the ion track. Thus, the charge collection that follows the ion strike does not substantially alter the potential difference across the junction and the overall field distribution.

Figure 49 shows the track of a light ion (e.g., α-particle), assumed for simplicity to be perpendicular to the plane of the junction. A reverse-biased p^+n Schottky-barrier diode is depicted. After the initial track ionization is thermalized, a process that occurs in times of the order of 10^{-12} s and leaves the track with a radius of about 0.1 μm [6], early carrier transport effects include the following: (1) The plasma column in the depletion layer is polarized almost instantly (about as fast as it is created), excluding the positive donor charge in its interior. This charge "surfaces" at the junction and recombines with an equal negative charge on the electrode. The neutralization of this track volume results in an unbalanced radial field component in the depletion layer directed in towards the track axis. (2) Ionization electrons in the same part of the track are attracted by the surrounding charged donors (i.e., they respond to this radial field component) and drift radially outward into the depletion layer, neutralizing charged donors there. (3) At an equal rate, ionization holes produced in the depletion layer are attracted to the negatively charged metal contact layer. (4) On a much slower time scale, the column begins a relatively slow expansion as ambipolar diffusion takes place.

In this early phase, most of the electrons leaving the track come from that segment lying in the original depletion layer; carriers well beyond the depletion layer initially see no field and are not affected. In this and subsequent phases of charge collection, rates of hole collection at the surface and the radial drift of electrons out of the track are approximately equal, so that the track plasma remains essentially neutral inside its sheath [27]. The sheath is defined here simply as the exterior layer of the plasma column where electrons leave the neutral plasma under the influence of radial fields. Funneling occurs as this electron space charge "fans out" and neutralizes part of the positively charged donor distribution near the track (a process that takes tens of picoseconds). Some of the field lines associated with local electron

Figure 49. Charge distribution and movement in a reverse-biased diode after an ion strike perpendicular to plane of p^+n junction.

charges on the metallization then no longer terminate on charged donors in the original depletion layer, but instead extend into the formerly neutral region. Alternatively, one may picture (in superposition) the majority carriers that have left the column as creating their own additional depletion volume in what was initially neutral space. Either way, the result is a bulge on the original depletion layer centered on the track. As in step (2) above, track electrons there are then subjected to a radial field and are pulled out of the plasma, while their hole counterparts are funneled up the track toward the surface. The resulting increase in space charge further extends the bulge. The consequence of this cause-and-effect cycle is an extension of a longitudinal field up the track into the initially neutral region and a resulting increase in prompt (drift) charge collection over and above that provided by charge in the original depletion layer.

Conservation of current in this transiently isolated junction requires a necessarily local closure of current paths. The charge motions described in figure 49 define the closed conventional-current loop shown in figure 50(a): a radial "fan-out" of electron current out of the track into the depletion layer, a hole current up the track and across the junction, a radial inward-directed electron replacement current on the electrode, and, closing the loop, a displacement current normal to the junction. This last current segment is the relatively small time-rate-of-change of the electric displacement $\vec{D}$ in the depletion layer due to the partial neutralization of charge on the junction, integrated over the area of the diode (one notes that $\partial\vec{D}/\partial t$ is always directed opposite to $\vec{D}$). The diode current paths drawn in 50(a) suggest a simple analogy, which is shown in figure 50(b). Here, two oppositely charged metal plates are suddenly shorted by a long nail, which
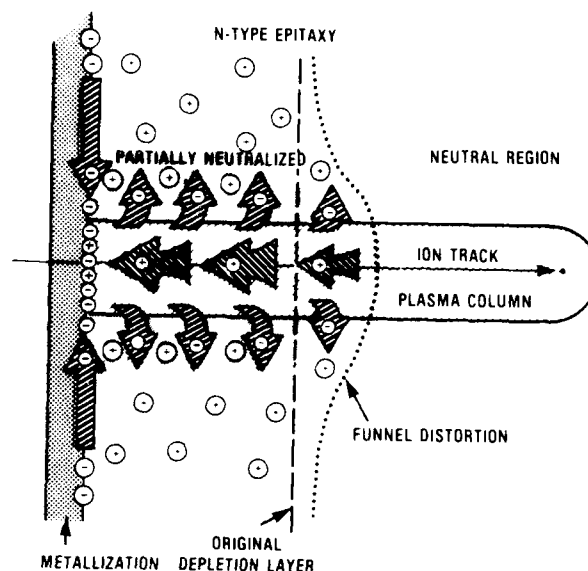
54

(a) METAL CONTACT EPITAXY DEPLETION LAYER NEUTRAL REGION

ION PATH
IONIZATION COLUMN

REVERSE-BIASED
SCHOTTKY-BARRIER DIODE

(b)

ANALOGOUS PARALLEL-PLATE CAPACITOR
WITH SHORTING NAIL

Figure 50. Electron and hole current distribution: (a) in reverse-biased
junction after ion strike; and (b) in an analogous shorted parallel-plate
configuration.

represents the heavy-ion track. This analogy obviously cannot provide for
either the discharge-limiting effects of the Schottky barrier, the depletion-
layer bulge (the funnel), or the hole current in the ion track. Nevertheless,
the picture gives a good representation of the closed SEU current loop in
large diodes transiently isolated from their bias circuitry. It shows how the
electric field in the nail would be largely confined to that current-carrying
portion lying between the two charge layers, rather than to the tip of the
nail.

In the diode, as the last of the drift and diffusion charge is col-
lected, the depletion region is reestablished as a uniform, slightly thinner
layer across the entire diode area, and the potential difference across the
junction settles at the original value minus ~Q/C, the ionization charge col-
lected divided by the junction capacitance. In due course, the electron
current in the bias loop produced by this voltage drop replaces the missing
(recombined) charge on the junction and the full junction bias is restored.

5.2 Plasma Screening of Funnel Fields

If the incident particle is now assumed to be a heavy ion, i.e., any
ion heavier than beryllium, the ionization density is substantially greater
than that in α-particle tracks, and the drift charge collection predicted by
the Hu and McLean-Oldham models is not fully realized. The suggestion here is

55

that the smaller collection may be explained by a plasma screening effect that prevents the full extension of the funnel field down the track into the neutral region. Figure 51 shows qualitatively how the field, potential, and charge distributions might be altered by plasma screening near the end of the funnel. As the funnel field begins to extend into the neutral part of the track, and carriers there are set in motion, a quasi-static shift in the charge distribution occurs, wherein minority-carrier holes (on time average) are brought closer to the electrode as electrons are simultaneously pushed away from the electrode and separated radially. This time-averaged polarization shift of charge density screens the field--the termination of field lines on minority carriers is now accomplished closer to the surface--and carriers beyond do not see a collection field.

Figure 51. Plasma screening during funneling: (a) electric field, (b) electric potential, and (c) net charge distribution.

A quantitative measure of this screening effect may be found by referring to the phenomenon of plane-wave attenuation in a conducting medium and the concept of skin depth. It is well known that a plane wave is rapidly attenuated as it propagates into a good conductor [31]. The attenuation factor f varies with propagation distance x according to

$$f = e^{-x/\delta} , \qquad (32)$$

where $\delta \sim (T/\pi\mu\sigma)^{1/2}$ is the skin depth, and T, μ, and σ are the plane wave period, the permeability of the target material, and its conductivity, respectively. Admittedly, the situation that exists in a semiconductor device after a heavy-ion strike differs from the case of the plane wave in a conductor: the electric field of the plane wave is transverse and oscillatory, while in

56

the diode depletion layer, the electric funnel field is longitudinal and short-lived. Nevertheless, there is a similarity in the two situations that suggests the use of an effective plasma attenuation factor of the form given above for the funnel field in the ion track. In both cases, free carriers move during a well-defined time interval to neutralize the field at their locations. In both cases, the extent of this neutralization is controlled by the conductivity and a critical time period. The greater the conductivity, the stronger the neutralization of fields and the shorter the distances into the two media that the fields can reach.

Analogous to the plane-wave period T in equation (32), the characteristic screening period is chosen to be the time it would take a minority carrier in the plasma column to drift to the surface from a maximum distance L. L is the length of track required to provide the quantity of charge predicted by the McLean-Oldham model which is chosen as the baseline model to modify. One notes that L is not that model's effective funnel length, L_c, which can exceed the track length for heavy, short-range particles. The screening period is then

$$\tau = \frac{L}{\langle v_{mic} \rangle} \ . \tag{33}$$

Here the average minority carrier drift velocity $\langle v_{mic} \rangle$ is found by applying an appropriate value for the average field to the velocity-field relationships for gallium arsenide given earlier (fig. 44). The average field value used for this purpose is

$$\langle E \rangle = \frac{1}{2} \frac{V_o}{L} \ , \tag{34}$$

where V_o is the applied bias.

To complete the derivation of a screening factor, a characteristic length is required. Since L was used to derive τ, and since the funnel field is assumed to collect charge from as far down the track as the distance L in the absence of screening, it follows that L is the obvious choice for the unscreened field penetration depth. The result is an expression for an attenuation factor f_s due to screening given by

$$f_s = e^{-L/\delta} \ , \text{ with } \delta = (\tau/\pi\mu\sigma)^{1/2} \ . \tag{35}$$

In this expression, the permeability is taken to be that of free space, and the conductivity is the low-field limit of conductivity due to the initial hole and electron densities.

This reduction factor can now be applied to the funnel contribution in the following expression for the total prompt charge Q_p:

$$Q_p = N_o[x_D + f_s(L - x_D)] \ , \tag{36}$$

57

where N_o is the initial ionization line density found using the CSDA and x_D is the initial depletion layer thickness, as calculated using equation (31). The justification for applying an electric field attenuation factor to a collection length is that the funnel portion of L is directly proportional to the electric field through the minority carrier drift velocity, at least for velocities significantly less than the saturation value (see eq (2), McLean and Oldham [9]).

One may ask what changes to the picture developed above would follow if the two conditions assumed at the outset did not apply. If the first condition does not apply, and charge can be replaced on the junction as fast as it is collected, then a prompt field is produced by the replenished charge directly across the active and substrate layers lying between the diode contacts. This is the case described by Hsieh et al [3-5]. This field causes majority carriers to stream out of the track directly into the substrate, where they are collected at the buried electrode. Their almost immediate presence along the whole length of the track creates a much more direct and rapid growth of funneling than is depicted in figure 49. One then expects a weaker longitudinal electric field along the full length of the track, and a much stronger field at its tip. This is analogous to the plate on the right side of figure 50 being re-identified as the buried contact and the nail (track) being shortened so that it reaches only a short distance into the space between the plates. As in figure 1, very little potential drop occurs over the length of the nail; most of the potential drop (and field) occurs at and beyond the nail tip. In the diode, the field (and the currents that follow it) spread and thin from the end of the track on toward the substrate electrode, following the spreading resistance pattern described qualitatively by Messenger [8].

More recently, Grubin et al [29] have modeled this same problem with a finite-difference computer code similar to that used by Hsieh et al. They held their n^+p junction at constant bias through the event (again, equivalent to an assumption of instantaneous replacement of the collected charge), and calculated time-dependent currents through the substrate, i.e., across the diode contacts. They concluded that these currents are more directly controlled by junction bias and the substrate parameters (resistivity, thickness, etc) than by the details of the track geometry and density. Thus, if one can hold the junction bias constant through an ion strike, the prompt response is a fast-rising current pulse in the diode circuit, rather than the sudden potential drop developed across the isolated diode junction. Another difference is that the plasma screening treatment developed above would not be directly applicable because the highest field is now developed off the tip of the ion track, where no ionization density exists. In this case, one then expects the 100-percent collection predicted by the McLean-Oldham model. This follows because the funnel field is produced by free charge carriers in the high field region. The funnel cannot readily collapse faster than these free carriers can disperse. Thus, the collection field, which now extends beyond the track, cannot reasonably relax back to the initial planar depletion layer configuration without completely sweeping out the track ionization lying in the initially neutral region.

If the second condition does not apply, i.e., if the diode is so
small that the charge in the ion track is a significant fraction of the total
charge on the reverse-biased junction, then the collection process itself
depresses the collection field; the process becomes self-dampening. A cred-
ible treatment therefore requires a finite-difference self-consistent calcula-
tion that is only reasonably performed on a modern, high-speed computer.
Since the diodes used in this study were easily large enough to insure the
applicability of condition 2, this case will not be further discussed.

5.3 Comparisons of Screened Funnel Model with Measurements

Predictions of prompt charge collection based on the plasma screening
modification to the McLean-Oldham model have been plotted in figures 52 to 55
for α-particles and oxygen, chlorine, and copper ion bombardments in gallium
arsenide, respectively. Also shown for comparison are the corresponding
measured data and predictions derived with the McLean-Oldham model.

As expected, plasma screening as it has been modeled is seen to have
only a modest effect on predictions for α-particles, giving results that still
fall near the measured data. For the heavier ions, the screening effect is
much more pronounced. Where the unscreened model predicts 100-percent drift
collection at all biases above a few volts, the screened-funnel predictions
fall considerably lower and much closer to the measurements. Compared to
measured data, the screening treatment moderately overpredicts low-bias
collection and, to a lesser extent, understates collection at high bias.

Figure 52. 5.2-MeV α-particles in GaAs: (a) $N_D = 8.0 \times 10^{14}$ cm^{-3} and
(b) $N_D = 1.3 \times 10^{15}$ cm^{-3}.

59

Figure 53. 17.7-MeV ^{16}O ions in GaAs: (a) $N_D = 8.0 \times 10^{14}$ cm^{-3} and (b) $N_D = 1.3 \times 10^{15}$ cm^{-3}.
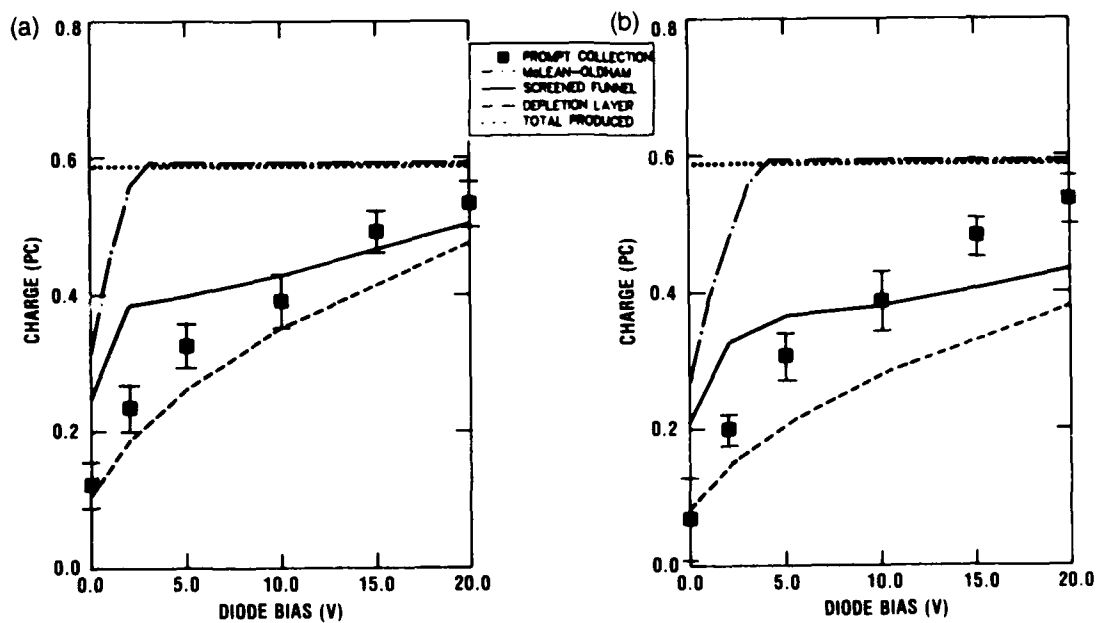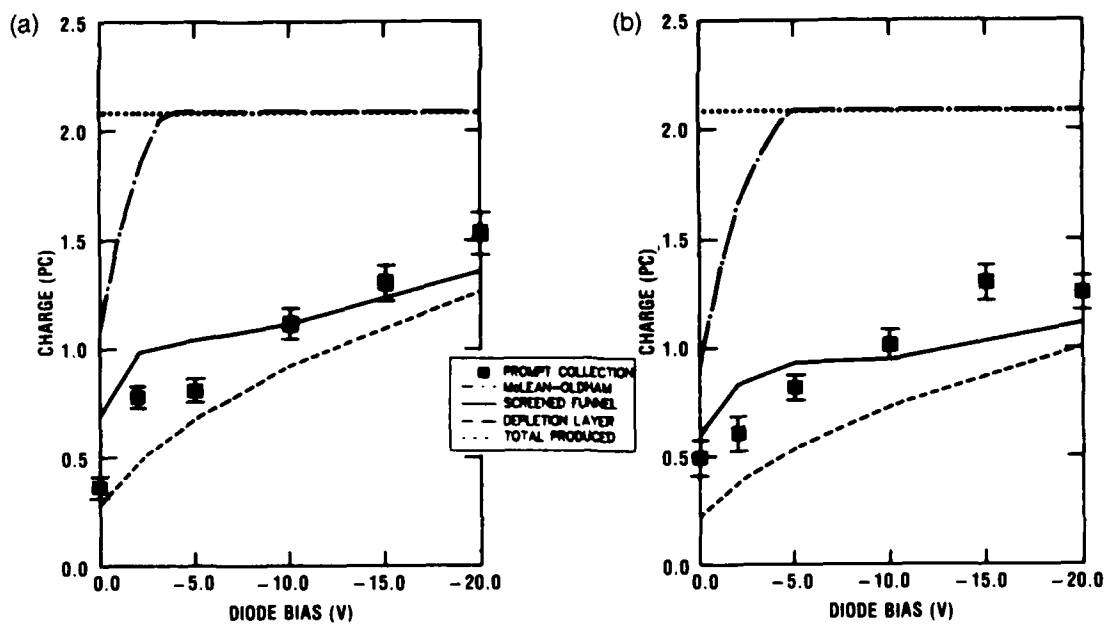

Figure 54. 62.5-MeV ^{35}Cl ions in GaAs: (a) $N_D = 8.0 \times 10^{14}$ cm^{-3} and (b) $N_D = 1.3 \times 10^{15}$ cm^{-3}.
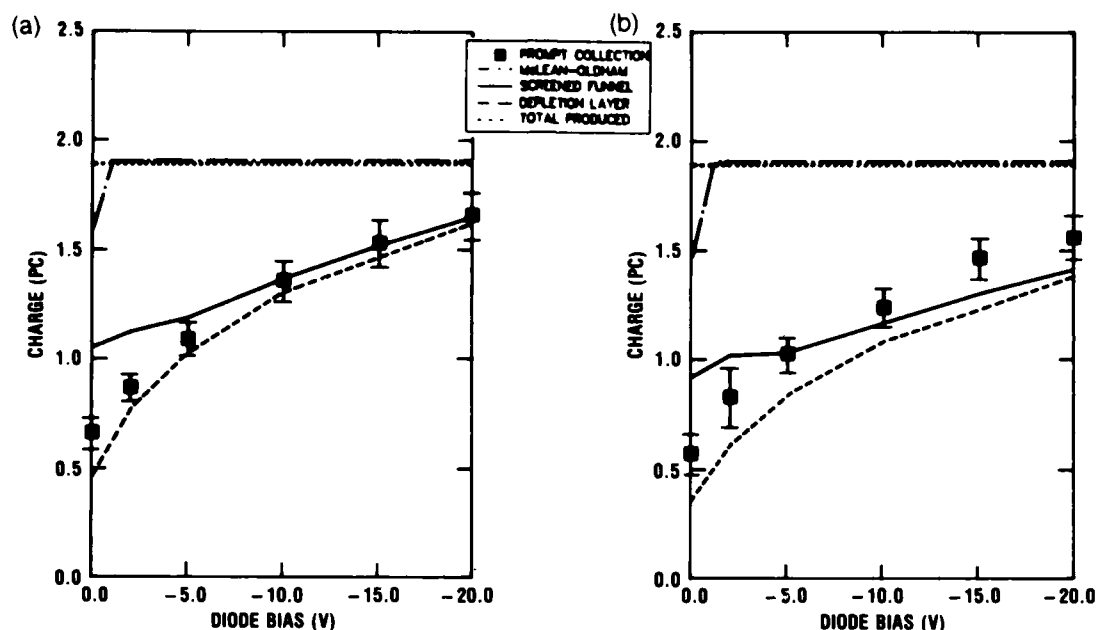
Figure 55.   56.9-MeV ^{63}Cu ions in GaAs: (a) $N_D = 8.0 \times 10^{14}$ cm^{-3} and (b) $N_D = 1.3 \times 10^{15}$ cm^{-3}.

Figures 56 to 59 show comparisons between experimental data on silicon from Oldham and McLean [10]* and predictions from both the McLean-Oldham model and that model modified by the plasma-screening factor.   The performances of the two funnel treatments are much the same in silicon as in gallium arsenide.   In both n-type and p-type silicon, the screened-funnel predictions for α-particles are shifted down only slightly from the McLean-Oldham funnel predictions, and the screened-funnel predictions for copper ions again are moderately overstated at low bias and understated at higher biases relative to the measured data.   The agreement seems to be better in the n-type silicon. In figures 57 and 59, the screened funnel predictions also show a negative slope at intermediate biases.   This effect derives from the application of the screening factor to just the funneled portion of the prompt charge predicted by the McLean-Oldham model.   At these biases, the decrease in this product more than offsets the increase in the depletion-layer contribution.   The overall result of the treatment, nevertheless, is an improvement in the prediction accuracy for heavy ions in n-type silicon, and a slight improvement for heavy ions in p-type silicon at the lower biases.

---

*F. B. McLean (Harry Diamond Laboratories), private communication.

Figure 56. 5.2-MeV α-particles in n-type Si: (a) $N_D = 1.0 \times 10^{15}$ cm^{-3} and (b) $N_D = 4.0 \times 10^{15}$ cm^{-3}.

Figure 57. 59.6-MeV ^{63}Cu ions in n-type Si: (a) $N_D = 4.7 \times 10^{14}$ cm^{-3} and (b) $N_D = 2.8 \times 10^{15}$ cm^{-3}.
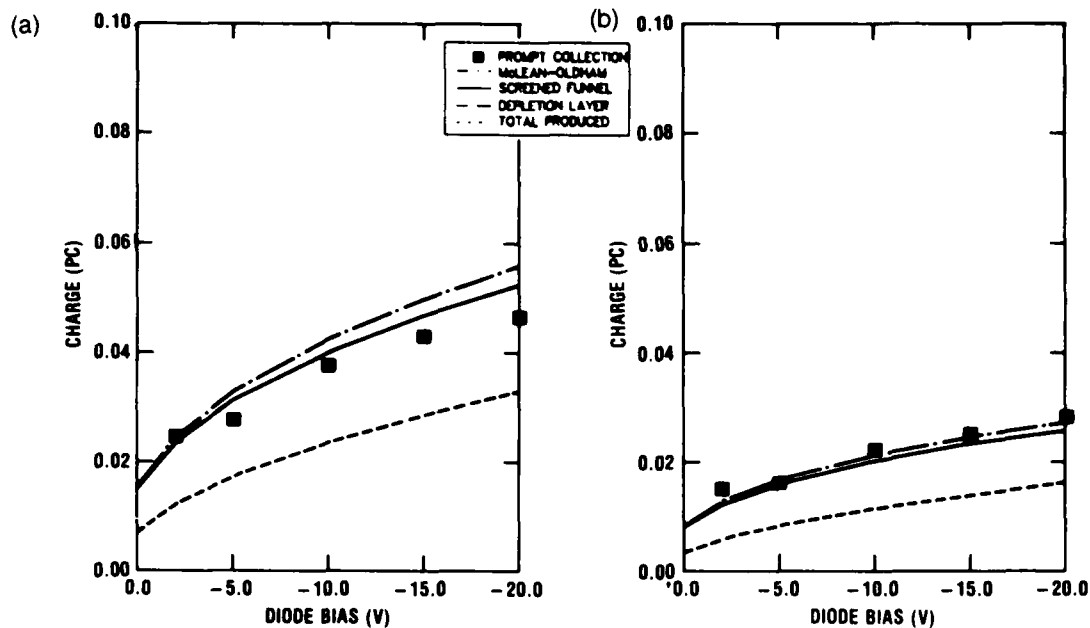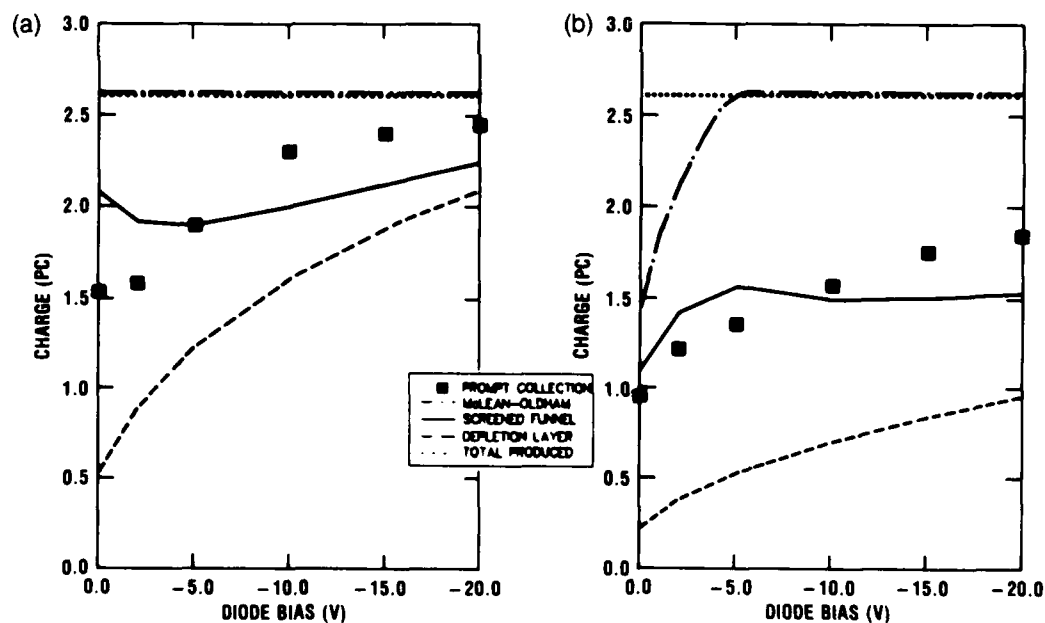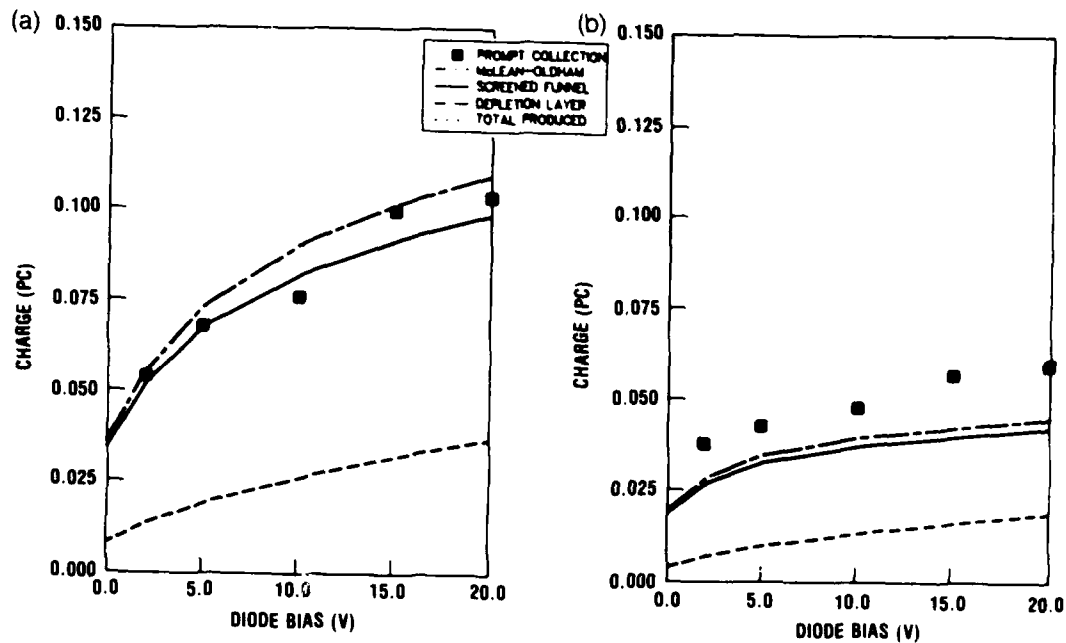
Figure 58. 5.2-MeV α-particles in p-type Si: (a) $N_A = 8.0 \times 10^{14}$ cm^{-3} and (b) $N_A = 3.0 \times 10^{15}$ cm^{-3}.

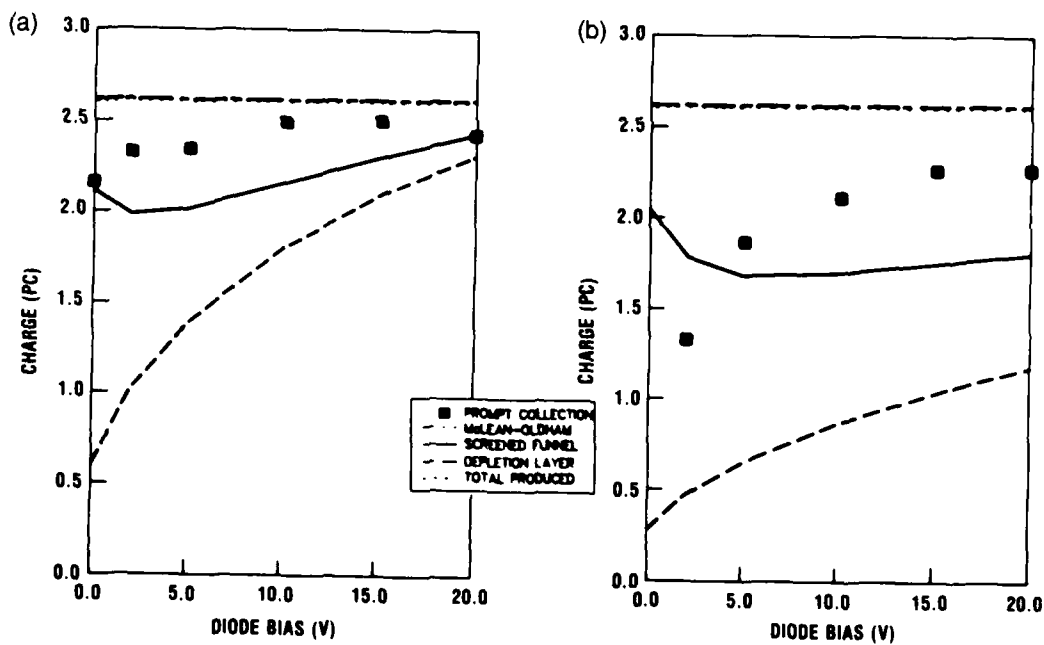Figure 59. 59.6-MeV ^{63}Cu ions in p-type Si: (a) $N_A = 3.6 \times 10^{14}$ cm^{-3} and (b) $N_A = 1.8 \times 10^{15}$ cm^{-3}.

It is also significant that the plasma screening treatment predicts stronger funneling in silicon under heavy-ion bombardment than in gallium arsenide under similar conditions. This prediction is borne out by measurements (compare, for example, fig. 55(b) with 57(b)). This result is consistent with the representation of plasma screening as an effect dependent on track conductivity through the skin depth: for a given ionization density, the gallium arsenide plasma has a much higher conductivity than the silicon plasma. This is because the electron mobility in gallium arsenide is almost 6 times higher than it is in silicon and almost 20 times higher than the hole mobility in silicon. Screening in gallium arsenide should therefore be a correspondingly stronger influence. As an illustration of this difference, tables 3 and 4 give the values of the critical screening parameters (x_D, τ, δ, L) and the resulting screening factor f_s as functions of junction bias for α-particles and copper ions incident on n-type gallium arsenide and n-type silicon. Similar tables for other diode samples and other ion-beam exposures are given in appendix D.

TABLE 3.   SCREENING PARAMETERS FOR N-TYPE GaAs

A.   5.24-MeV alpha particles in 8.0×10^{14} cm^{-3} diode ($N_o = 4.56 \times 10^8$ ion pairs/cm)

Bias (V)	x_D (μm)	τ (ns)	δ (μm)	L (μm)	f_s (unitless)
0	1.34	0.30	19.60	2.30	0.89
2	2.32	0.33	20.64	4.14	0.82
5	3.28	0.35	21.18	5.91	0.76
10	4.44	0.37	21.84	7.96	0.69
15	5.36	0.39	22.28	9.48	0.65
20	6.14	0.40	22.77	10.71	0.62

B.   56.9-MeV copper ions in 8.0×10^{14} cm^{-3} diode ($N_o = 2.19 \times 10^{10}$ ion pairs/cm)

Bias (V)	x_D (μm)	τ (ns)	δ (μm)	L (μm)	f_s (unitless)
0	1.34	1.94	7.20	5.92	0.44
2	2.32	1.11	5.45	7.69	0.24
5	3.28	0.58	3.92	7.69	0.14
10	4.44	0.35	3.07	7.69	0.08
15	5.36	0.28	2.74	7.69	0.06
20	6.14	0.25	2.57	7.69	0.05

TABLE 4. SCREENING PARAMETERS FOR N-TYPE Si

A. 5.20-MeV alpha particles in 1.0×10^{15} cm^{-3} diode ($\bar{N}_o = 3.83 \times 10^8$ ion pairs/cm)

Bias (V)	x_D (μm)	τ (ns)	δ (μm)	L (μm)	f_s (unitless)
0	1.14	0.30	50.77	2.45	0.95
2	1.97	0.28	49.18	3.88	0.92
5	2.79	0.29	50.11	5.16	0.90
10	3.77	0.30	51.45	6.58	0.88
15	4.55	0.32	52.80	7.66	0.86
20	5.21	0.33	53.26	8.53	0.85

B. 59.6-MeV copper ions in 2.8×10^{15} cm^{-3} diode ($\bar{N}_o = 1.95 \times 10^{10}$ ion pairs/cm)

Bias (V)	x_D (μm)	τ (ns)	δ (μm)	L (μm)	f_s (unitless)
0	0.68	1.08	13.54	4.82	0.70
2	1.18	0.98	12.91	7.75	0.55
5	1.66	0.89	12.32	10.16	0.44
10	2.25	0.59	9.99	10.16	0.36
15	2.72	0.48	9.07	10.16	0.33
20	3.11	0.43	8.51	10.16	0.30

6. CONCLUSIONS

The primary objective of this study was the experimental determination of the electrical response of reverse-biased n-type Schottky-barrier gallium arsenide diodes to heavy-ion bombardment. This response was measured in terms of ionization charge collection attributable to the electric-field transport (drift) of carriers, a collection process that is typically completed in less than a nanosecond. There were two measures of comparison. The first was the prompt collection provided by ionization charge generated in the diode depletion layer. Prompt collection over and above this was held to be a result of electric-field funneling. The second measure was the corresponding collection of charge via drift transport in silicon, the semiconductor material currently most used in digital device technology.

Results of experiments showed that funneling of ionization charge in these gallium arsenide diodes is a significant influence, especially for the lighter ions considered. However, the funneling contribution was shown to diminish in relative magnitude for the heavier ions, contributing in the case of copper ions little more than a few tens of percentage points of the total prompt charge collected. This trend was seen to occur to a much lesser degree in silicon diodes. The implication of this result is that silicon devices will be more vulnerable than gallium arsenide devices to single-event upset caused

by heavy ions. Neither the Hu nor McLean-Oldham analytical funnel models predict for gallium arsenide this pronounced diminution of funnel strength in the heavier ion tracks.

The observed falloff in funneling in heavy-ion tracks is held to be the consequence of plasma screening. In the more dense ionization of the heavy-ion track, longitudinal funnel fields are believed to be screened from the end of the track by the quasistatic polarization of the ionization column. A plasma screening factor has been developed here and applied to the McLean-Oldham model; the factor depends on a characteristic skin depth based on plane wave attenuation in a conducting material. Reduced predictions of prompt charge collection have been calculated with this model and compared to meas-urements in gallium arsenide. The improvement in prediction accuracy over the unscreened funnel model is substantial. Similar comparisons were made on data reported in the literature for both n- and p-type silicon diodes. Results showed similar improvement in prediction accuracy for the former and a lesser improvement for the latter, mainly at lower biases.

Two aspects of these comparisons support the screening interpretation presented here. First, the screening treatment produced only a small effect for the lightly ionized tracks of α-particles, falling close to measurements and predictions from the unscreened McLean-Oldham model. The same screening model predicted a much stronger screening effect on funneling for the more heavily ionized tracks of oxygen, chlorine, and copper ions, in both gallium arsenide and silicon. These predictions followed measured results reasonably well, while the unscreened model consistently overpredicted prompt charge collection. The second aspect that lends support to the screening interpreta-tion is that, for all other things equal in gallium arsenide and silicon, the model predicts a more pronounced screening effect in n-type gallium arsenide than in either type of silicon. This is because the electron mobility in gallium arsenide is much larger than carrier mobilities in silicon. Compari-sons of results of experiments here and in the literature bear this prediction out; i.e., the screening treatment reproduces this basic difference in the observed responses of the two semiconductor materials.

The conclusion reached in this study is that gallium arsenide offers even more promise in high-speed device technology than expected, because plasma screening associated with its high electron mobility strongly mitigates the SEU response of the material to heavy-ion bombardments.

Finally, it must be acknowledged that the screening treatment developed here is empirical, developed in response to the observed falloff in funnel strength in heavy-ion tracks in gallium arsenide. Nevertheless, it is a simple, straightforward modification to the McLean-Oldham model that appears to work reasonably well, giving the design engineer a convenient means to more acurately estimate the response of his circuits to heavy-ion strikes.

66

ACKNOWLEDGEMENTS

LITERATURE CITED

1. D. Binder, E. C. Smith, and A. B. Holman, IEEE Trans. Nucl. Sci., NS-22, No. 6 (1975), 2675.

2. T. C. May and M. H. Woods, IEEE Trans. Electron Devices, ED-26, No. 1 (1979), 2.

3. C. M. Hsieh, P. C. Murley, and R. R. O'Brien, IEEE Electron Devices Lett. EDL-2 (1981), 103.

4. C. M. Hsieh, P. C. Murley, and R. R. O'Brien, Proc. IEEE International Reliability Physics Symposium, Orlando, FL, 7 April 1981, p 38.

5. C. M. Hsieh, P. C. Murley, and R. R. O'Brien, IEEE Trans. Electron Devices, ED-30, No. 6 (1983), 686.

6. S. Kirkpatrick, IEEE Trans. Electron Devices, ED-26, No. 11 (1979), 1742.

7. C. Hu, IEEE Electron Devices Lett., EDL-3 (1982), 31.

8. G. C. Messenger, IEEE Trans. Nucl. Sci., NS-29 (1982), 2024.

9. F. B. McLean and T. R. Oldham, IEEE Trans. Nucl. Sci., NS-29 (1982), 2018.

10. T. R. Oldham and F. B. McLean, IEEE Trans. Nucl. Sci., NS-30 (1983), 4493.

11. M. A. Hopkins and J. R. Srour, IEEE Trans. Nucl. Sci., NS-30, No. 6 (1983), 4457.

12. E. L. Peterson, P. Shapiro, J. H. Adams, Jr., and E. A. Burke, IEEE Trans. Nucl. Sci., NS-29, No. 6 (1982), 2055.

13. V. A. J. van Lint, R. E. Leadon, and J. F. Colwell, IEEE Trans. Nucl. Sci., NS-19, No. 6 (1972), 181.

14. J. R. Srour and R. A. Hartman, IEEE Trans. Nucl. Sci., NS-32, No. 6 (1985).

15. K. Soliman and D. K. Nichols, IEEE Trans. Nucl. Sci., NS-32, No. 6 (1985).

16. R. Zuleeg and K. Lehovec, IEEE Trans. Nucl. Sci., NS-27, No. 5 (1980), 1343.

17. S. M. Sze, Physics of Semiconductor Devices, 2nd Ed., John Wiley & Sons, (1981), p 850.

18. R. D. Evans, The Atomic Nucleus, McGraw-Hill Book Company (1955), p 828.

LITERATURE CITED (cont'd)

19. J. F. Ziegler, <u>Handbook of Stopping Cross-Sections for Energetic Ions in All Elements</u>, Vol. 5, Pergamon Press, Inc. (1980).

20. C. A. Klein, J. Phys. Soc. Japan Suppl. <u>21</u> (1966), 307.

21. C. J. Wu and D. B. Wittry, J. Appl. Phys., <u>49</u>, No. 5 (1978), 2827.

22. K. S. Champlin, R. J. Erlandson, G. H. Glover, P. S. Hauge, and T. Lu, Appl. Phys. Lett. <u>11</u> (1967), 348.

23. L. P. Hunter, editor, <u>Handbook of Semiconductor Electronics</u>, 1st Ed., McGraw-Hill Book Company, Inc., New York (1956), p 3-3.

24. S. M. Sze, <u>Physics of Semiconductor Devices</u>, 2nd Ed., John Wiley & Sons, (1981), p 291.

25. J. E. Eberhardt, R. D. Ryan, and A. J. Tavendale, Nucl. Instrum. Methods, <u>94</u> (1971), 463.

26. K. G. McKay and K. B. McAfee, Phys. Rev., <u>91</u>, No. 5 (1958), 1079.

27. P. A. Tove and W. Seibt, Nucl. Instrum. Methods, <u>51</u> (1967), 261.

28. See, for example, J. D. Jackson, <u>Classical Electrodynamics</u>, 2nd Ed., John Wiley & Sons (1975), p 298.

29. H. L. Grubin, J. P. Kreskovsky, and B. C. Weinberg, IEEE Trans. Nucl. Sci., <u>NS-31</u>, No. 6 (1984), 1161.

APPENDIX A.--TOTAL STOPPING POWERS FOR ALL IONS IN GERMANIUM AND SILICON

APPENDIX A

FIGURES

Figures A-1 through A-8 show the Ziegler[1] total stopping powers of all ions in germanium and silicon for the ion energy range of 0.2 to 5 MeV/amu. The germanium data were used instead of data on gallium arsenide, with appropriate adjustment for the differing mass densities during conversion of these data to linear ion penetrations of the diode epitaxies. Ion energies per atomic mass unit at the diode junctions were as follows:

Target material	Ion energy/amu			
	α	O	Cl	Cu
Gallium arsenide	1.310	1.106	1.761	0.895
Silicon	1.300	1.031	1.718	0.831

Ionization profiles (fig. 26 to 34 in the body of the report) were developed using these stopping powers. For ion energies below 0.2 MeV/amu, the Ziegler stopping powers were linearly extrapolated to zero at zero ion energy.

---

[1] J. F. Ziegler, Handbook of Stopping Cross-Sections for Energetic Ions in All Elements, Vol. 5, Pergamon Press, Inc. (1980).

73

Figure A-1. Total stopping powers in Ge for H → P ions with energies from 0.2 to 0.8 MeV/amu (from Ziegler, ref 1).

Figure A-2. Total stopping powers in Ge for S → U ions with energies from 0.2 to 0.8 MeV/amu (from Ziegler, ref 1).

Figure A-3. Total stopping powers in Ge for H → P ions with energies from 0.5 to 5.0 MeV/amu (from Ziegler, ref 1).

Figure A-4. Total stopping powers in Ge for S → U ions with energies from 0.5 to 5.0 MeV/amu (from Ziegler, ref 1).

Figure A-5. Total stopping powers in Si for H → P ions with energies from 0.2 to 0.8 MeV/amu (from Ziegler, ref 1).

Figure A-6. Total stopping powers in Si for S → U ions with energies from 0.2 to 0.8 MeV/amu (from Ziegler, ref 1).
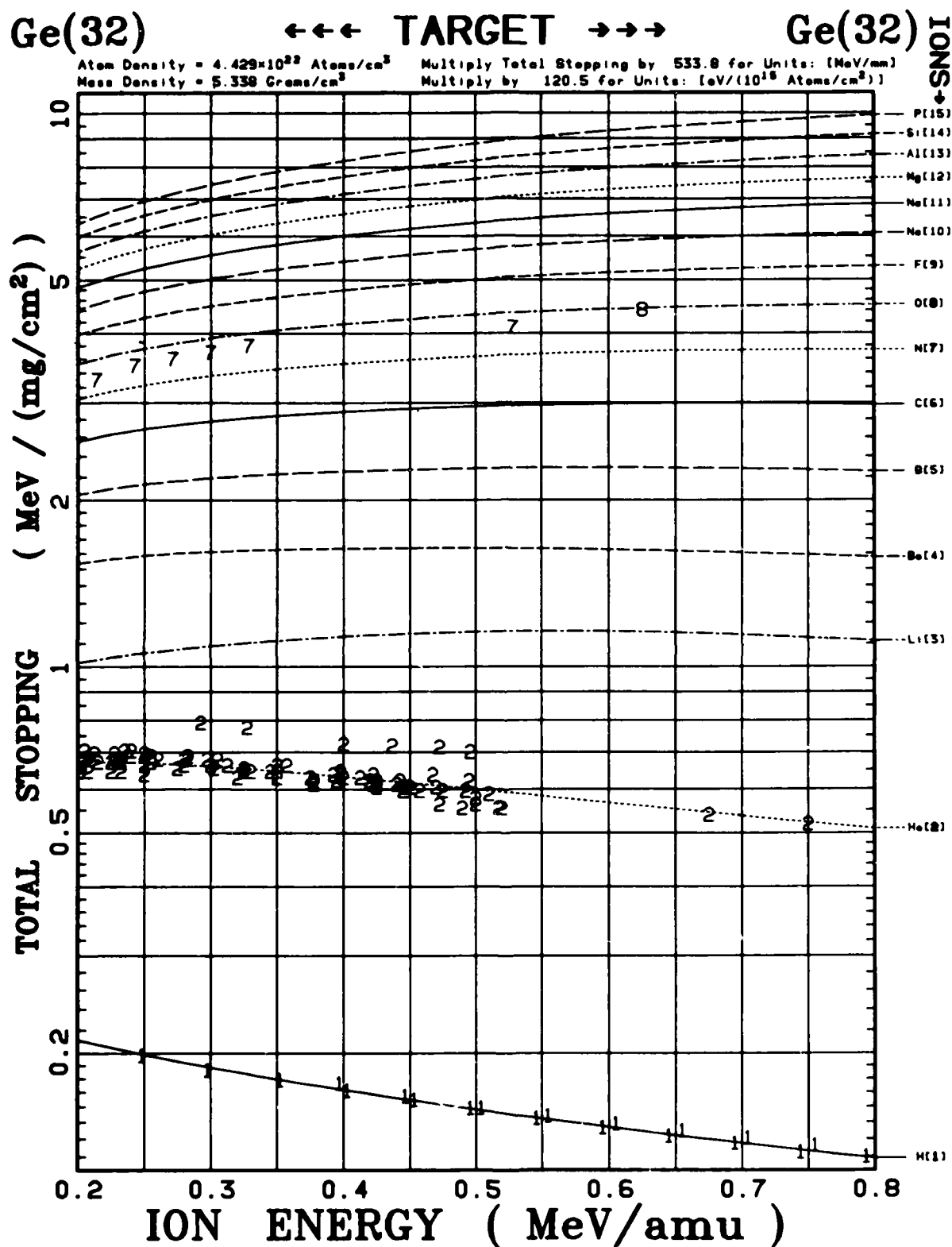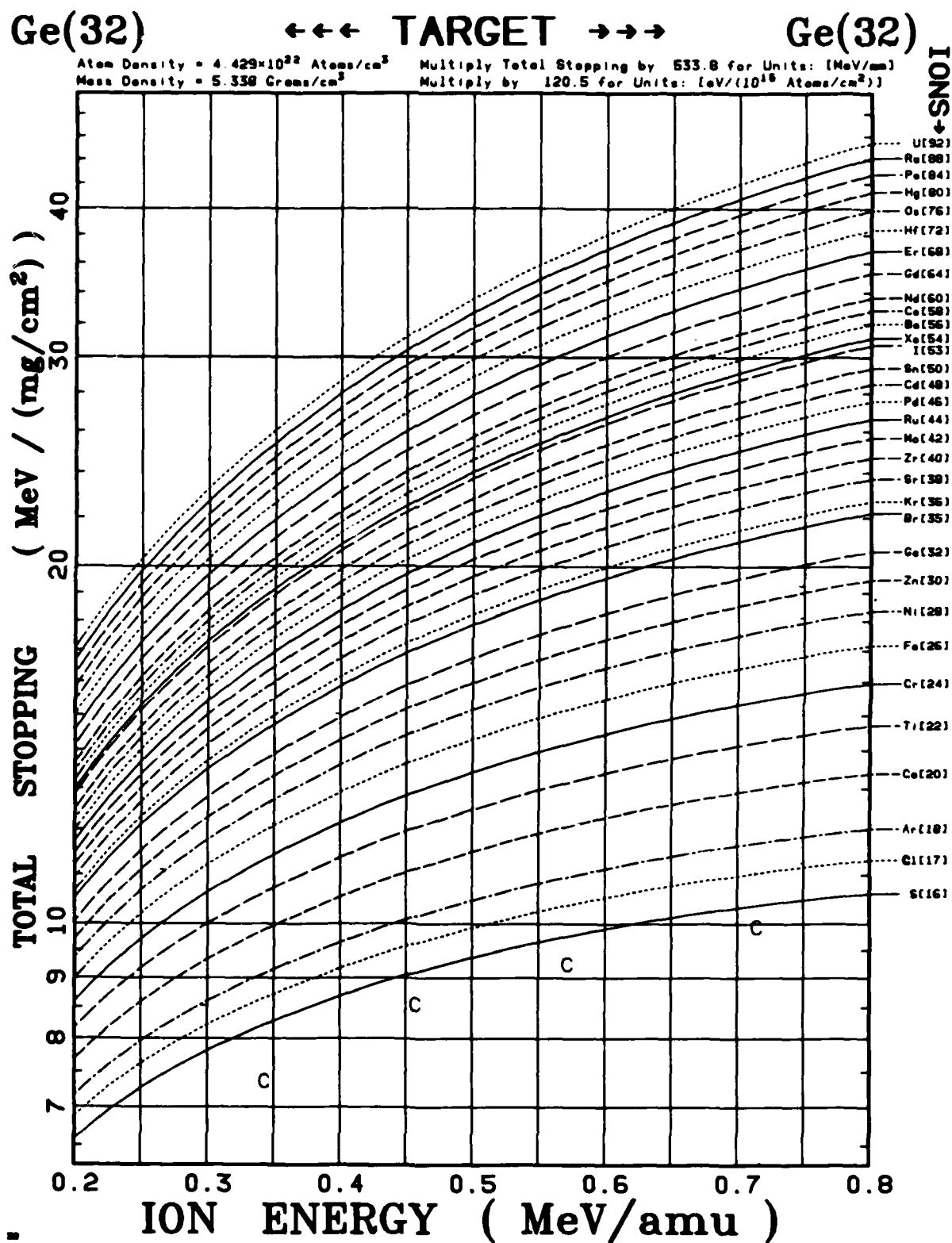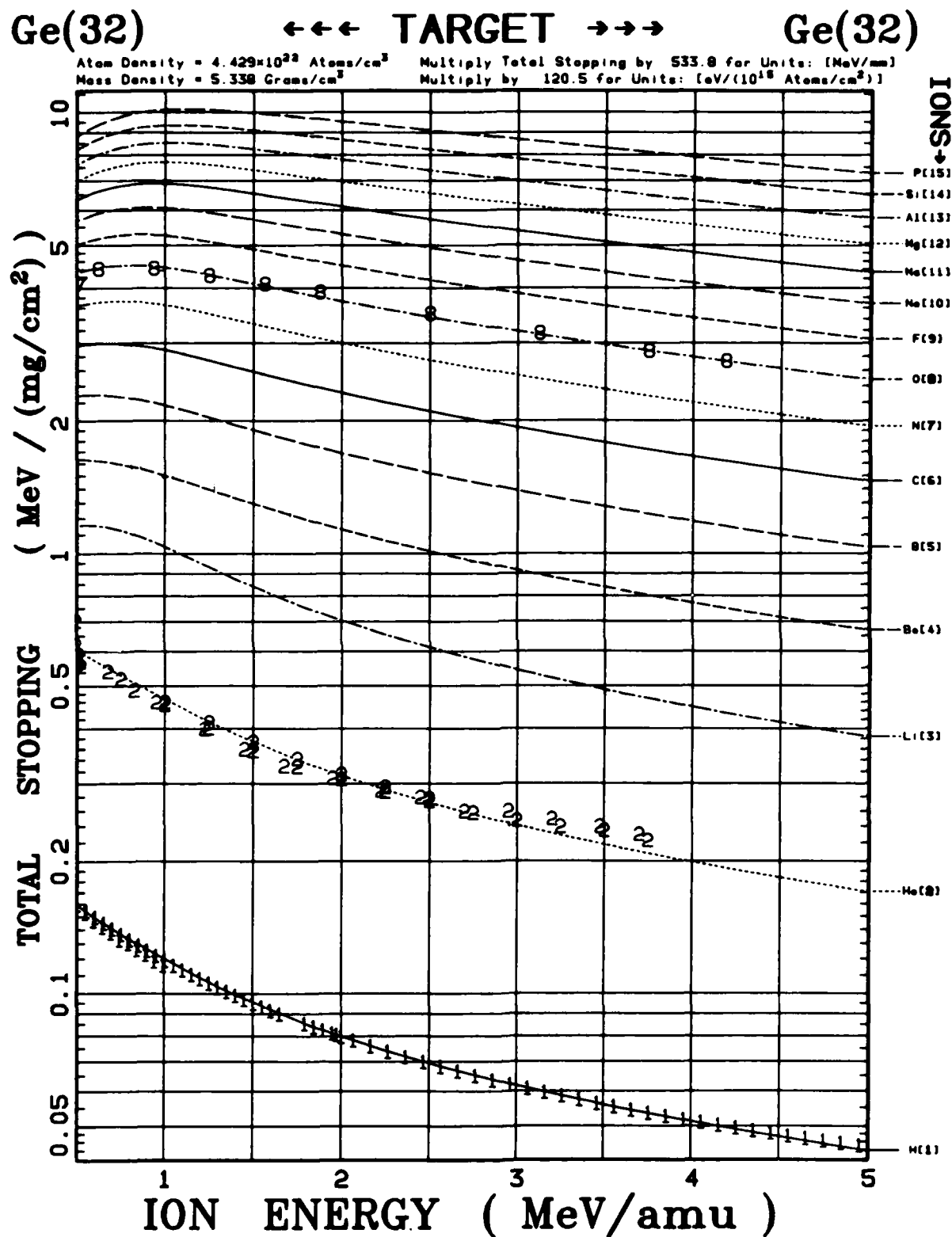
Figure A-7. Total stopping powers in Si for H → P ions with energies from 0.5 to 5.0 MeV/amu (from Ziegler, ref 1).
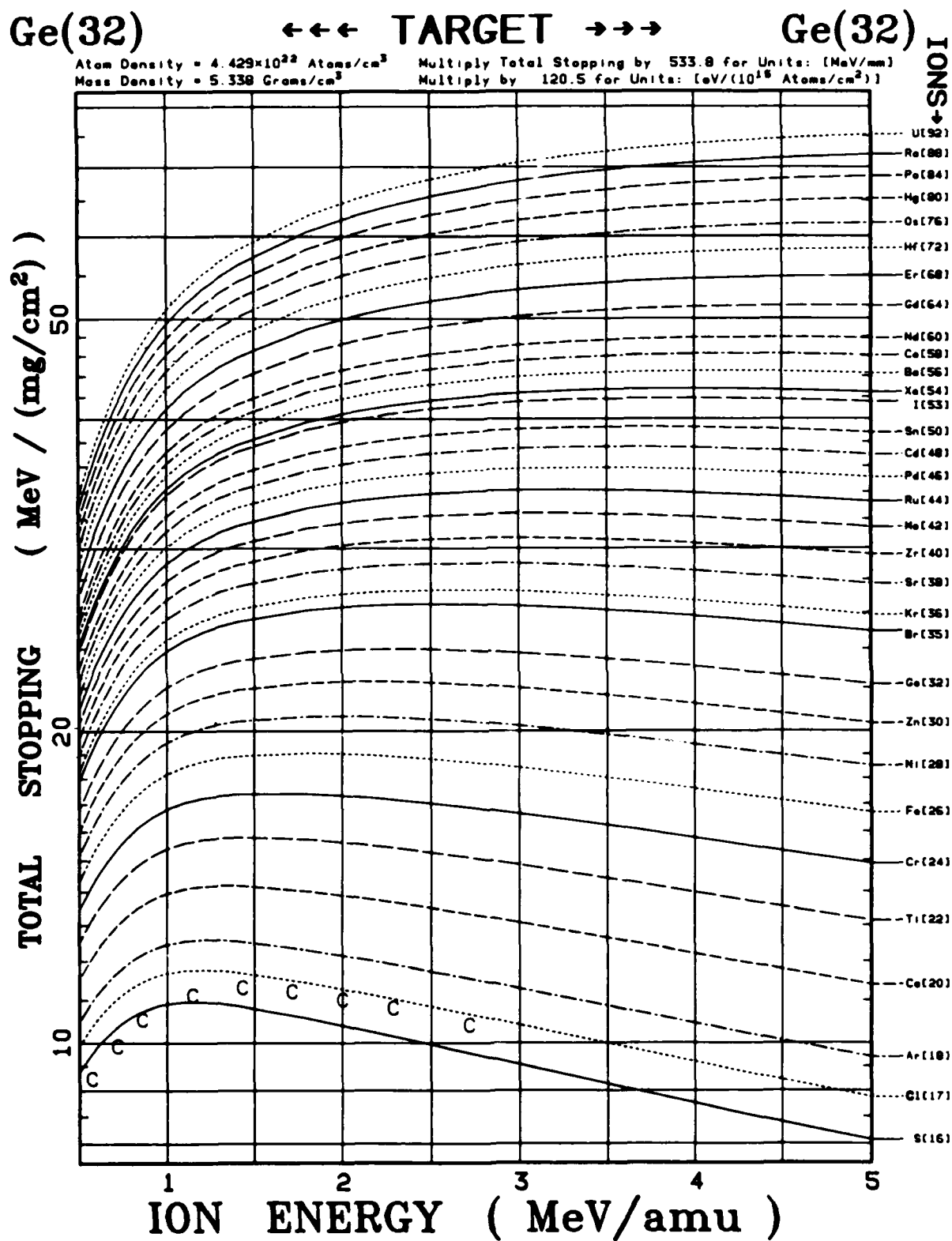
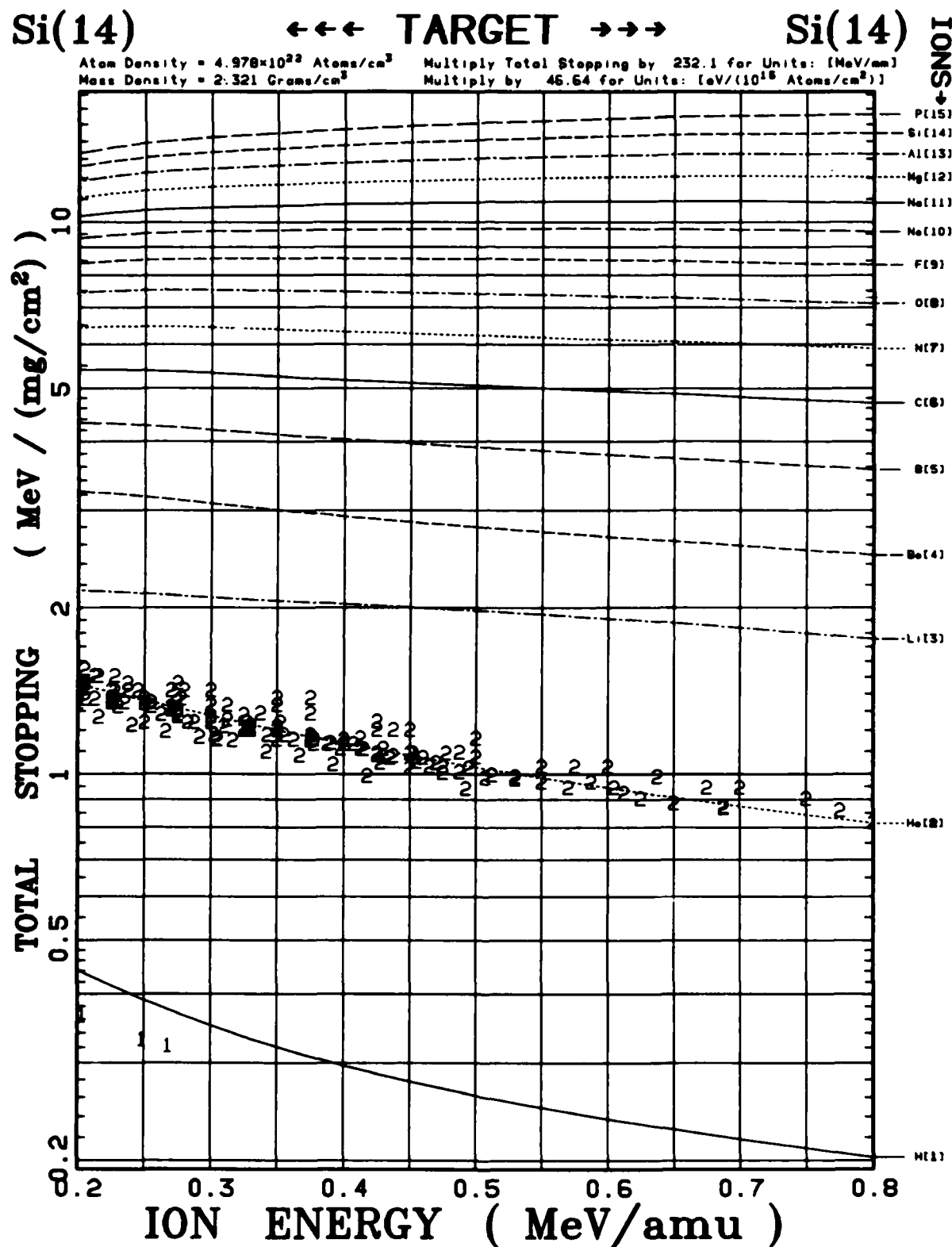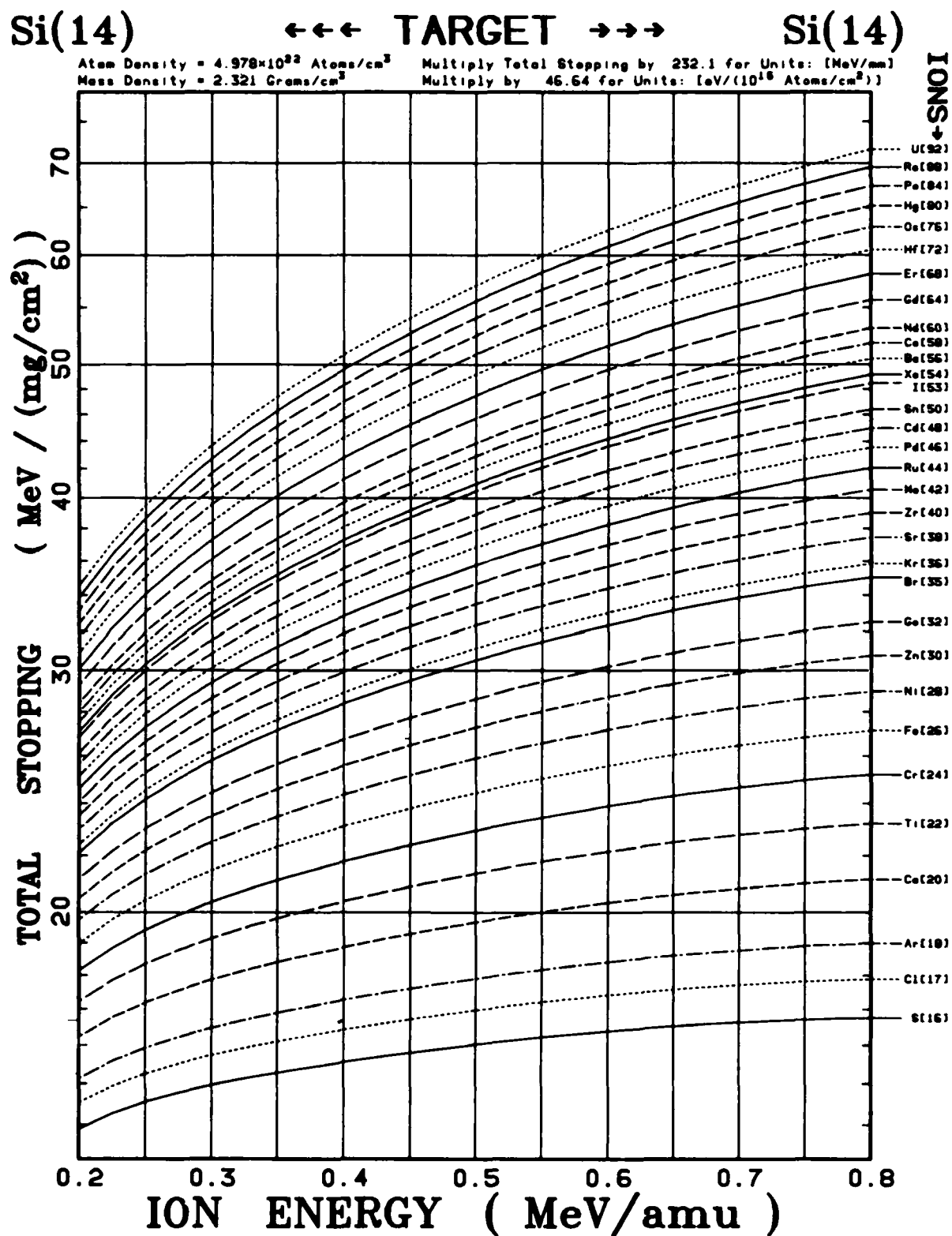Figure A-8. Total stopping powers in Si for S → U ions with energies from 0.5 to 5.0 MeV/amu (from Ziegler, ref 1).

APPENDIX B.--CAPACITANCE VALUES FOR GALLIUM ARSENIDE AND SILICON
TEST DIODES

APPENDIX B

TABLES

Table B-1 gives the capacitances of the GaAs test diodes (including the diode holder capacitance, 8.64 pF) as functions of bias voltage. Except as noted, these capacitances were measured in situ immediately before and after ion-beam exposures. Included in these tables are the percent differences in capacitances measured after exposure relative to pre-exposure values. Table B-2 gives the corresponding data for the low-doped silicon calibration diodes used for the heavy-ion experiments. In both tables B-1 and B-2, changes in capacitance were typically 0 to 3 percent and were usually larger after exposure. Table B-3 shows representative results of a cross check on the accuracy of the Boonton 72BD. This was done using an HP 4275A LCR meter. The very small differences (typically a few percentage points or less) tend to establish the accuracy of the capacitance measurements made with the Boonton 72BD meter, which was considered the most reliable source of capacitance information during this study.

TABLE B-1. IN-SITU CAPACITANCE OF GaAs DIODES AND HOLDER
(INSTRUMENT: BOONTON 72BD)

A. GaAs diode sample 2-12 ($N_D = 8.0 \times 10^{14}$ cm^{-3}), α-particles

Reverse bias voltage (V)	Capacitance (pF)		Difference (%)
	Pre-exposure	Post-exposure	
0	79.34	78.30	-1.31
-1	55.25	--	--
-2	46.54	46.90	+0.77
-5	35.64	36.10	+1.29
-10	28.94	29.70	+2.63
-15	25.64	26.60	+3.74
-20	23.74	23.80	+0.25
-25	22.44	--	--
-30	20.44	22.30	+9.10
-40	19.84	20.80	+4.84
-50	18.72	19.70	+5.23

B. GaAs diode sample 1-2 ($N_D = 1.3 \times 10^{15}$ cm^{-3}), α-particles

Reverse bias voltage (V)	Capacitance (pF)		Difference (%)
	Pre-exposure	Post-exposure	
0	119.52	118.30	-1.02
-1	76.32	--	--
-2	61.72	61.90	+0.29
-5	45.12	45.40	+0.62
-10	35.42	35.50	+0.22
-15	30.92	31.30	+1.23
-20	28.32	28.70	+1.34
-25	26.52	--	--
-30	25.22	25.60	+1.51
-40	23.32	23.70	+1.63
-50	22.02	22.40	+1.72

TABLE B-1. IN-SITU CAPACITANCE OF GaAs DIODES AND HOLDER
(cont'd)
(INSTRUMENT: BOONTON 72BD)

C. GaAs diode sample 2-3 ($N_D = 8.0 \times 10^{14}$ cm^{-3}), O ions

Reverse bias voltage (V)	Capacitance (pF)		Difference (%)
	Pre-exposure	Post-exposure	
0	66.55	65.71	-1.26
-1	48.75	--	--
-2	41.75	41.71	+0.10
-5	33.15	33.01	-0.42
-10	27.55	27.61	+0.22
-15	24.85	25.01	+0.64
-20	23.25	23.41	+0.69
-25	22.05	--	--
-30	21.15	21.21	+0.28
-40	19.75	19.18	-0.30
-50	18.85	18.71	-0.74

D. GaAs diode sample 1-7 ($N_D = 1.3 \times 10^{15}$ cm^{-3}), O ions

Reverse bias voltage (V)	Capacitance (pF)		Difference (%)
	Pre-exposure	Post-exposure	
0	121.65	121.61	0.00
-1	76.85	--	--
-2	61.15	62.81	+2.71
-5	45.05	45.81	+1.69
-10	35.15	35.91	+2.16
-15	30.65	31.41	+2.48
-20	28.05	28.81	+2.71
-25	26.25	--	--
-30	24.85	25.61	+3.06
-40	22.95	23.71	+3.31
-50	21.55	22.41	+3.99

TABLE B-1. IN-SITU CAPACITANCE OF GaAs DIODES AND HOLDER
(cont'd)
(INSTRUMENT: BOONTON 72BD)

E. GaAs diode sample 2-7 ($N_D = 8.0 \times 10^{14}$ cm^{-3}), Cl ions

Reverse bias voltage (V)	Capacitance (pF)		Difference (%)
	Pre-exposure	Post-exposure[a]	
0	87.34	83.66	4.21
-1	58.24	57.56	1.17
-2	48.24	48.26	0.04
-5	36.34	36.86	1.43
-10	29.34	30.26	3.13
-15	26.14	27.06	3.52
-20	24.14	25.16	4.22
-25	22.74	23.66	4.04
-30	21.74	22.66	4.23
-40	20.14	21.06	4.57
-50	18.97	19.96	5.22

F. GaAs diode sample 1-13 ($N_D = 1.3 \times 10^{15}$ cm^{-3}), Cl ions

Reverse bias voltage (V)	Capacitance (pF)		Difference (%)
	Pre-exposure	Post-exposure[a]	
0	123.54	121.06	-2.00
-1	78.64	79.46	+1.04
-2	63.64	64.96	+2.07
-5	46.44	47.96	+3.27
-10	36.24	38.16	+5.30
-15	31.64	33.56	+6.07
-20	28.94	30.96	+6.98
-25	24.04	29.06	+20.88
-30	25.64	27.66	+7.88
-40	23.64	25.56	+8.12
-50	22.84	24.16	+5.78

[a]Post-exposure measurements made 16 months after experiment.

TABLE B-1. IN-SITU CAPACITANCE OF GaAs DIODES AND HOLDER
(cont'd)
(INSTRUMENT: BOONTON 72BD)

G. GaAs diode sample 2-1 (N_D = 8.0 × 10^{14} cm^{-3}), Cu ions

Reverse bias voltage (V)	Capacitance (pF)		Difference (%)
	Pre-exposure	Post-exposure	
0	90.64	89.84	-0.88
-1	59.64	--	--
-2	49.44	49.04	-0.81
-5	37.04	36.94	-0.27
-10	30.04	29.64	-1.33
-15	26.74	26.34	-1.49
-20	24.74	24.44	-1.21
-25	23.34	--	--
-30	22.24	21.94	-1.35
-40	20.64	20.34	-1.45
-50	19.54	19.24	-1.53

H. GaAs diode sample 1-8 (N_D = 1.3 × 10^{15} cm^{-3}), Cu ions

Reverse bias voltage (V)	Capacitance (pF)		Difference (%)
	Pre-exposure	Post-exposure	
0	124.34	122.93	-1.13
-1	78.84	--	--
-2	63.84	63.33	-0.80
-5	46.54	46.13	-0.88
-10	36.44	36.03	-1.29
-15	31.84	31.43	-1.23
-20	29.14	28.63	-1.75
-25	27.24	--	--
-30	25.84	25.43	-1.59
-40	23.94	23.53	-1.71
-50	22.64	22.23	-1.81

TABLE B-2.   IN-SITU CAPACITANCE OF Si CALIBRATING DIODES
AND HOLDER
(INSTRUMENT: BOONTON 72BD)

A.   Si diode sample SD-4 (N_D = 9 × 10^{13} cm^{-3}), O ions

Reverse bias voltage (V)	Capacitance (pF)		Difference (%)
	Pre-exposure	Post-exposure	
0	51.04	51.02	-0.04
-1	33.44	--	--
-2	28.04	28.42	+1.35
-5	21.94	22.32	+1.73
-10	18.43	18.72	+1.57
-15	16.78	17.12	+2.03
-20	15.80	16.12	+2.02
-25	15.13	--	--
-30	14.63	14.92	+1.98
-40	13.92	14.22	+2.15
-50	13.43	13.72	+2.16

B.   Si diode sample SD-6 (N_D = 9 × 10^{13} cm^{-3}), Cl ions

Reverse bias voltage (V)	Capacitance (pF)		Difference (%)
	Pre-exposure	Post-exposure	
0	54.53	56.2	-3.06
-1	35.63	--	--
-2	29.73	30.0	+0.91
-5	23.13	23.40	+1.17
-10	19.33	19.60	+1.40
-15	17.54	17.80	+1.48
-20	16.45	16.62	+1.03
-25	15.69	--	--
-30	15.14	15.31	+1.12
-40	14.34	14.52	+1.25
-50	13.79	13.97	+1.30

C.   Si diode sample SD-3 (N_D = 9 × 10^{13} cm^{-3}), Cu ions

Reverse bias voltage (V)	Capacitance (pF)		Difference (%)
	Pre-exposure	Post-exposure	
0	52.50	51.57	-1.77
-1	34.61	--	--
-2	29.11	28.67	-1.51
-5	23.01	22.47	+2.35
-10	19.41	18.97	-2.27
-15	17.65	17.12	-3.00
-20	16.65	16.11	-3.24
-25	15.97	--	--
-30	15.50	14.98	-3.35
-40	14.90	14.40	-3.35
-50	14.53	14.02	-3.51

TABLE B-3. CROSS-CHECK ON BOONTON 72BD CAPACITANCE METER[a]

Reverse bias voltage (V)	Capacitance (pF)		Difference (%)
	Pre-exposure	Post-exposure	
0	121.65	121.40	-0.205
-1	76.85	77.32	+0.608
-2	61.15	62.60	+2.32
-5	45.05	45.66	+1.33
-10	35.15	35.90	+2.09
-20	28.05	28.79	+2.48
-25	26.25	26.99	+2.74
-30	24.85	25.66	+3.16

[a]Measurements performed on diode sample 1-7 ($N_D = 1.3 \times 10^{15} \text{ cm}^{-3}$).

APPENDIX C.--COMPARISONS OF REVERSE-BIAS LEAKAGE IN GALLIUM ARSENIDE
DIODES BEFORE AND AFTER ION BOMBARDMENT

a7/

APPENDIX C

FIGURES

Figures 11 through 12 in the main body of the report show reverse-bias current-voltage characterizations of typical low- and high-doped GaAs diodes, recorded before and after their subjection to ion bombardment. Figures C-1 through C-6 show these data for the rest of the test samples. These characterizations generally showed improved reverse-bias leakage performance following particle-beam exposures.

Cumulative heavy-ion strikes (in the accelerator particle beams) were approximately 10^3 to 10^4 particles per diode, while cumulative α-particle strikes were approximately 10^5 alpha particles per diode. The larger α-particle fluences were a consequence of uninterrupted exposure of the diode to the ^{241}Am α-particle source over the entire voltage-run sequence. This was in contrast to the heavy-ion exposures, which were interrupted between recordings at each bias voltage using the vacuum gate valve.

Diodes 1-13, 1-5, 2-11, and 2-1 showed essentially no change after their respective heavy-ion exposures, while diode 2-7 showed the largest reduction in leakage current, dropping from an initial value of about 75 nA at -50 V to about 10 nA at the same voltage. The remaining diodes showed intermediate reductions ranging from -33 percent for diode 1-8 to -17 percent for diode 2-3. No consistent pattern based on initial leakage value, doping, or ion-beam exposure is apparent in these results.

Notwithstanding these differences, the data show that the Schottky barrier junctions withstood the ion bombardments in all cases. The cause of the reductions in leakage current is not known. It is conjectured here that the effect is attributable to reduced carrier mobilities associated with increased defect (scattering-center) densities, which tend to increase the resistivity of the semiconductor material.

Figure C-1. Reverse-bias I-V curves for GaAs diode 2-11 ($N_D = 8.0 \times 10^{14}$ cm^{-3}): (a) before, (b) after α-particle exposure.

Figure C-2. Reverse-bias I-V curves for GaAs diode 1-5 ($N_D = 1.3 \times 10^{15}$ cm^{-3}): (a) before, (b) after α-particle exposure.

Figure C-3. Reverse-bias I-V curves for GaAs diode 2-3 ($N_D = 8.0 \times 10^{14}$ cm^{-3}): (a) before, (b) after O-beam exposure.

Figure C-4. Reverse-bias I-V curves for GaAs diode 1-7 ($N_D = 1.3 \times 10^{15}$ cm^{-3}): (a) before, (b) after O-beam exposure.

Figure C-5.   Reverse-bias I-V curves for GaAs diode C-7 ($N_D = 9.0 \times 10^{14}$ cm^{-3}): (a) before, (b) after Cl-beam exposure.

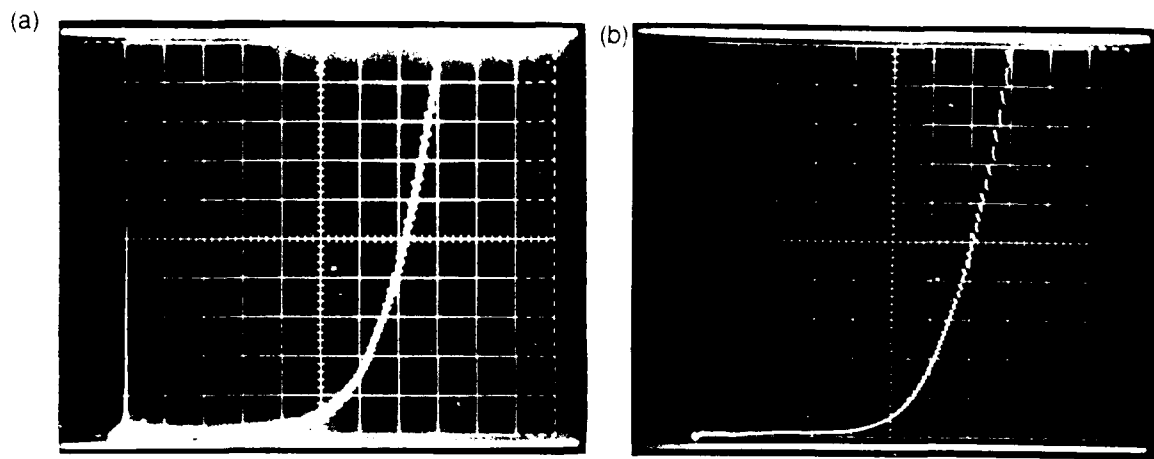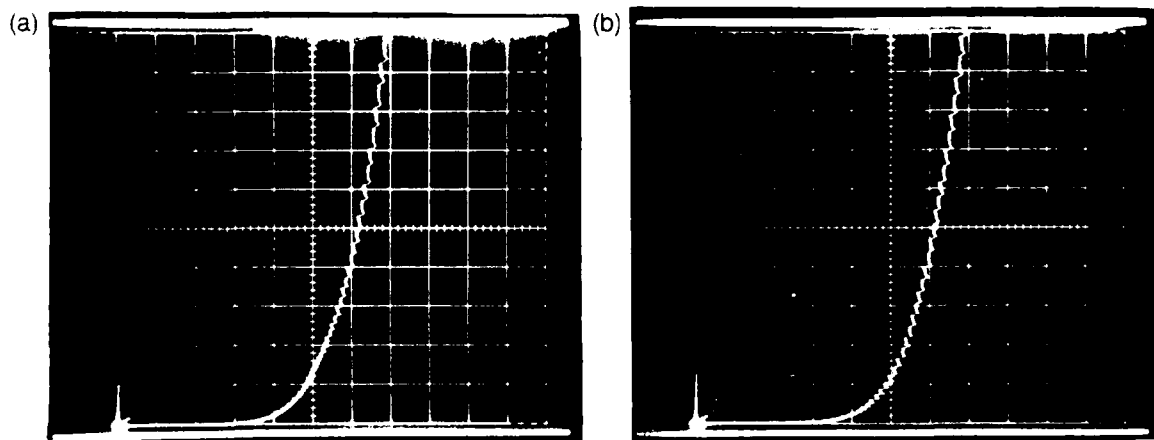Figure C-6.   Reverse-bias I-V curves for GaAs diode 1-13 ($N_D = 1.5 \times 10^{15}$ cm^{-3}): (a) before, (b) after Cl-beam exposure.

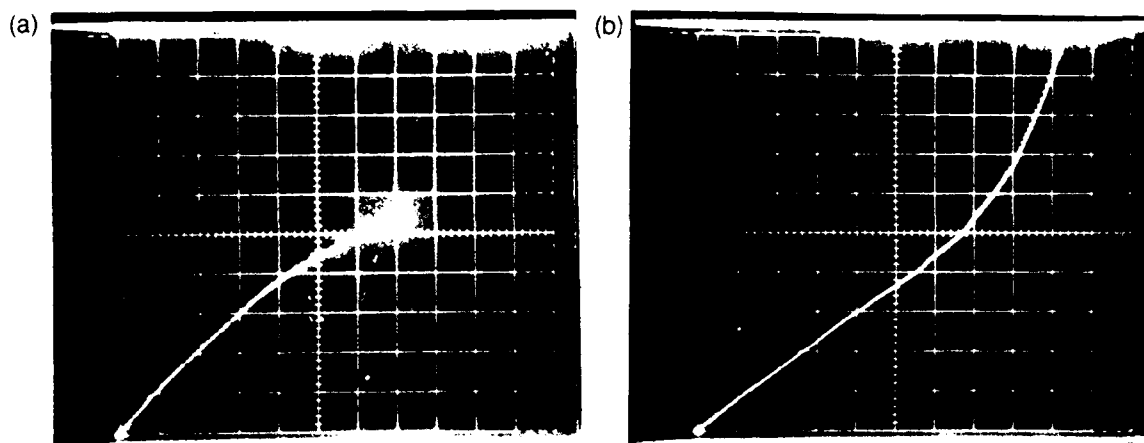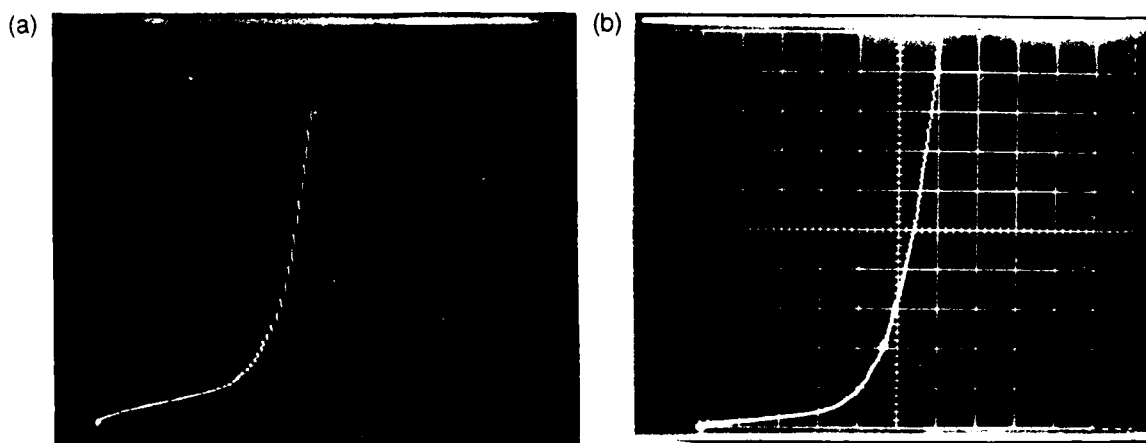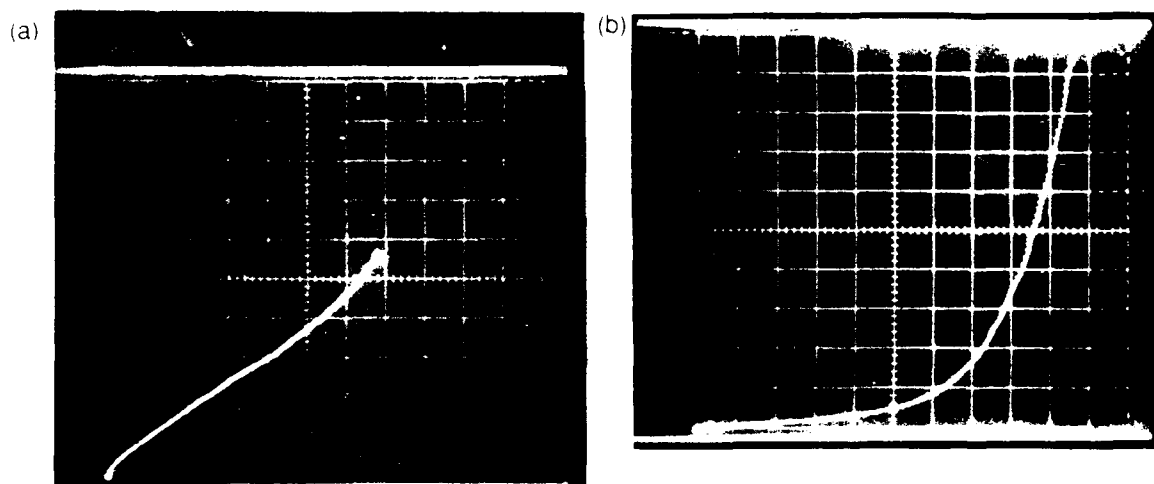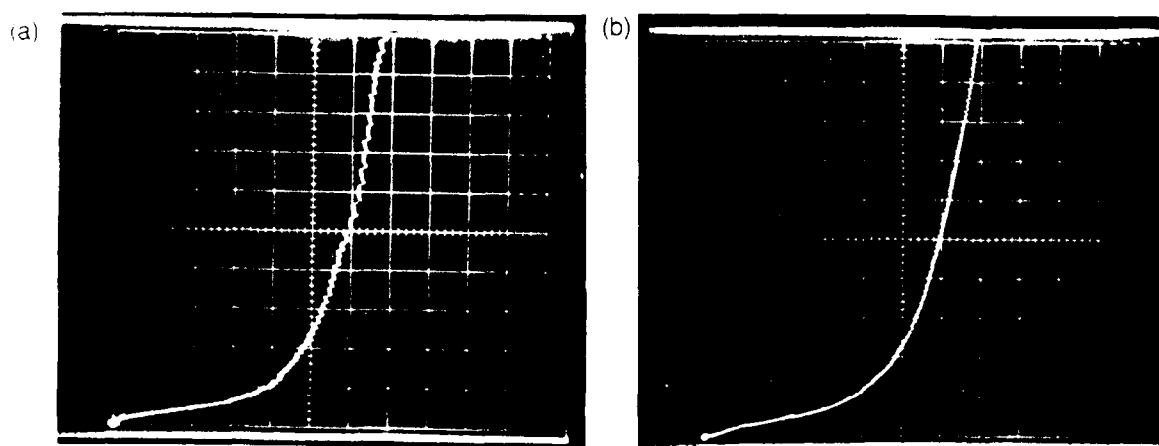APPENDIX D.--CRITICAL SCREENING PARAMETERS

1.0

4.5
2.8
2.5
3.2
2.2
3.6
4.0
2.0

1.1

1.8

1.25 1.4 1.6

CROCOPY RESOLUTION TEST CHART
NATIONAL BUREAU OF STANDARDS-1963-A

APPENDIX D

TABLES

The following tables present the critical screening parameters for silicon and gallium arsenide diodes under α-particle and copper-ion bombardments.

TABLE D-1. SCREENING PARAMETERS FOR
N-TYPE GaAs

A. 5.24-MeV α-particles in 1.3×10^{15} cm^{-3} diode ($\bar{N}_O = 4.56 \times 10^8$ ion pairs/cm)

Bias (V)	x_D (μm)	τ (ns)	δ (μm)	L (μm)	f_s (unitless)
0	1.05	0.21	16.48	1.94	0.89
2	1.82	0.24	17.52	3.48	0.82
5	2.58	0.25	17.92	4.91	0.76
10	3.49	0.27	18.52	6.54	0.70
15	4.21	0.28	18.99	7.71	0.67
20	4.82	0.29	19.28	8.64	0.64

B. 56.9-MeV copper ions in 1.3×10^{15} cm^{-3} diode ($\bar{N}_O = 2.19 \times 10^{10}$ ion pairs/cm)

Bias (V)	x_D (μm)	τ (ns)	δ (μm)	L (μm)	f_s (unitless)
0	1.05	1.50	6.33	5.18	0.44
2	1.82	1.11	5.45	7.69	0.24
5	2.58	0.58	3.92	7.69	0.14
10	3.49	0.35	3.07	7.69	0.08
15	4.21	0.28	2.74	7.69	0.06
20	4.82	0.25	2.57	7.69	0.05

TABLE D-2. SCREENING PARAMETERS FOR N-TYPE Si

A. 5.20-MeV α-particles in 4.0×10^{15} cm^{-3} diode ($\bar{N}_O = 3.83 \times 10^8$ ion pairs/cm)

Bias (V)	x_D (μm)	τ (ns)	δ (μm)	L (μm)	f_s (unitless)
0	0.57	0.10	29.14	1.33	0.955
2	0.98	0.10	29.97	2.07	0.93
5	1.39	0.11	30.88	2.71	0.92
10	1.89	0.12	31.88	3.40	0.90
15	2.27	0.12	32.69	3.91	0.89
20	2.61	0.13	33.52	4.32	0.88

B. 59.6-MeV copper ions in 4.7×10^{15} cm^{-3} diode ($\bar{N}_O = 1.95 \times 10^{10}$ ion pairs/cm)

Bias (V)	x_D (μm)	τ (ns)	δ (μm)	L (μm)	f_s (unitless)
0	1.66	4.49	27.62	10.00	0.70
2	2.87	1.64	16.66	10.16	0.54
5	4.06	0.89	12.32	10.16	0.44
10	5.50	0.59	9.99	10.16	0.36
15	6.63	0.48	9.07	10.16	0.33
20	7.60	0.43	8.51	10.16	0.30

TABLE D-3.   SCREENING PARAMETERS FOR P-TYPE Si

A.   5.20-MeV α-particles in 8.0×10^{14} cm^{-3} diode ($\bar{N}_o = 3.83 \times 10^8$ ion pairs/cm)

Bias (V)	x_D (μm)	τ (ns)	δ (μm)	L (μm)	f_s (unitless)
0	1.27	0.51	115.42	5.57	0.95
2	2.20	0.41	103.79	8.47	0.92
5	3.11	0.39	101.06	10.87	0.90
10	4.22	0.39	100.42	13.05	0.88
15	5.09	0.39	100.90	14.41	0.87
20	5.83	0.39	101.02	15.39	0.86

B.   5.20-MeV α-particles in 3.0×10^{15} cm^{-3} diode ($\bar{N}_o = 3.83 \times 10^8$ ion pairs/cm)

Bias (V)	x_D (μm)	τ (ns)	δ (μm)	L (μm)	f_s (unitless)
0	0.66	0.16	65.62	3.09	0.95
2	1.14	0.15	62.42	4.52	0.93
5	1.61	0.15	62.35	5.49	0.92
10	2.18	0.15	62.27	6.23	0.90
15	2.63	0.15	62.37	6.65	0.90
20	3.01	0.15	62.68	6.98	0.89

C.   59.6-MeV copper ions in 3.6×10^{15} cm^{-3} diode ($\bar{N}_o = 1.95 \times 10^{10}$ ion pairs/cm)

Bias (V)	x_D (μm)	τ (ns)	δ (μm)	L (μm)	f_s (unitless)
0	1.90	1.68	29.29	10.16	0.71
2	3.28	0.58	17.23	10.16	0.55
5	4.64	0.35	13.42	10.16	0.47
10	6.29	0.28	11.86	10.16	0.42
15	7.58	0.25	11.23	10.16	0.40
20	8.69	0.23	10.92	10.16	0.39

D.   59.6-MeV copper ions in 1.8×10^{15} cm^{-3} diode ($\bar{N}_o = 1.95 \times 10^{10}$ ion pairs/cm)

Bias (V)	x_D (μm)	τ (ns)	δ (μm)	L (μm)	f_s (unitless)
0	0.85	1.68	29.29	10.16	0.71
2	1.47	0.58	17.23	10.16	0.55
5	2.08	0.35	13.42	10.16	0.47
10	2.81	0.28	11.86	10.16	0.42
15	3.39	0.25	11.23	10.16	0.40
20	3.88	0.23	10.92	10.16	0.39

TABLE D-4. SCREENING PARAMETERS FOR Si
CALIBRATION DIODES ($N_D = 9.0 \times 10^{13}$ cm^{-3})

A. 5.20-MeV α-particles ($\bar{N}_o = 3.83 \times 10^{6}$
ion pairs/cm).

Bias (V)	x_D (μm)	τ (ns)	δ (μm)	L (μm)	f_s (unitless)
0	3.79	2.61	150.83	7.62	0.95
2	6.57	2.16	137.11	11.73	0.92
5	9.28	2.00	131.99	15.65	0.89
10	12.57	1.91	129.08	20.22	0.86
15	15.16	1.90	128.69	23.75	0.83
20	17.37	1.80	125.30	25.94	0.81

B. 52.8-MeV copper ions ($\bar{N}_o = 1.91 \times 10^{10}$ ion
pairs/cm)

Bias (V)	x_D (μm)	τ (ns)	δ (μm)	L (μm)	f_s (unitless)
0	3.79	3.81	25.75	9.24	0.70
2	6.57	1.37	15.46	9.24	0.55
5	9.28	0.76	11.50	9.24	0.45
10	12.57	0.51	9.43	9.24	0.38
15	15.16	0.42	8.55	9.24	0.34
20	17.37	0.37	8.01	9.24	0.32

DISTRIBUTION

ADMINISTRATOR
DEFENSE TECHNICAL INFORMATION CENTER
ATTN DTIC-DDA (12 COPIES)
CAMERON STATION, BUILDING 5
ALEXANDRIA, VA 22304-6145

DEFENSE ADVANCED RSCH PROJ AGENCY
ATTN LIBRARY
ATTN S. ROOSILD
ATTN R. REYNOLDS
1400 WILSON BLVD
ARLINGTON, VA 22209-2308

DIRECTOR
DEFENSE INTELLIGENCE AGENCY
ATTN RTS-2B
WASHINGTON, DC 20340-6537

COMMANDER
FIELD COMMAND
DEFENSE NUCLEAR AGENCY
ATTN FCTXE
KIRTLAND AFB, NM 87115-5000

HQ DA
ATTN DAMA-AR, DR. L. CAMERON
ATTN DAMA-ART, LTC B. RINEHART
WASHINGTON, DC 20310

DIRECTOR
US ARMY BALLISTIC RESEARCH LABORATORY
ATTN SLCBR-TSB-S (STINFO)
ABERDEEN PROVING GROUND, MD 21005

US ARMY ELECTRONICS TECHNOLOGY
  & DEVICES LABORATORY
ATTN SLCET-DD
FT MONMOUTH, NJ 07703

COMMANDER
US ARMY MATERIEL COMMAND
ATTN AMCCN-N, COL L. STROUD
5001 EISENHOWER AVENUE
ALEXANDRIA, 22333-0001

DIRECTOR
US ARMY MATERIEL SYSTEMS ANALYSIS
  ACTIVITY
ATTN AMXSY-MP
ABERDEEN PROVING GROUND, MD 21005

COMMANDER
US ARMY MISSILE & MUNITIONS
  CENTER & SCHOOL
ATTN ATSK-CTD-F
REDSTONE ARSENAL, AL 35809

US ARMY RESEARCH OFFICE
ATTN M. STROSCIO
PO BOX 12211
RESEARCH TRIANGLE PARK, NC 27709

US ARMY STRATEGIC DEFENSE COMMAND
ATTN R. C. WEBB
ATTN R. J. BRADSHAW, JR.
HUNTSVILLE, AL 35812

COMMANDER
US ARMY WHITE SANDS MISSILE RANGE
ATTN STEWS-TE-AN, J. MEASON
WHITE SANDS MISSILE RANGE, NM 88002

OFC OF THE DEP ASST SEC OF THE NAVY
PENTAGON 5E731
ATTN L. J. ABELLA
WASHINGTON, DC 20350

NAVAL ELECTRONICS ENGRG ACTVY
PACIFIC
PO BOX 130
ATTN CODE 250, D. O'BRYHIM
PEARL HARBOR, HI 96860-5170

COMMANDING OFFICER
NAVAL RESEARCH LABORATORY
ATTN CODE 4610, J. RITTER
ATTN CODE 4613, A. B. CAMPBELL
ATTN CODE 4673, A. KNUDSON
ATTN CODE 4611, E. PETERSON
ATTN CODE 4611, J. B. LANGWORTHY
ATTN CODE 4611, W. BENDEL
ATTN CODE 5816, H. HUGHES
WASHINGTON, DC 20375-0001

COMMANDING OFFICER
NAVAL WEAPONS SUPPORT CENTER
ATTN CODE 6054, T. ELLIS
ATTN CODE 6054, J. RAMSEY
ATTN CODE 6054, D. PLATTETER
CRANE, IN 47522

HQ, USAF/SAMI
WASHINGTON, DC 20330

AIR FORCE INSTITUTE OF TECHNOLOGY
ATTN LIBRARY/AFIT/LDEE
WRIGHT-PATTERSON AFB, OH 45433-6583

AIR FORCE WEAPONS LABORATORY, AFSC
ATTN NTCAS, J. FERRY
ATTN NTCAS, J. MULLIS
KIRTLAND AFB, N, 87117-6008

COMMANDER
ROME AIR DEVELOPMENT CENTER, AFSC
ATTN ESR B. BUCHANAN
HANSCOM AFB, MA 01731

DEPARTMENT OF COMMERCE
NATIONAL BUREAU OF STANDARDS
ATTN CODE A305, K. GALLOWAY
ATTN CODE A237, H. SCHAFFT
BLDG 101, ROOM A-705
WASHINGTON, DC 20234

SPACE DIVISION/AQ
PO BOX 92960
ATTN ALT
WORLDWAY POSTAL CENTER
LOS ANGELES, CA 90009-2960

LOS ALAMOS NATIONAL LABORATORY
PO BOX 1663
ATTN D. B. HOLTKAMP
LOS ALAMOS, NM 87545

NASA
GODDARD SPACE FLIGHT CENTER
ATTN CODE 313, V. DANCHENKO
ATTN CODE 601, E. STASSINOPOULOS
ATTN CODE 660, J. TRAINOR
ATTN CODE 695, M. ACUNA
GREENBELT, MD 20771

NASA HEADQUARTERS
ATTN CODE DP, B. BERNSTEIN
WASHINGTON, DC 20546

SANDIA NATIONAL LABORATORIES
PO BOX 5800
ATTN ORG 2110, R. E. BLAIR
ATTN ORG 2144, P. V. DRESSENDORFER
ATTN ORG 5160, F. N. COPPAGE
ALBUQUERQUE, NM 87185-5800

ADVANCED RESEARCH & APPLICATIONS
  CORP
ATTN L. PALKUTI
1223 E. ARQUES AVE
SUNNYVALE, CA 94086-4701

AEROSPACE CORP
PO BOX 92957
ATTN W. CRANE, A2/1083
ATTN W. KOLASINSKI, BLDG M2, MS/259
ATTN V. JOSEPHSON
ATTN P. BUCHMAN
ATTN G. GILLEY
ATTN J. B. BLAKE
LOS ANGELES, CA 90009-2957

BDM CORP
ATTN C. M. STICKLEY
7915 JONES BRANCH DRIVE
MCLEAN, VA 22102-3396

BOEING CO
PO BOX 3707
MAIL STOP 33-04
ATTN M/S 2R-00, A JOHNSTON
ATTN M/S 18-73, C. ROSENBERG
ATTN M/S 2R-00, I. ARIMURA
SEATTLE, WA 98124-2207

CALIFORNIA INSTITUTE OF TECHNOLOGY
JET PROPULSION LAB
ATTN W. PRICE, MS-83-122
4800 OAK GROVE DRIVE
PASADENA, CA 91103

CHARLES STARK DRAPER LAB INC
ATTN N. TIBBETTS
555 TECHNOLOGY SQUARE
CAMBRIDGE, MA 02139-3539

CLARKSON COLLEGE OF TECHNOLOGY
ATTN P. J. MCNULTY
POTSDAM, NY 13676-1499

ELECTRONIC INDUSTRIES ASSO
ATTN J. KINN
2001 EYE STREET, NW
WASHINGTON, DC 20006-5009

ENGINEERING SOCIETIES LIBRARY
ATTN ACQUISITIONS DEPARTMENT
345 EAST 47TH STREET
NEW YORK, NY 10017

GENERAL ELECTRIC CO
SPACE SYSTEMS DIVISION
VALLEY FORGE SPACE CENTER
PO BOX 8555
ATTN D. HOESCHELE
PHILADELPHIA, PA 19101-8555

HONEYWELL, INC
MILITARY AVIONICS DIVISION
ATTN R. BELT, MS-MN 17-22334
ATTN G. HAVEY, MN 17-2334
ATTN D. NEILSEN, SSED MS-MN 14-3015
2600 RIDGEWAY PARKWAY
MINNEAPOLIS, MN 55413-1719

JOHNS HOPKINS UNIVERSITY
APPLIED PHYSICS LAB
ATTN R. MAURER
JOHNS HOPKINS RD
LAUREL, MD 20707-6099

JOHNS HOPKINS UNIVERSITY
ATTN DEPT OF ELEC ENGR, G. MASSON
34TH & CHARLES STREET
BALTIMORE, MD 21218

IBM CORP
THOMAS J. WATSON RSCH CTR
PO BOX 218
ATTN J. ZIEGLER
YORKTOWN HEIGHTS, NY 10598-0218

ILLINOIS COMPUTER RESEARCH, INC
ATTN E. S. DAVIDSON
2114 LYNWOOD DRIVE
CHAMPAIGN, IL 61821-6608

ILLINOIS COMPUTER RESEARCH, INC
ATTN J. ABRAHAM
603 W. GREEN
CHAMPAIGN, IL 61820-5012

IRT CORP
PO BOX 85317
ATTN J. HARRITY
SAN DIEGO, CA 92138-9048

KAMAN SCIENCES CORP
SYSTEMS DIRECTORATE
ATTN E. CONRAD
1911 JEFFERSON DAVIS HIGHWAY
ARLINGTON, VA 22202-3508

KAMAN TEMPO
ALEXANDRIA OFFICE
HUNTINGTON BUILDING
ATTN DASIAC
2560 HUNTINGTON AVE
ALEXANDRIA, VA 22303-1410

LITTON SYSTEMS, INC
GUIDANCE & CONTROL SYSTEMS DIVISION
ATTN E. L. ZIMMERMAN
ATTN L. SMITH, MS 76-31
5500 CANOGA AVE
WOODLAND HILLS, CA 91367-6698

LOCKHEED MISSILES & SPACE CO, INC
ATTN F. JUNGA, 97-40 BLDG 202
3251 HANOVER STREET
PALO ALTO, CA 94304-1191

MCDONNELL DOUGLAS CORP
PO BOX 516
ATTN R. L. KLOSTER, DEPT E 451
ST LOUIS, MO 63166-0516

MR. GEORGE C. MESSENGER
CONSULTING ENGINEER
3111 BEL AIR DRIVE, 7-F
LAS VEGAS, NV 89109-1558

MISSION RESEARCH CORP
SAN DIEGO
ATTN J. RAYMOND
5434 RUFFIN RD
SAN DIEGO, CA 92123-1313

MOTOROLA, INC
SEMICONDUCTOR PRODUCTS SECTOR
PO BOX 2953
ATTN C. LUND
PHOENIX, AZ 85062-2953

NORTH CAROLINA UNIVERSITY
DEPARTMENT OF ELECTRICAL ENGRG
PO BOX 5275
ATTN S. DIEHL
RALEIGH, NC 27650-5275

NORTHROP CORP
ELECTRONIC DIVISION
PO BOX 5032
ATTN E. KING, C3323/WC
HAWTHORNE, CA 90251-5032

107

NORTHROP CORP
NORTHROP RESEARCH & TECHNOLOGY CTR
ATTN J. SROUR
ATTN A. BAHRAMAN
ONE RESEARCH PARK
PALOS VERDES PENINSULA, CA 90274-5471

R&D ASSOCIATES
PO BOX 9695
ATTN C. KNOWLES
MARINA DEL REY, CA 90295

RAND CORP
ATTN B. BENNETT
2100 M STREET, NW
WASHINGTON, DC 20037-1270

RAND CORP
PO BOX 2138
ATTN P. DAVIS
SANTA MONICA, CA 90406-2138

RCA CORP
AEROSPACE & DEFENSE
ASTRO-ELECTRONIC DIV
PO BOX 800
ATTN G. BRUCKER
PRINCETON, NJ 08540

RESEARCH TRIANGLE INSTITUTE
PO BOX 12194
ATTN M. SIMONS
RESEARCH TRIANGLE PARK, NC 27709-2194

ROCKWELL INTERNATIONAL CORP
ROCKETDYNE DIVISION
ATTN R. OLSON, MS AC34
6633 CANOGA AVENUE
CANOGA PARK, CA 91303-2703

SCIENCE APPLICATIONS INTL CORP
ATTN J. SPRATT
2615 PACIFIC COAST HWY
SUITE 300
HERMOSA BEACH, CA 90254-2293

SCIENCE APPLICATIONS INTL CORP
PO BOX 2351
ATTN D. LONG
ATTN D. MILLWARD
ATTN R. FITZWILSON
LA JOLLA, CA 92038-2351

SCIENTIFIC RESEARCH ASSO, INC
PO BOX 498
ATTN H. GRUBIN
GLASTONBURY, CT 06033-0498

TEXAS INSTRUMENTS, INC
PO BOX 225474
ATTN J. SALZMAN
ATTN T. CHEEK, MS 3143
ATTN F. POBLENZ, MS 3143
ATTN M. L. BUSCHBOM, MS 961
DALLAS, TX 75265-5474

TRW ELECTRONICS & DEFENSE SECTOR
BALLISTIC MISSILE DIV
PO BOX 1310
ATTN M. ASA, MS R1/2144
SAN BERNARDINO, CA 92402-1310

TRW ELECTRONICS & DEFENSE SECTOR
ATTN A. WITTELES, MS R1/2144
ATTN M. S. ASH
ATTN O. ADAMS
ATTN W. WILLIS
ATTN P. R. REID, MS R6/2541
ONE SPACE PARK
REDONDO BEACH, CA 90278

WESTINGHOUSE ELECTRIC CO
ADVANCED TECHNOLOGY LAB
PO BOX 1521
ATTN F. BLAHA, MS 3206
ATTN E. J. BOLING, MS 3431
BALITMORE, MD 21203-1521

WESTINGHOUSE ELECTRIC CORP
DEFENSE & ELECTRONIC CTR
PO BOX 1693
ATTN H. KALAPACA, MS 5155
ATTN D. GRIMES, MS 5155
BALTIMORE, MD 21203-1693

US ARMY LABORATORY COMMAND
ATTN COMMANDER, AMSLC-CG
ATTN TECHNICAL DIRECTOR, AMSLC-TD

INSTALLATION SUPPORT ACTIVITY
ATTN DIRECTOR, SLCIS-D
ATTN RECORD COPY, SCLIS-IM-TS
ATTN LIBRARY, SLCIS-IM-TL (3 COPIES)
ATTN LIBRARY, SLCIS-IM-TL (WOODBRIDGE)
ATTN TECHNICAL REPORTS BRANCH, SLCIS-IM-TR
ATTN LEGAL OFFICE, SLCIS-CC

DIRECTOR
HARRY DIAMOND LABORATORIES
ATTN D/DIVISION DIRECTORS
ATTN CHIEF, SLCHD-NW-E
ATTN CHIEF, SLCHD-NW-EB
ATTN CHIEF, SLCID-NW-EC
ATTN CHIEF, SLCHD-NW-ED
ATTN CHIEF, SLCHD-NW-EE
ATTN CHIEF, SLCHD-NW-R
ATTN CHIEF, SLCHD-NW-RA
ATTN CHIEF, SLCHD-NW-RC
ATTN CHIEF, SLCHD-NW-RE
ATTN CHIEF, SLCHD-NW-RH
ATTN CHIEF, SLCHD-NW-RI
ATTN CHIEF, SLCHD-NW-P
ATTN SLCHD-IT-EB, B. ZABLUDOWSKI
ATTN SLCHD-NW-P, J. CORRIGAN
ATTN SLCHD-NW-RC, K. W. BENNETT
ATTN SLCHD-NW-RC, H. E. BOESCH, JR.
ATTN SLCHD-NW-RC, J. MCGARRITY
ATTN SLCHD-NW-RC, F. B. MCLEAN
ATTN SLCHD-NW-RC, T. OLDHAM
ATTN SLCHD-NW-RH, H. EISEN
ATTN SLCHD-NW-RH, R. GILBERT (10 COPIES)
ATTN SLCHD-NW-RH, G. OVREBO (10 COPIES)
ATTN SLCHD-NW-RH, J. SCHIFANO (10 COPIES)

END

12-86

DTIC